REACTION-BASED KNOCK PREDICTIVE MODELING AND MODEL-BASED STOCHASTIC KNOCK LIMIT CONTROL OF SPARK-IGNITION ENGINES

By

Ruixue Li

A DISSERTATION

Submitted to
Michigan State University
in partial fulfillment of the requirements
for the degree of

Mechanical Engineering – Doctor of Philosophy

2020

ABSTRACT

REACTION-BASED KNOCK PREDICTIVE MODELING AND MODEL-BASED STOCHASTIC KNOCK LIMIT CONTROL OF SPARK-IGNITION ENGINES

By

Ruixue Li

This dissertation studies the spark-ignition (SI) engine knock phenomenon, abnormal combustion due to the auto-ignition of end-gas ahead of the propagated flame front, resulting in the rapid chemical energy release with aggressive combustion, limiting the further improvement of thermal efficiency and even damaging the engine mechanically. A control-oriented combustion and pressure wave model with satisfactory accuracy and low computational effort is a necessity for the knock control strategy design. This dissertation develops a control-oriented knock predictive model that includes a two-zone reaction-based combustion model and a pressure wave model. This knock predictive model is capable of accurately describing the combustion process of a spark-ignited engine and predict the in-cylinder pressure oscillations under knocking combustion in real-time. Based on this model, a feedforward and feedback stochastic knock limit control strategy is developed to reduce the knock cyclic variability and control the knock mean-intensity below a desired up bound while keeping spark timing as close to engine maximum brake torque (MBT) timing as possible.

A control-oriented two-zone reaction-based model to accurately describe the combustion process of a SI engine is first developed. Instead of using the conventional pre-determined Wiebe-based combustion model, a two-step chemical reaction model is utilized to predict the combustion process along with important thermodynamic parameters such as the mass-fraction-burned, in-cylinder pressure, temperatures and individual species mass changes in both zones. Sensitivities of model parameters are analyzed during the model calibration process. As a result, one set of calibration parameters are used to predict combustion characteristics over all engine operating conditions studied in this paper, which is the major advantage of the proposed method. Also, the proposed modeling approach is capable of modeling the combustion process for real-time simulations. As the by-product of the model, engine knock can also be predicted based on the Arrhenius integral

in the unburned zone, which is valuable for model-based knock control. The proposed combustion model is intensively validated using the experimental data with a peak relative prediction error of 6.2% for the in-cylinder pressure.

Based on this validated combustion model, a control-oriented pressure wave model for SI engines is further developed. This model is capable of predicting the in-cylinder pressure oscillations under knocking combustion in real-time and can be used for the model-based knock prediction and control. A pressure wave equation including the knock deadening behavior is proposed, simplified, and used to calculate the pressure perturbations generated by the knocking combustion. The boundary and initial conditions at knock onset are analyzed and the analytic solution of the pressure wave equation is obtained. The model is calibrated and validated over two different engine operating conditions at knock limit. The chemical kinetic-based Arrhenius integral (ARI) and the KI20 are used as the evaluation methods for knock onset and intensity prediction, and the knock frequency is studied with a fast Fourier transform of the filtered in-cylinder pressure oscillations. Especially, the knock characteristics associated with gas mixture properties at intake valve closing is analyzed based on the experimental data and their effect to knock cycle-to-cycle variation is also studied for the proposed model.

In addition, this dissertation studies the correlation between in-cylinder mixture temperature at intake valve closing and the engine knock, along with knock cyclic variability based on the knock predictive model. A strong correlation between the intake temperature and knock intensity has been obtained and validated based on the simulation investigation and experiment data obtained at knock limit. Therefore, a model-based feedforward and feedback stochastic knock limit control strategy is developed to reduce the knock cycle-to-cycle variability and maintain the knock mean-intensity within a desired up bound by controlling the spark timing as close to MBT timing as possible. The control performance is validated with the simulation results to show the capability of the model-based feedforward and feedback stochastic knock limit control in significantly reducing the knock cyclic variability and improving the knock intensity distribution for the best fuel economy.

ACKNOWLEDGMENTS

This dissertation would not have been possible without the help of so many people. I would like to express my immeasurable appreciation and deepest gratitude to all the people whose assistance were a milestone in the completion of my Ph.D. study.

Foremost, I wish to express my deepest gratitude to my advisor, Prof. Guoming (George) Zhu, for his persistent support, professional guidance and profound encouragement of my Ph.D. study and research. It is my fortune to join his group, study and do my research work with his patience, enthusiasm and immense knowledge. His comprehensive knowledge in advanced control theory and practical experience in automotive industry inspired my passion for control theories and applications in automotive. Besides, I would not have been possible to work in Isuzu North America and Pilot Systems International LLC. as a control engineer intern for 12 months without his recommendation and guidance. It is whole-heartedly appreciated that his great advice for my study proved monumental towards the success of my Ph.D. study. What I learned from him is invaluable for my future career and life!

I wish to express my sincere appreciation to my committee members: Dr. Harold Schock, Dr. Hassan Khalil, and Dr. Ranjan Mukherjee, for their encouragement and insightful comments of my courses, research and dissertation. Dr. Harold Schock gave me the greatest guidance in the internal combustion engine and simulation using GT-SUITE. Dr. Hassan Khalil and Dr. Ranjan Mukherjee provided me solid knowledge of linear/nonlinear control and adaptive control, which is the foundation of my research work and industry internship experience.

I wish to express my warmest regards to the lab engineers and my fellow labmates, with whom I am honored to have worked during my Ph.D study in Energy and Automotive Research Lab. My special gratitude goes to Dr. Tianyi He for his kindness and help in the control system design of my Ph.D project and my internship project in Pilot Systems International LLC. I also wish to thank Dr. Yifan Men and Dr. Ruitao Song for their invaluable assistance in the reaction-based combustion modeling, calibration and bench testing. I'd like to express my appreciation to our

electrical engineer, Kevin Moran, and mechanical engineer, Tom Stuecken, and Dr. Sedigheh Tolou, for their help for the bench setup and testing. Many thanks to Dr. Yingxu Wang, Dr. Huan Li, Dr. Chengsheng Miao, Anuj Pal, Wenpeng Wei, Jian Tang, Dawei Hu and Shen Qu, for their kindly help and wonderful time we spent together.

I wish to send my special appreciation to the engineers and interns whom I worked with in Pilot Systems International LLC. and Isuzu North America, Powertrain and Vehicle Research Development. I wish to thank Dr. Jim Winkelman and Stuart Steel for their professional knowledge, practical industry experience and consistent support in the project of road noise cancellation control system design of suspension system. I also wish to thank my supervisor and mentor in Isuzu North America: Tim Victor and Thirumal Harikrishnan for their guidance and support in the project of oxygen fraction estimation of diesel engine air-path system.

Lastly, to my loving and supportive parents, brother, and sweetest cat Sally. This journey would not have been possible without their love, understanding and encouragement.

TABLE OF CONTENTS

LIST OF TABLES

LIST OF FIGURES

CHAPTER 1

INTRODUCTION

1.1 Motivation

Nowadays, energy crisis and environmental issues are two of the biggest challenges worldwide that motivate the automotive industry to improve the engine efficiency and reduce emissions, that are two main goals for optimizing internal combustion (IC) engine performances. Over 90% of passenger cars around the world are powered by the IC engines, where spark-ignited (SI) engines consist of about 85% of them. Especially, the fuel consumption of SI engines are 20~30% higher than the diesel engines [2]. Therefore, the main research of SI engines is to further improve the fuel economy and reduce emissions [3] that are closely related to combustion process. However, operating engine at its knock limit turns out to be one of the main challenges in improving the thermal efficiency of SI engines. Especially, SI engines with high compression ratio, turbocharger, and even reduced displacement combustion chamber become the tendency in recent years to improve the engine fuel efficiency. The increased boost level or high compression ratio raises the probability of engine knock event [2, 4].

Knock is an abnormal combustion phenomenon in the spark-ignited (SI) engine resulted by the auto-ignition of end-gas (unburned) in the propagating flame front [5, 6]. The chemical reaction energy aggressively released by the auto-ignited end-gas and the main combustion by the spark ignition will cause the uneven heat distributions in the combustion chamber, leading to high frequency shock waves, sharp pressure rise, and high temperature that may damage the engine. Knock at high engine speed can cause rapid engine damage and less damaging but is more likely to cause driver annoyance at low engine speed [7]. Especially, under certain operational conditions, the MBT timing is more advanced than the knock boundary spark timing, it is not able to operate the ignition at MBT timing without engine knock. In these conditions, it is desirable to operate the engine at the knock limit to produce the best fuel efficiency. Therefore, the engine knock prediction

and spark timing control to operate the engine at knock limit or MBT timing take an significant role in improving SI engine fuel economy.

Spark timing control is extensively studied in the literature (see [8, 9]) to operate the engine close to its MBT timing without knock combustion. A traditional method for knock limit control is to advance or retard the spark timing by integral control based on the error between the measured knock intensity and the pre-defined knock intensity threshold [9], resulting in operating the engine in and out of knock combustion unsmoothly. The fluctuations of engine spark timing over engine cycles cannot guarantee satisfactory knock limit control performance of operating the engine at its MBT timing as close as possible. The analysis of experimental knock data indicates that engine knock is a stochastic phenomenon and knock control should not only limit the engine knock intensity below its desired level but also reduce the knock cycle-to-cycle variability.

Therefore, the motivation of this dissertation is to develop model-based stochastic knock limit control algorithms to operate the SI engine at border-line knock limit under these conditions that the MBT timing is limited by knock, and to control the knock intensity within the desired bound with minimum cycle-to-cycle knock variability. The foundation for the control design is a knock predictive model that is able to accurately predict the combustion process, knock major characteristics (knock onset timing, frequency, intensity, cyclic variability) in real-time. However, there is limited study in literature about the reaction-based real-time model for spark-ignition (SI) engines capable of knock prediction. Note that auto-ignition of end-gas (knock) in SI engines is a very important phenomenon, and unfortunately, there is not many results on control-oriented knock modeling. So the development of knock control oriented combustion and knock prediction model, and model-based stochastic knock limit control are two main goals of this dissertation.

1.2 Research Overview

1.2.1 Control-Oriented Combustion Model for SI Engines

In the past decades, the model-based engine control, especially combustion control, is widely studied due to the rapid technology development in combustion sensing and real-time computing power. As

part of model-based engine control, major progress has been made in developing control-oriented engine and combustion models for both spark-ignition (SI) and compression ignition (CI) internal combustion engines [10]. These developed models are used for model-based design and calibration to efficiently reduce engine development time and cost [11]. The control-oriented engine models are used for model-based control in real-time applications. Furthermore, since engine dynamics, emissions, and performance can be efficiently studied through simulations without conducting physical experiments, it is possible to study engine operations at its operational boundary when experiments are hard to conduct without damaging the physical system.

Model-based combustion control leads to the development of control-oriented engine combustion models to reliably predict the in-cylinder combustion process by providing detailed mass-fraction-burned (MFB) rate, in-cylinder pressure, and other information [11]. Up to now, there are several widely-used modeling approaches for the in-cylinder combustion process that can be classified as single-zone, multi-zone, and multi-dimensional models [12]. The multi-dimensional computational fluid dynamics (CFD) models accurately describe the in-cylinder combustion process, including the flame fluid dynamics and the in-cylinder mixture characteristics, by solving a number of partial differential equations. Some multi-dimensional CFD models predict the combustion process by modeling thousands of chemical reaction species with certain reaction steps. One of the most popular approaches is the CHEMKIN-CFD module for ANSYS FLUENT that uses the multi-dimensional model to simulate detailed chemical mechanisms and chemically reacting flows in a multidimensional cylinder and to trace individual species information.

Although these models are able to predict the combustion process accurately, they require tremendous computational power to even simulate the combustion process for one engine cycle. As a result, the multi-dimensional CFD models are only good for off-line simulations, but it is not suitable for model-based control design and validation that require real-time simulation capability. The GT-Power and Ricardo Wave engine models, widely used in automotive industry, use 0-D/1-D modeling approach to take account of the gas flow dynamics outside of combustion chamber and 0-D single-zone modeling approach for the combustion process based on the empirical combustion

functions such as the Wiebe function [13, 14, 15, 16]. GT-power models are significantly simplified over the CFD ones [17] but it still cannot be used for real-time simulations. On the other hand, the 0-D single zone combustion model, such as the mean-value model [18], was widely used for control design due to its ability of conducting real-time simulations. To reduce simulation time, it uses maps to model the complex combustion process. As a result, the model accuracy is highly dependent on the calibration process and its transient responses are not accurate since the thermodynamics is not modeled. Furthermore, the mean-value model is not able to predict the in-cylinder pressure, heat-release-rate (HRR), and states of chemical species.

To overcome the limitations of these combustion models discussed above, two-zone and multi-zone models are developed. Shapiro and Gerpen [19] presented a two-zone combustion model for internal combustion engines based on the second-law of thermodynamics. Loganathan [20] and Saad [21] proposed a two-zone combustion model for diesel engines, and Borg [22] developed a two-zone model for SI engines to study engine performance. Note that in two-zone models, the gas mixture are separated into burned (reaction) and unburned zones, assuming that the flame front is a thin boundary layer separating the two zones, as shown in Figure 1.1 for a two-zone combustion model of SI engines. In some literature [3, 23, 24], the unburned zone is further split into multiple zones based on temperature gradients, assuming that the mixture in each individual zone is homogeneous but has different thermodynamic characteristics. Rakopoulos and Michos [3, 23] proposed a multi-zone combustion model for engine transient performance and NOx (Nitric-oxide) formation of a syngas SI engine. However, the MFB rate of these discussed two- and multi-zone models [18, 19, 20, 21, 22, 23, 24, 25, 26, 27] is generated by an empirical Wiebe function that needs to be calibrated as a function of engine speed, load, exhaust-gas-recirculation (EGR), etc. for each engine operating condition.

To improve Wiebe-based combustion model, the flame development dynamics is introduced in the real-time combustion model recently. Hall, et al. [28] proposed a control-oriented two-zone combustion model for SI engines, assuming that the burned zone is sphere-shaped with the flame front on the boundary and MFB rate is determined by calculating the flame speed. However, since

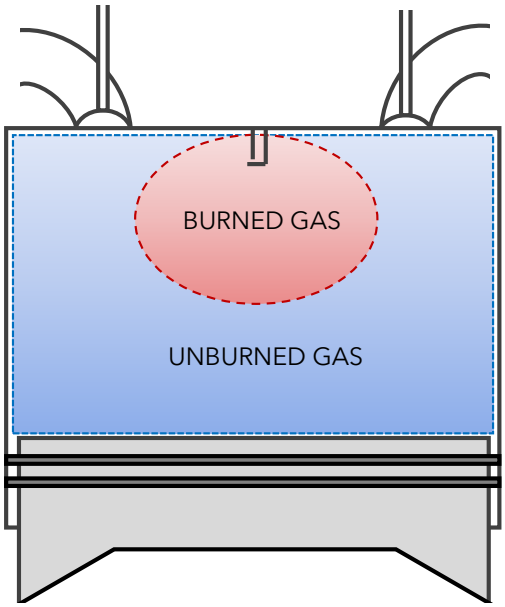

Figure 1.1: A two-zone combustion model for SI engines

the chemical reaction process is not modeled, thermodynamic properties of the chemical species cannot be predicted. In order to predict the combustion process along with key thermodynamic parameters such as the MFB rate, in-cylinder pressure, temperatures and individual species mass changes, the reaction-based combustion model is developed. Jia and Wang [29] presented a control-oriented reaction-based single-zone combustion model for a propane-fueled Homogeneous Charge Compression Ignition (HCCI) engine, and Men and Zhu[30] also proposed a control-oriented three-zone reaction-based combustion model for direct-injection (DI) diesel engines. Both discarded the empirical Wiebe-based combustion model, and instead, adopted single or multi-step chemical kinetic mechanism in conjunction with the Arrhenius function-based reaction rates. The reaction-based combustion model takes into account for chemical characteristics in the actual combustion process and is able to predict the MFB rate, pressure rise rate, HRR, and zone temperatures as well as the properties of each individual chemical species with very low computational load. Therefore, the reaction-based combustion model can be further developed for the real-time knock prediction

and model-based knock control.

1.2.2 Knock Prediction and Modeling for SI Engines

The auto-ignition of the end-gas in the unburned mixtures will result in the shock waves in the combustion chamber, led to the pressure oscillations, rapid pressure and temperature raise. As shown in Figure 1.2 for the experimental in-cylinder pressure (blue solid-line) and the band-pass filtered pressure oscillations (red-solid line) for one cycle when the engine is operated at knock condition. After the knock onset, the in-cylinder pressure rapidly raises up to 35bar due to the aggressive knocking combustion. And the maximum pressure oscillation amplitude is 3bar. The temperature of the unburned mixture is below 1000K before knock onset, and then it can be up to 3000K. Therefore, the prediction and control of engine knock is very important to prevent the engine damage, and meet the fuel economy and emission regulations.

Engine knock phenomenon is extensively studied in past decades from the knock detection methods to 3-D modeling of the knocking combustion. Knock detection is the first step to study knock characteristics and many methods are proposed for knock detection [31, 32, 33, 34].The pressure sensor is one of the most popular methods used to detect engine knock in the lab, accelerometer (also called knock sensor) is widely used in production vehicles for detecting engine knock but the mechanical vibration caused by engine valve events and interaction among different combustion chambers adds significant noise into the knock sensor, sometimes making knock detection impossible. Some new methods are proposed in the past decade. Zhu, Haskara, and Winkelman [35] developed an ignition coil based ionization detection circuit for detecting the engine knock. The knock onset prediction is another important topic for improving engine knock control [36, 37, 38]. Two prediction methods are widely used in past decades. One is auto-ignition delay model [39] based on calculated auto-ignition delay time τ defined as duration between the end of compression and knock onset time. The pressure and temperature of the unburned mixtures are required but no chemical reaction and flame dynamics are considered. The other method is the chemical kinetic method based on the Arrhenius integral utilizing the chemical reaction

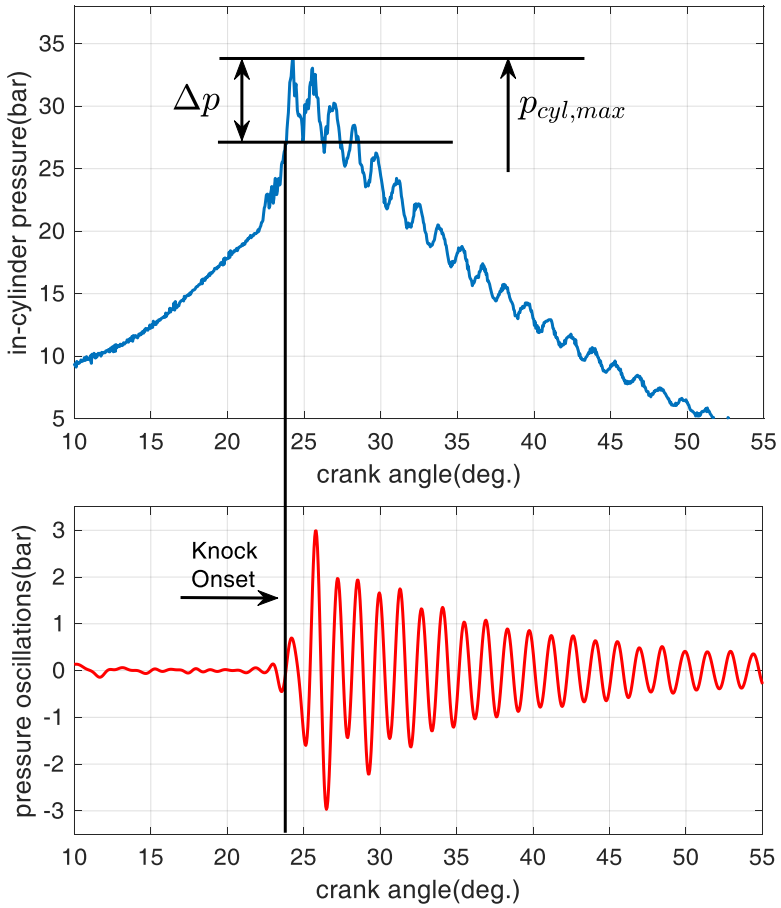

Figure 1.2: Experimental in-cylinder pressure and filtered pressure oscillations under knock condition

rate and concentration of the species involved in the auto-ignition. Both methods have their advantages and disadvantages. The auto-ignition delay method has been improved [40, 38, 41] and is widely used due to the its simplicity and low computing cost. However, without considering the important chemical reaction process in the combustion chamber, the auto-ignition process cannot be predicted accurately. The Arrhenius integral method is widely used in 3-D computational fluid dynamic (CFD) models for predicting the knock onset but the chemical reaction steps and species involved can be fairly large (up to thousands), resulting in the high computation load. It is not suitable for the model-based knock control design. So a real-time model that is able to predict the

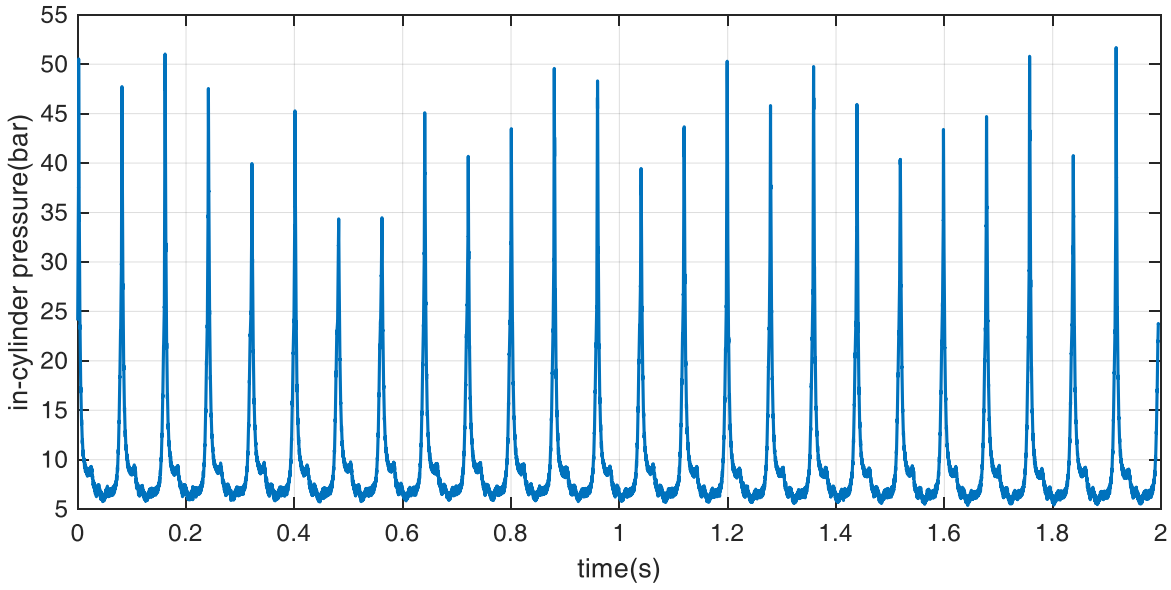

Figure 1.3: Time-based experimental in-cylinder pressure when the engine is operated at the knock limit (steady-state)

engine combustion process and also knock phenomenon is highly desired.

Engine knock phenomenon is complex and not consistent. In-cylinder pressure oscillation information has great potential in identifying major knock characteristics [42] such as knock frequency and intensity and it is widely studied. As shown in Figure 1.2, the pressure oscillations are generated after the knock onset, and the filtered pressure oscillation wave (red solid-line) can be further analyzed to obtain the frequency, intensity and knock onset timing. Moreover, the engine knock has a distinguishing characteristics: the cycle-to-cycle variability [43, 44, 45]. As shown in Figure 1.3 for a time-based in-cylinder pressure of 25 continuous cycles. It is obvious that the peak pressure is not consistent at knock condition when the engine is operated at steady-state. To better demonstrate the knock intensity variability, the cycle-based experimental in-cylinder pressure of 11 continuous cycles are shown in Figure 1.4. It indicates that the knock intensity is not consistent but shows strong variability, and the peak pressure location (PPL) moves to be closed to MBT as long as the knock intensity increases. The details of cycle #11, that has the heaviest knock intensity, are shown in Figure 1.5. Therefore, the study of pressure oscillations as well as the knock

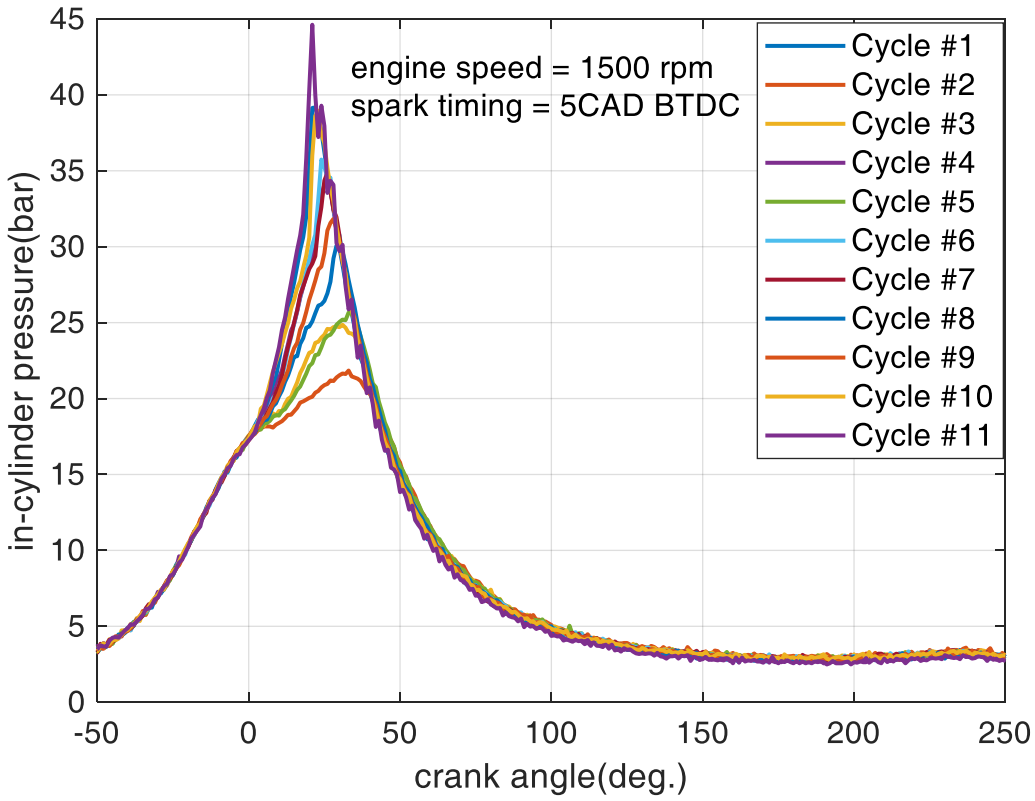

Figure 1.4: Cycle-based experimental in-cylinder pressure when the engine is operated at knock limit (steady-state)

cycle-to-cycle variability are very important for the knock prediction modeling.

Katsumata, Morikawa and Tanabe [46] investigated the end-gas shock waves under knocking combustion using a high-speed direct and schlieren photography method. Kawahara and Tomita [47] visualized the auto-ignition of end-gas and pressure waves in a hydrogen spark-ignition engine using a high-speed camera, and furthermore, they even observed the cycle-to-cycle images of the auto-ignited kernel in the end-gas region. The visualization results indicate that large amount of unburned mixtures generates strong shock waves caused by the auto-ignited kernel explosion. These optical diagnostics methods are very helpful to understand the physical process of knocking combustion. Modeling in-cylinder pressure waves under knocking combustion and associated numerical simulations are widely used to study the knock phenomenon. Yao and Xu [48] developed

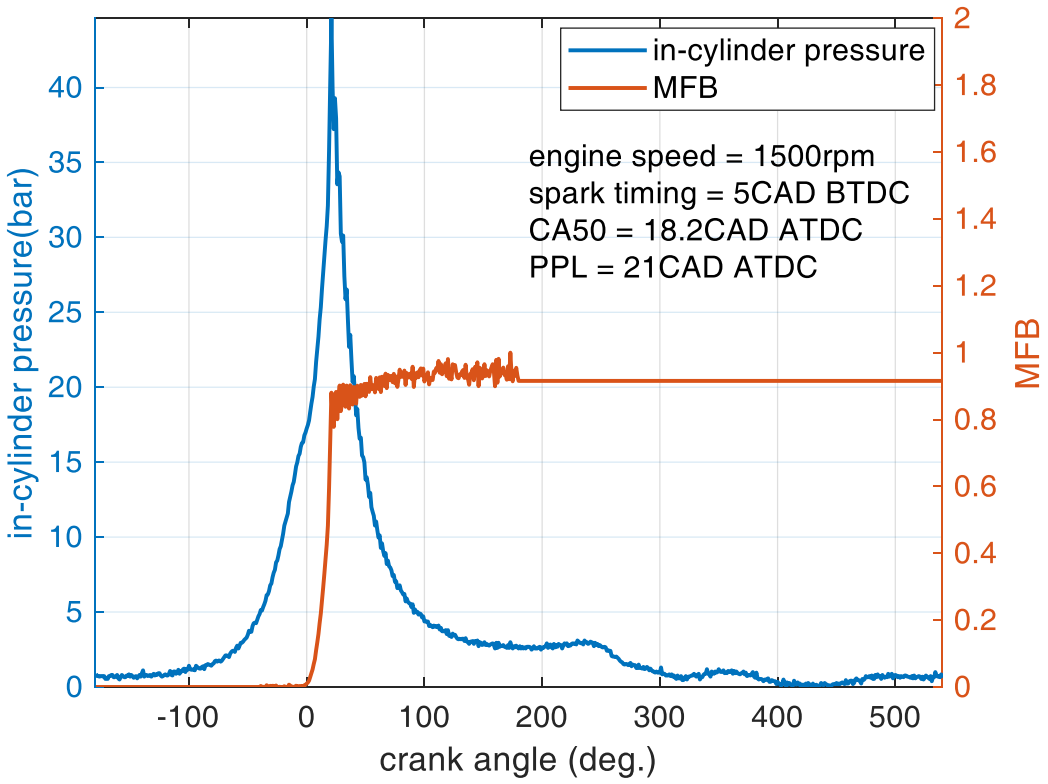

Figure 1.5: Experimental in-cylinder pressure and MFB rate for a heavy knock cycle

a 3-D CFD model to study the propagation and reflection of pressure waves generated by the end-gas auto-ignition. They used the 3-D simulation results to optimize the combustion chamber shape. Terashima and Koshi [49] proposed a 1-D pressure wave model including large detailed chemical kinetic mechanisms to study the pressure wave generated during end-gas auto-ignition and the results demonstrate the influence of wall temperature to the knock intensity. Richard [50] developed a 1-D CFD model to predict the cycle-to-cycle variability in SI engines based on the analysis of Large-Eddy Simulation (LES). These 1-D and 3-D models are able to predict the in-cylinder pressure oscillation accurately but with tremendous computational load. Therefore, they are good for off-line studying knock characteristics but not suitable for model-based knock prediction and control design.

To overcome the limitations of the 1-D and 3-D models discussed above and reduce the computation load, simplified 0-D pressure wave model is required. However, there are few literature in the area of real-time pressure oscillation modeling. Draper [51] is a pioneer of applying the acoustic wave equation to internal combustion engines to study the pressure wave characteristics in the combustion chamber but the pressure oscillation magnitude decay behavior, caused by the energy loss and piston movement, was not considered. Note that the deadening behavior is a natural process and must be considered for accurately predicting the real-time pressure oscillations. Based on Draper's work, Brecq and Corre [52] proposed a pressure envelop curve to predict the pressure oscillation peaks. Although this envelop curve shows the magnitude decay behavior, it is a curve fitting model that is not able to predict the actual pressure oscillations. Based on the envelop curve model, an improved 3-D pressure wave model is proposed by Di Gaeta [53] to describe the actual pressure oscillations and magnitude decay behavior. A general solution to this wave equation is provided but the 3-D model is still too complex to be used for model-based knock prediction and control design. Therefore, a physical-based real-time pressure wave model that is capable to predict the pressure oscillations resulted by knocking combustion is important for knock control design.

1.2.3 Model-Based Knock Limit Control for SI Engines

The knock intensity is commonly used to present the engine knock severity. In general, the knock intensity is calculated by processing the knock sensor signal with a band-pass filter and then integrating within a pre-defined knock window. As discussed in the last section, the engine knock phenomenon has a significant characteristics: the knock intensity of each cycle is randomly varying cycle-to-cycle with minimal cyclic correlation even under steady-state operational condition, as shown in Figure 1.3. Due to this cyclic knock variability, the knock control objective generally focuses on the stochastic knock intensity control with statistical analysis approach. In literature [35, 9, 49, 7, 54, 55, 56, 57, 58, 59, 60], many different stochastic knock control strategies, such as the likelihood-based control, the feedforward or closed-loop knock limit control, the learning-map based method, Bayesian approach, are proposed to control the knock intensity distribution presented

with the mean value and standard deviation. Zhu et al. [35, 9] unitized the ionization signal to detect the knock intensity, and proposed a stochastic closed-loop spark timing management system to maintain the knock intensity within the confidence level with MBT timing control and knock limit control. Stotsky [56] proposed a closed-loop knock control algorithm based on the statistic approach to control the spark timing moving up and down at each cycle based on the feedback error of a regulation variable and it's targeted value. In recently years, the on-board learning-based stochastic knock limit control [55, 54] has been studied as well in the literature to control the knock intensity distribution based on the real-time experimental data adaptation and estimation.

However, most of the stochastic knock control algorithms proposed in the literature are based on the real-time knock sensor measurement and knock intensity estimation. Therefore, a significant number of cycles data are generally required to obtain the accurate mean value and standard deviation for statistical analysis before the spark timing compensation by the knock controller. This process is time-cost and the control updating is too slow to operate the spark timing at the border-line knock limit with minimum knock cycle-to-cycle variability and best fuel economy. To overcome the limitations of the experimental data-based stochastic knock limit control, the model-based stochastic knock limit control demonstrates its advantages. Jones et al. [7] developed a model-based Bayesian knock event controller and the control-oriented model was an empirical model that can capture the characteristics of knock intensity distribution (mean value and deviation) after the extensively calibration with experimental data. However, the model cannot predict the physical process for the knock combustion and it requires tremendous calibrations to improve the model accuracy. Then a physical-based knock predictive model that can accurately describe the physical combustion process under knock condition and the important knock characteristics in real-time will reduce the calibration cost and is the foundation for the model-based stochastic knock limit control strategy design.

As for the knock cycle-to-cycle variability, it is influenced by many factors, but the in-cylinder mixtures intake temperature at intake valve closing (IVC) is the major one. Zhou et al. [61] studied the percentages of knock and cycle-to-cycle variation with different intake temperatures based on

extensive experiment data. The results indicated that the higher intake temperature will increase the knock occurrence percentage and significantly influence the knock cycle-to-cycle variability. Therefore, it's important that the control-oriented knock predictive model has the capability to predict the cycle-to-cycle knock variability, besides the prediction of knock onset timing and intensity of individual cycles.

This dissertation focuses on the development of the real-time combustion model and pressure wave model and model-based knock prediction and control. A control-oriented reaction-based combustion model of SI engines for real-time simulations is developed and validated first, where a two-zone combustion model is used along with the two-step chemical reaction mechanism and the reaction rate of individual species is based on the Arrhenius function. The in-cylinder thermodynamics and combustion process are modeled between IVC and exhaust valve opening (EVO). The proposed combustion model is validated against experimental data at five typical operational conditions with one set of calibration parameters and demonstrated its capability of predicting the combustion process accurately. Based on this reaction-based combustion model, a control-oriented knock pressure wave model capable of predicting the major characteristics of knock phenomenon in real-time is developed and validated. The proposed 0-D reaction-based real-time knock pressure wave model capable of predicting the knock onset timing and in-cylinder pressure wave (used to predict knock frequency and intensity) under knock combustion. Furthermore, the cycle-by-cycle knock variability is also demonstrated by the proposed model.

Consequently, this dissertation studies the stochastic knock limit control based on the control-oriented physical-based knock predictive model that consists of the combustion and the pressure wave models. Comparing with the experimental data-based knock control methods, the physical model-based knock prediction and control has the significant improvement of control compensation efficiency with minimum time cost, and makes it possible to compensate the spark timing of each cycle and operate the engine at the border-line knock limit as close to MBT timing as possible.

1.3 Dissertation Contributions

The main contributions of this dissertation are:

(1) The proposed 0-D two-zone two-step chemical reaction combustion model capable of predicting MFB, HRR, in-cylinder pressure, along with thermodynamic properties of individual species such as their chemical reaction rates, associated molar concentrations, and concentration variation rates, and so on. Furthermore, the developed model is calibrated under five different engine operating conditions using one set of calibration parameters. That is, the model does not need to be recalibrated under different operating conditions, which is very important for model-based control.

(2) The proposed 0-D reaction-based real-time knock pressure wave model capable of predicting the knock onset timing and in-cylinder pressure oscillation wave under knocking combustion that can be used to predict knock frequency and intensity. Especially, the cycle-by-cycle knock variability is also demonstrated by the proposed pressure wave model.

(3) The development of the model-based stochastic knock limit control strategy to maintain the knock intensity within a desired bound defined by the targeted mean value and standard deviation of cyclic knock intensity as close to MBT timing as possible. A strong correlation between cycle-to-cycle knock variability and in-cylinder mixtures intake temperature is obtained based on the knock predictive model. And two different model-based stochastic knock limit control strategies are proposed and validated to maintain the knock intensity below the designed bound as close to MBT timing as possible.

1.4 Dissertation Organization

This dissertation is organized as follows. In Chapter 2, a control-oriented two-zone reaction-based combustion model is developed, calibrated and validated against the experimental data collected from 5 typical engine operating conditions. In detail, the outline of the proposed model is discussed by addressing the mass and heat transfer interaction on the boundary layer of the two zones and the chemical reaction rates of individual species based on the Arrhenius function, along with thermodynamic states and properties in two zones. Next, a four cylinder SI engine experimental

data is used to validate the developed model, and a calibration method, based on the parameter sensitivity analysis, is also presented. Then in Chapter 3, a zero-dimensional real-time pressure wave model is developed and validated based on the combustion model developed in Chapter 2 for knock prediction. In detail, a 0-D pressure wave equation for modeling the in-cylinder pressure oscillations is derived first. Then the boundary and initial conditions used for deriving the pressure wave equation is further discussed. Next, the Arrhenius integral for predicting knock onset and knock intensity are discussed and the proposed model is calibrated using the experimental data from a four cylinder SI engine under knocking combustion. The simulation results are presented to show the model's capability of predicting the knock onset, knock frequency and intensity under different engine operating conditions. The knock cycle-to-cycle variability is also analyzed using both experimental data and model simulation results, and simulation results confirm its capability of predicting the cycle-by-cycle variability. In Chapter 4, the correlations of knock cycle-to-cycle variability with in-cylinder mixtures intake temperature as long as the spark timing are studied separately based on the knock predictive model. Then a knock predictive model-based feedforward stochastic knock limit control strategy is proposed and the control performance in operating the engine at the border-line knock limit with MBT timing constraint, and reducing the knock cycle-to-cycle variability is validated with simulation results. Furthermore, a closed-loop control strategy is further proposed, including the feedforward control strategy and a PI controller in the feedback loop to compensate the spark timing with the feedback error of three standard deviation confidence limit and a pre-defined targeted threshold. The control performance of the feedforward and closed-loop stochastic knock limit control strategies are compared. The conclusions and further work are discussed in Chapter 5.

CHAPTER 2

TWO-ZONE REACTION-BASED COMBUSTION MODELING

The proposed model focuses on predicting the in-cylinder combustion process for a four-stroke SI engine between IVC and EVO. It is assumed that the fresh air, fuel, and residual-exhaust-gas (REG) from the last combustion cycle are homogeneously mixed in the cylinder at IVC. Between IVC and EVO, the combustion chamber is divided into two zones: unburned and burned (reaction). The two zones are assumed to be hemisphere-shaped and both have heat losses to the cylinder wall; see the right drawing in Figure 2.1. Since the in-cylinder combustion chamber shape is not hemisphere (see the left drawing in Figure 2.1), in the combustion model, the volumes of burned and unburned zones indicated in the left drawing in Figure 2.1 are matched with these in the right drawing in Figure 2.1, respectively. An initial 1.5% of total fresh air and fuel mixture is assigned to the ignition zone at IVC and after ignition it becomes the initial reaction zone mass. The REG and the rest of total fresh air and fuel mixture are assigned to both ignition and unburned zones initially. After the spark, combustion starts in the reaction zone and the gas mixture in the unburned zone flows into the reaction zone to burn. It is further assumed that the chemical reaction products stay in the reaction zone, and as a result, it expands with the flame propagation.

The interactions between two zones include heat and mass transfer, which makes it easier to simulate the actual combustion process, flame propagation, and temperate difference. Furthermore, different from the traditional empirical Wiebe-based combustion model, a two-step chemical reaction kinetic mechanism is used in this paper to calculate the chemical reaction rates during the combustion process. The molar concentration and concentration variation rate of each individual species in the reaction zone during the entire combustion process are calculated, making it possible to study the detailed combustion process such as MFB, HRR, chemical reaction rates, flame speed, zone temperatures, and pressure.

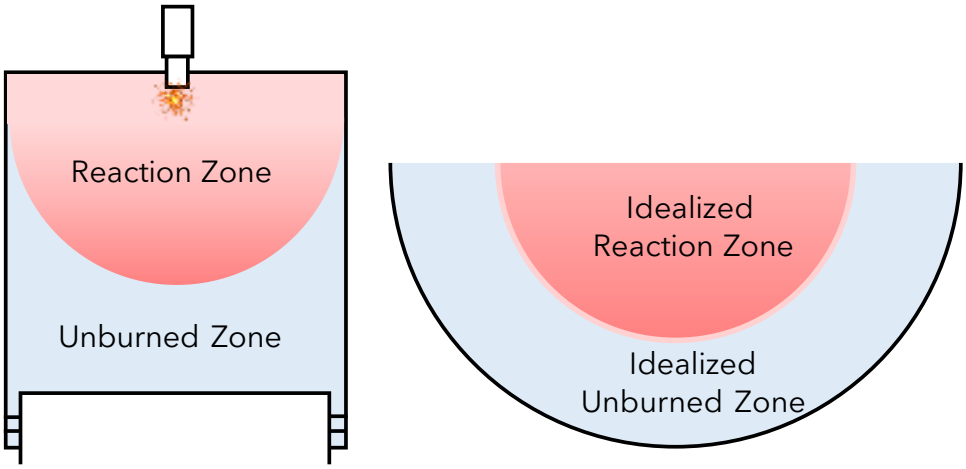

Figure 2.1: Two-zone combustion model structure

2.1 Two-Zone Model Configuration

The combustion chamber is assumed to be divided into two zones as shown in Figure 2.1. The flame front separates the two zones, and the reaction zone is where the chemical reaction takes place and the combustion products are assumed to stay within this zone. The pre-mixed gas mixture is in the unburned zone. From the left drawing in Figure 2.1, the heat loss area of the reaction zone extends from the cylinder head to its wall; and the area of unburned zone is from the piston top to cylinder wall. This is important for modeling heat losses in the next section. The two zones interact through the interface with heat and mass transfer. The model inputs include mass of fresh air and fuel, air-to-fuel ratio (AFR), REG, chamber volume at IVC, in-cylinder pressure and temperature at IVC. As mentioned in the last section, fresh air, fuel, and REG are premixed at IVC with a known AFR, λ, and the total mass in the combustion chamber is shown below in (2.1).

$$m_{tot} = m_{air} + m_{fuel} + m_{REG} \tag{2.1}$$

where m_{REG} is the mass of residual exhaust gas trapped in the chamber. For the data used to calibrate this model for the test engine, the EGR (exhaust gas recirculation) valve is closed so the

EGR rate was set to zero in this study and only REG is considered. Note that if the EGR rate is not zero, only the REG mass needs to be modifies based on the EGR rate. In this study, with the known IVC timing, the calculate REG mass is around 7% of total mass at IVC. To initiate the combustion, ignition energy is applied to a small zone (around 1.5% of the total mass for this paper) around the spark plug gap and the combustion is initiated when the auto-ignition condition is satisfied. The small zone is called ignition zone and the associated mass is called initial ignition zone mass. Since auto-ignition is assumed in the ignition zone, the combustion in the ignition zone completes in one simulation step and the ignition zone becomes the reaction zone after the combustion is completed and the initial ignition zone mass becomes the initial mass of reaction zone.

The total cylinder volume V_{cyl} and its rate of change $\dot{V}_{cyl}$ can be obtained from the typical piston motion law [62] below.

$$V_{cyl} = V_c \left(1 + \frac{r_c - 1}{2}\left[R + 1 - \cos\theta - \sqrt{R^2 - \sin^2\theta}\right]\right) \tag{2.2}$$

$$\dot{V}_{cyl} = \frac{(r_c - 1)V_c}{2} \sin\theta \left(1 + \frac{\cos\theta}{\sqrt{R^2 - \sin^2\theta}}\right) \frac{d\theta}{dt} \tag{2.3}$$

where θ is the crank angle; r_c is the compression ratio; R is the ratio of connecting rod length and crank radius; and V_c is the clearance volume. Therefore, assuming the mixtures in both zones are homogeneous, the unburned zone volume V_u can be calculated first based on the ideal gas law, and the volume rate of change $\dot{V}_u$ can be derived from V_u; see below.

$$V_u = \frac{m_u R_u T_u}{p M W_u}, \dot{V}_u = \frac{dV_u}{dt} \tag{2.4}$$

where m_u, T_u, and MW_u are mass, temperature and average molecular weight of the unburned zone mixture, respectively; p is the in-cylinder pressure; R_u (8.314 J/K-mol) is the universal gas constant.

Therefore, the reaction zone volume V_r and its rate $\dot{V}_r$ can be derived as

$$V_r = V_{cyl} - V_u, \dot{V}_r = \dot{V}_{cyl} - \dot{V}_u \tag{2.5}$$

Detailed interaction between two zones is shown in Figure 2.2 and the associated formulas used to calculate the mixture characteristics in each zone will be discussed in the next few subsections.

2.2 Interaction between Two Zones

Heat and mass transfer between two zones and heat loss from two zones to the cylinder boundary are very important to obtain an accurate combustion model since the thermodynamic properties in each zone are based on heat loss, heat and mass transfer.

2.2.1 Heat Transfer Interface

Between IVC and spark ignition, there is no heat and mass transfer at the interface between unburned and reaction (ignition) zones. As a result, the mass and volume ratio of two zones remain unchanged. With the added spark energy, the combustion is initiated in the reaction (ignition) zone and the model transits to the combustion phase. During the combustion phase, the flame stays within the reaction zone with a radius of R_r and propagates towards the unburned zone. As is shown in Figure 2.2, the heat release from the chemical reaction results in a fast increment of the reaction zone temperature T_r, and the temperature difference between the two zones leads to the heat transfer $\dot{Q}_{tr}$ from the reaction to unburned zone.

Physically, the mass in the interface of two zones will be heated up much faster than the rest of mixture in the unburned zone. Therefore, it is assumed that there is a very thin virtual region (the green area in Figure 2.2) between two zones. This virtual region is homogeneous but the temperature is much higher than that of unburned zone. After the start of combustion, the total heat transfer from the reaction zone is divided into two parts, where part one, $\dot{Q}_m$, is used to heat the mixture in the virtual region into T_r so that the associated mass in this region can be moved into the reaction zone and this process is called the mass transfer process; part two, $\dot{Q}_t$, is used to heat the mass in the rest of unburned zone.

The total heat transfer $\dot{Q}_{tr}$ from the reaction to unburned zone can be calculated based on the following equation.

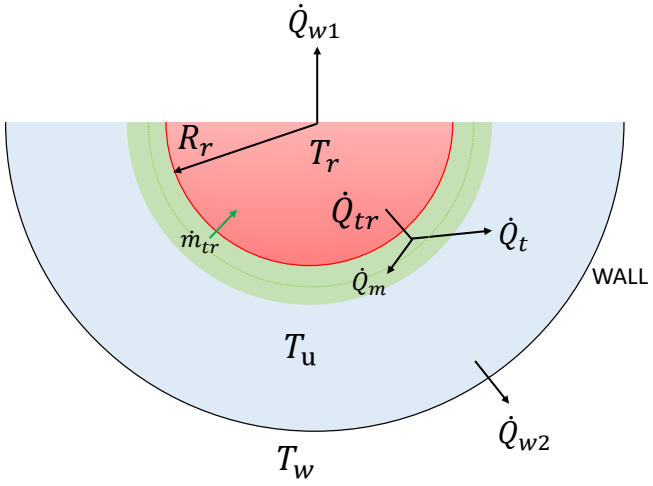

Figure 2.2: Interaction between reaction and unburned zones

$$\dot{Q}_{tr} = k_c A_{tr} \frac{T_r - T_u}{R_r} \tag{2.6}$$

where k_c is the heat coefficient to be calibrated; A_{tr} is the effective contact area between two zones; R_r is the radius of the reaction zone. Since the two zone temperatures are assumed to be homogeneous, the temperature gradient distance for the heat transfer $\dot{Q}_{tr}$ is physically from the center of the reaction zone to the average radius of the virtual region; see the dash-line in Figure 2.2. However, the virtual region is assumed to be a very thin layer, and as a result, the R_r is used as the temperature gradient distance in this paper.

A_{tr} can be calculated by (2.7) below.

$$A_{tr} = 2\pi {R_r}^2 \tag{2.7}$$

To calculate heat transfer, $\dot{Q}_m$, assume that the temperature in the virtual region (green thin layer in Figure 2.2) is T_g that is an average temperature of reaction and unburned zones weighted

by the mass and specific heat coefficient associated with the corresponding zone.

$$T_g = \frac{m_r c_{p,r} T_r + m_u c_{p,u} T_u}{m_r c_{p,r} + m_u c_{p,u}} \tag{2.8}$$

where T_r, m_r and $c_{p,r}$ are the temperature, mass and specific heat of the mixtures in the reaction zone; T_u, m_u and $c_{p,u}$ are the same parameters for the unburned zone, respectively. As a result, the heat transfer from the reaction zone to the virtual thin layer is

$$\dot{Q}_m = k_c A_{tr} \frac{T_r - T_g}{R_r} \tag{2.9}$$

Substituting (2.8) to (2.9) yields

$$\dot{Q}_m = k_c A_{tr} \frac{T_r - T_u}{R_r} \frac{m_u}{m_r + m_u} = \frac{m_u}{m_r + m_u} \dot{Q}_{tr} \tag{2.10}$$

As a result, the remaining heat transfer $\dot{Q}_t$ used to increase the unburned zone temperature can be derived as

$$\dot{Q}_t = \dot{Q}_{tr} - \dot{Q}_m = \frac{m_r}{m_u + m_r} \dot{Q}_{tr} \tag{2.11}$$

As discussed in the last few subsections, it is assumed that there is no mass transfer between the two zones until combustion is initiated. Physically, the mass transfer rate is high at the beginning of combustion phase and low at the end of combustion. Equations (2.10) and (2.11) indicate that there is no temperature difference between two zones before combustion is initiated ($\dot{Q}_{tr} = 0$), resulting in $\dot{Q}_m = 0$ and $\dot{Q}_t = 0$ during the compression process. During the combustion phase, the fraction $m_u/(m_u + m_r)$ in (2.10) dominates the heat transfer for mass transfer. On the other hand, during the fast combustion phase, the fraction $m_r/(m_u + m_r)$ in (2.11) dominates the heat transfer and causes the increment of the unburned zone temperature.

2.2.2 Heat Loss

Heat loss affects the thermal stratification inside the cylinder and the combustion characteristics [11].The heat loss in this model includes two parts. One is the heat loss from the reaction zone

to the cylinder head and liner, which dominates heat loss during the combustion phase, and is represented by $\dot{Q}_{w1}$. The other part is the heat loss from the unburned zone to the piston crown and the remaining cylinder liner, and is represented by $\dot{Q}_{w2}$; see Figure 2.2.

To reduce the computational load for this real-time combustion model, the heat loss model is simplified and the Woschni's formula [63] is used to calculate both heat losses, $\dot{Q}_{w1}$ and $\dot{Q}_{w2}$ below.

$$\dot{Q}_{w1} = h_{c1} A_{w1} (T_r - T_w) \tag{2.12}$$

$$\dot{Q}_{w2} = h_{c2} A_{w2} (T_u - T_w) \tag{2.13}$$

where h_{c1} and h_{c2} are the heat transfer coefficients; T_r, T_u and T_w are the temperature of the reaction zone, unburned zone and the cylinder boundary, respectively. Note that the temperature of the cylinder boundary (cylinder head, cylinder liner, piston head) is assumed to be the same and constant. A_{w1} and A_{w2} are the contacting area for the heat loss between the associated zone and the cylinder boundary, respectively.

The reaction zone is a very small hemisphere initially, and then starts expanding due to the flame propagation after the ignition. Therefore, the contacting area A_{w1} between the reaction zone and the cylinder boundary increases as well; see Figure 2.1. As the two zones are assumed in the hemisphere shape based on the characteristic of the flame propagation, both physical chambers shown on the left of Figure 2.1 can be transferred to the hemisphere shapes (shown in the right drawing of Figure 2.1) with the matched volumes, respectively. And it is assumed that the heat loss from the reaction zone to the wall is only through the base surface of the reaction zone in hemisphere shape. As a result, A_{w1} can be calculated based on the geometry below.

$$A_{w1} = \pi {R_r}^2 \tag{2.14}$$

where R_r is the radius of the reaction zone. Note that the base surface of reaction zone A_{w1} is not limited by the cylinder head but will consistently increase with the volume of the reaction zone.

The contacting area from the unburned zone to the rest of cylinder boundary A_{w2} decreases as the flame propagates and is given by

$$A_{w2} = A_p + A_{ch} + A_h - A_{w1} \tag{2.15}$$

where A_p is the piston crown surface area; A_{ch} is the cylinder liner area; and A_h is the cylinder head surface area. The heat transfer coefficients h_{c1} and h_{c2} are given by [30]

$$h_{c1} = \alpha B^{-0.2} p^{0.8} T_r^{-0.55} (2.28 S_p)^{0.8} \tag{2.16}$$

$$h_{c2} = \beta B^{-0.2} p^{0.8} T_u^{-0.55} (2.28 S_p)^{0.8} \tag{2.17}$$

where α and β are calibration constants; and S_p is the piston velocity equal to $\dot{V}_{cyl}/A_p$.

2.2.3 Mass Transfer

As mentioned above, the heat transfer rate $\dot{Q}_m$ causes the mass transfer between two zones during the combustion process. If mass flow rate $\dot{m}_{tr}$ were too large, the modeled combustion would be unstable; and if it were too slow, the combustion might not continue. Therefore, the mass transfer rate between two zones is a key parameter to be modeled and it is calculated by the following equation.

$$\dot{m}_{tr} = \frac{k_m \dot{Q}_m}{c_{p,u} \Delta T_0} \tag{2.18}$$

where k_m is the mass coefficient; and ΔT_0 is a constant associated with temperature increment. Both parameters need to be calibrated based on the experimental data. $c_{p,u}$ is the specific heat of the gas mixture in the unburned zone and will be discussed in the next subsection.

2.3 Chemical Reaction Kinetic Mechanism

The mixture in the unburned zone consists of fresh air, fuel, and REG trapped in the combustion chamber from the last cycle. The initial reaction zone size is about 1~2% of the total mass, and each species in the mixture changes during the combustion. It is assumed that the mixtures in both zones are homogeneous. The composition and thermodynamic properties of mixtures in both zones are determined by the in-cylinder pressure, zone temperature, AFR, and zone volumes [64]. Based on the chemical kinetic mechanism, the properties of each species in each zone can be studied. And with a two-step chemical reaction mechanism, the detailed combustion process can be modeled.

2.3.1 Molar Concentration and its Concentration Rate:

The molar concentration and its concentration variation rate of each individual species are the foundation for studying the chemical reaction process and thermodynamic properties of the mixture. The mixture in the unburned zone consists of 5 chemical species and they are C_8H_{18}, O_2, N_2, CO_2, and H_2O. Due to the two-step chemical reaction mechanism, the reaction zone has one more chemical species, CO, generated during the reaction process. Therefore, there are 6 species: C_8H_{18}, O_2, N_2, CO_2, H_2O, and CO in the reaction zone.

The molar concentration $[X_i]$ (moles per unit volume) of species i is defined by

$$[X_i] = \frac{N_i}{V} \tag{2.19}$$

where i stands for different species in each zone; N_i is the associated molecular number of species i, where $N_i = m_i/MW_i$ and V is the associated zone volume.

The molar concentration of each species $[X_i]$ changes during the combustion process and the associated zone volume also changes due to the piston movement. Therefore, the rate of change for the molar concentration $[X_i]$ is denoted by $[\dot{X}_i]$ (kmol/m^3·s) and given by

$$
\begin{aligned}
[\dot{X}_i] &= \frac{d[X_i]}{dt} = \frac{d(N_i/V)}{dt} \\
&= \frac{1}{VMW_i}\frac{dm_i}{dt} - N_i\frac{1}{V^2}\frac{dV}{dt}
\end{aligned}
\tag{2.20}
$$

The first term on the right side of (2.20) accounts for the mass change. The mass change in a zone is driven by two factors: mass transfer between two zones and chemical reaction. During the chemical reaction process, the masses of reactants and products keep changing until the reaction is ended. The second term reflects the effect of volume change to the molar concentration.

The mass change term is defined below.

$$
\frac{1}{VMW_i}\frac{dm_i}{dt} = \omega_i = \omega_{flow,i} + \omega_{chem,i} \tag{2.21}
$$

where $\omega_{chem,i}$ (kmol/m^3·s), reaction rate, is used to reflect the effect of chemical reaction. And the Arrhenius Law [64] is used in this model to calculate the reaction rate $\omega_{chem,i}$. This part will be addressed next. Note that $\omega_{flow,i}$ accounts for the effect of mass transfer for the concentration rate of species i and can be calculated based on the mass transfer rate $\dot{m}_{tr}$.

$$
\omega_{flow,i} = \begin{cases} \frac{-x_{u,i}\dot{m}_{tr}}{V_u MW_u} & \text{in the unburned zone} \\ \frac{x_{u,i}\dot{m}_{tr}}{V_r MW_u} & \text{in the reaction zone} \end{cases} \tag{2.22}
$$

where $x_{u,i}$ is the molar fraction of each species in the unburned zone; MW_u is the average molecular weight of the unburned zone mixture to be discussed in the next subsection.

2.3.2 Two-Step Chemical Reaction Mechanism:

A simplified but practical chemical reaction mechanism for the combustion process is always desired. In recent literature, the one-step reaction between reactants and products is widely used to achieve this goal. However, the one-step reaction mechanism is not able to describe the flame propagation process from lean to rich combustion [64]. The main weakness of this one-step reaction mechanism is the neglect of CO produced in the combustion process. Since in the typical

hydrocarbon flames, large amount of CO and H_2 exists in the equilibrium with CO_2 and H_2O, while the CO oxidation is also a rather slow process [64, 65]. Therefore, a two-step chemical reaction mechanism is proposed in the reaction zone to account for the influence of the CO oxidation process. The specific reaction steps are shown below.

$$C_8H_{18} + \frac{17}{2}O_2 \xrightarrow{k_1} 8\,CO + 9\,H_2O \tag{M1}$$

$$CO + \frac{1}{2}O_2 \underset{k_3}{\overset{k_2}{\rightleftharpoons}} CO_2 \tag{M2}$$

where the proportionality factor k_i ($i = 1, 2, 3$) is the specific reaction rate constant dominated by the temperature [65].

The rate of the first step reaction (M1) is given by

$$\omega_{M1} = k_1[C_8H_{18}]^{n_1}[O_2]^{n_2} \tag{2.23}$$

where $[C_8H_{18}]$ and $[O_2]$ are molar concentrations of species fuel and species O_2, respectively; and n_1 and n_2 are associated reaction order and are empirically determined.

For the second step chemical reaction (M2), since it is a reversible reaction, the net reaction rate is given by

$$\omega_{M2} = k_2[CO]^{n_3}[O_2]^{n_4} - k_3[CO_2]^{n_5} \tag{2.24}$$

where the first and second terms on the right side are the forward and backward reaction rates of M2, respectively; [CO] and $[CO_2]$ are molar concentrations of CO and CO_2, respectively; and $n_3 \sim n_5$ are associated reaction order and are also empirically determined.

The specific reaction rate constant k_i ($i = 1, 2, 3$) in M1 and M2 are calculated based on the Arrhenius Law [64].

$$k_i = A_i e^{-E_{a,i}/R_u T} \tag{2.25}$$

where $E_{a,i}$ is the activation energy of the reaction (J/mol); A_i is the pre-exponential factor; $E_{a,i}$ and A_i are constant and to be calibrated. As activation energy E_a and the universal gas constant R_u are constant, the activation temperature T_a can be defined as

$$T_{a,i} = \frac{E_{a,i}}{R_u} \tag{2.26}$$

Based on (2.23) and (2.24), the production rates of each species are

$$\boldsymbol{\Omega}_{chem} = \boldsymbol{s}_{5\times2} \cdot \boldsymbol{\omega}_{2\times1} \tag{2.27}$$

where $\boldsymbol{\Omega}_{chem}$ is the production rate vector of the species; $\boldsymbol{s}_{5\times2}$ is the stoichiometric coefficient matrix; and $\boldsymbol{\omega}_{2\times1}$ is the reaction rate vector for M1 and M2; see below.

$$\boldsymbol{\Omega}_{chem} = (\omega_{\mathrm{C_8H_{18}}} \quad \omega_{\mathrm{O_2}} \quad \omega_{\mathrm{CO_2}} \quad \omega_{\mathrm{H_2O}} \quad \omega_{\mathrm{CO}})^{\intercal} \tag{2.28}$$

and

$$\boldsymbol{s}_{5\times2} = \begin{bmatrix} -1 & 0 \\ -\frac{17}{2} & -\frac{1}{2} \\ 0 & 1 \\ 9 & 0 \\ 8 & -1 \end{bmatrix}, \boldsymbol{\omega}_{2\times1} = \begin{bmatrix} \omega_{M1} \\ \omega_{M2} \end{bmatrix} \tag{2.29}$$

2.3.3 Zone Temperature

Based on the second-law of thermodynamics, conservation of mass, conservation of energy, and the chemical kinetic mechanism discussed above, the temperature rate of change for the reaction zone can be derived below.

$$\dot{T}_r = \frac{\frac{\dot{Q}_r}{V_r} + R_u T_r \Sigma[\dot{X}_i] - \Sigma[\dot{X}_i]\bar{h}_i - \frac{\dot{V}_r}{V_r}\Sigma[X_i]\bar{h}_i + \frac{\Sigma(\dot{N}_i\bar{h}_i)}{V_r}}{\Sigma[X_i](\bar{c}_{p,i} - R_u)} \tag{2.30}$$

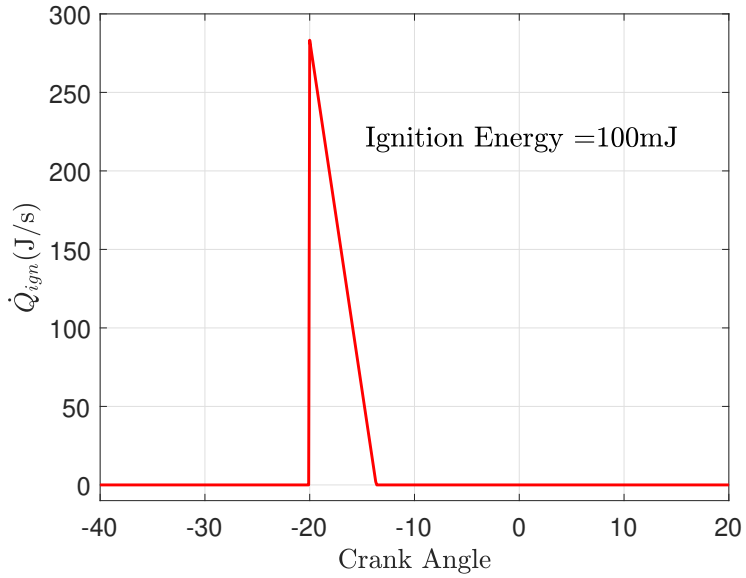

Figure 2.3: Ignition energy profile used

where $\bar{h}_i$ and $\bar{c}_{p,i}$ are molar enthalpy (kJ/kmol) and molar specific heat (kJ/kmol·K) of species i, respectively, with respect to temperature; and $\dot{Q}_r$ (kJ/s) is the net heat transfer rate for the reaction zone defined by

$$\dot{Q}_r = \dot{Q}_{ign} - \dot{Q}_t - \dot{Q}_{w1} \tag{2.31}$$

Note that $\dot{Q}_{ign}$ (kJ/s) is the rate of provided ignition energy. Figure 2.3 provides a sample ignition energy profile for $\dot{Q}_{ign}$ used in the proposed model, where the total ignition energy is 100 mJ with a duration of 6 crank angle degrees (CADs).

The formula used to calculate the unburned zone temperature T_u is similar to those for the reaction zone. However, since there is no chemical reaction in the unburned zone, the molar concentration rate ($[\dot{X}_i]$) formula for the unburned zone needs to be modified. Note that no chemical reaction in the unburned zone means that the reaction rate of each species is zero ($\omega_{chem,i} = 0$). As a result, the change of molar concentration is caused by the mass transfer and volume change only. Therefore, (2.20) and (2.21) can be modified and combined; see below.

$$[\dot{X}_i] = \frac{\dot{m}_i}{V_u MW_i} - \frac{N_i \dot{V}_u}{V_u^2} = \omega_{flow,i} - \frac{N_i \dot{V}_u}{V_u^2} \tag{2.32}$$

Thus, the unburned zone temperature rate $\dot{T}_u$ is

$$\dot{T}_u = \frac{\frac{\dot{Q}_u}{V_u} + R_u T_u \Sigma[\dot{X}_i] - \Sigma[\dot{X}_i]\bar{h}_i - \frac{\dot{V}_u}{V_u}\Sigma[X_i]\bar{h}_i + \frac{\Sigma(\dot{N}_i \bar{h}_i)}{V_u}}{\Sigma[X_i](\bar{c}_{p,i} - R_u)} \tag{2.33}$$

where $\dot{Q}_u$ is the unburned zone net heat transfer rate and is given by

$$\dot{Q}_u = \dot{Q}_t - \dot{Q}_{w2} \tag{2.34}$$

2.3.4 In-Cylinder Pressure

With the known temperature, mass, and volume of each zone, the cylinder pressure can be calculated by the ideal gas law below.

$$\bar{p} = \frac{m_{tot} R_u T_{avg}}{V_{cyl} MW_{mix}} \tag{2.35}$$

where MW_{mix} is the average molecular weight of in-cylinder mixture and can be weighted by the mass and specific heat of the mixture in each zone; see below.

$$MW_{mix} = \frac{m_r c_{p,r} MW_r + m_u c_{p,u} MW_u}{m_r c_{p,r} + m_u c_{p,u}} \tag{2.36}$$

Note that MW_u and MW_r are the average molecular weight of the mixture in the reaction and unburned zones, respectively. Since the chemical reaction happens in the reaction zone, it is assumed that MW_u is constant throughout the combustion cycle and MW_r varies due to the chemical reaction in the reaction zone. As a result, MW_u can be computed by

$$MW_u = \sum x_{u,i} MW_i \tag{2.37}$$

where $x_{u,i}$ and MW_i are the mole fraction and molecular weight of each species i, respectively, in the unburned zone and they remain unchanged throughout the combustion process.

However, MW_r changes during the combustion process and can be derived as

$$MW_r = \frac{\sum m_i MW_i}{\sum m_i} \tag{2.38}$$

where i is the species in the reaction zone; m_i and MW_i are the associated mass and molecular weight, respectively.

T_{avg} in (2.35) is the overall temperature of the mixture in the cylinder weighted by the mass and specific heat of mixtures in each zone; see below

$$T_{avg} = \frac{m_r c_{p,r} T_r + m_u c_{p,u} T_u}{m_r c_{p,r} + m_u c_{p,u}} \tag{2.39}$$

where $c_{p,r}$ and $c_{p,u}$ are the specific heat of mixtures in reaction and unburned zones, respectively. $c_{p,u}$ and $c_{p,r}$ are derived as

$$c_{p,u} = \sum [X_i] \cdot \bar{c}_{p,i}(T_u) V_u \tag{2.40}$$

$$c_{p,r} = \sum [X_i] \cdot \bar{c}_{p,i}(T_r) V_r \tag{2.41}$$

where $[X_i]$ is the molar concentration of species i in the associated zone; $\bar{c}_{p,i}(T_u)$ and $\bar{c}_{p,i}(T_r)$ are the molar specific heat of each species i in the associated zone at current zone temperature, respectively.

2.4 Model Calibration

2.4.1 Experimental Investigation

The experimental data used to validate the proposed reaction-based two-zone combustion model is collected from a 4-cylinder, four-stroke SI engine through dynamometer experiments. The engine parameters are listed in Table 2.1.

The test data for five typical steady-state engine operating conditions are used for validation purpose and is summarized in Table 2.2, where the relative air-fuel ratio λ is controlled to be close to stoichiometric. At each condition, 100 cycles of engine data were collected. In order to calibrate

Table 2.1: Test engine parameters.

Parameter	Value
Bore	86 mm
Stroke	86 mm
Rod	143.6 mm
Compression ratio	11:1
Displacement	499.56 cm^3
Intake valve closing(IVC)	190°BTDC
Exhaust valve opening(EVO)	156°ATDC

the ARI coefficients for auto-ignition (knock) prediction, the ignition timing under two operational conditions (high load conditions for 1500 and 2000 rpm) are controlled to be near the engine knock limit.

Table 2.2: Engine operational conditions.

Case	1	2	3	4	5
IMEP[bar]	4.53	5.01	6.78	6.83	8.23
Engine Speed[rpm]	1100	1500	1500	2000	2000

An A&D CAS (Combustion Analysis System) is used to record in-cylinder pressure, intake manifold pressure, ignition current, etc. The average in-cylinder mixture temperature is calculated based on the recorded in-cylinder pressure and used to compare with the modeled ones.

2.4.2 Model Calibration

This section discusses the model calibration process for key model parameters and compares the simulation results with the experimental data. The model's capability of predicting the physical combustion process is demonstrated by comparing the associated simulation results of certain important combustion variables and thermodynamic states.

Based on the discussion at the end of Reaction-Based Combustion Model section, there are a set of model parameters to be calibrated empirically; see Table 2.3. These coefficients can be

grouped into two sets: low and high sensitivity parameters, where high sensitivity ones need to be calibrated carefully.

The reaction order n_j $(j = 1, 2, 3, 4, 5)$ in equations (2.23) and (2.24) and the activation energy $E_{a,i}$ $(i = 1, 2, 3)$ in the Arrhenius function (2.25) for calculating reaction rates of the two-step chemical reaction mechanism have low sensitivity and these parameters do have their recommended values verified based on standard combustion experiments. Therefore, these parameters are modified slightly from the reference values and kept unchanged with respect to the engine operating condition; see Table 2.4 for the values used.

Table 2.3: Parameters to be calibrated.

Parameter	Equation	Group
$n_j (j = 1 \sim 5)$	(2.23),(2.24)	low sensitivity
$T_{a,i} (i = 1, 2, 3)$	(2.26)	
α, β	(2.16),(2.17)	high sensitivity
k_c, k_m	(2.6),(2.18)	
$A_i (i = 1, 2, 3)$	(2.25)	

Table 2.4: Calibrated parameters with low sensitivity

n_1	n_2	n_3	n_4	n_5	$T_{a,1}$	$T_{a,2}$	$T_{a,3}$
0.25	1.5	0.3	0.25	1	15540K	17900K	28130K

There are seven parameters with high sensitivity and they are: α in (2.16) and β in (2.17) associated with the heat loss to the cylinder boundary, k_c in (2.6) with the heat transfer between two zones, k_m in (2.18) for the mass transfer through the interface between two zones, and A_i $(i = 1, 2, 3)$ in (2.25) for the two-step chemical reaction rate.

The heat loss coefficients α and β should be calibrated first under no combustion condition to make sure that the simulated pressure tracks the experimental one from IVC to spark. The simulated and experimental pressure curves with the calibrated heat loss coefficients are compared in Figure 2.4, where the simulated pressure is the dashed-line and experiment one is the solid one.

The heat transfer $\dot{Q}_{tr}$ between two zones is very important since it affects the thermodynamic properties in each zone, for instance, zone temperature, in-cylinder pressure, chemical reaction rate, and so on. Also, the mass transfer between the two zones is partially dependent on the calculated heat transfer. In this model, the heat coefficient k_c in (2.6) is the key to have accurate heat transfer.

k_m in (2.18) is the mass coefficient that governs the mass flow rate between two zones. It indicates through the calibration process that the mass transfer rate $\dot{m}_{tr}$ dominates the modeled combustion process. The accurate mass transfer rate from the unburned to reaction zone shall be calibrated well to ensure an accurate combustion process.

The pre-exponential factor A_i $(i = 1, 2, 3)$ in the Arrhenius function is the main coefficient for calibrating the two-step chemical reaction mechanism. If A_i were too large, the auto-ignition could happen before the spark, leading to pre-ignition; and if A_i were too small, the reaction rate would be too slow to start the combustion process after the spark.

The high sensitivity parameters are listed in Table 2.5 with associated calibration values. Note that these calibrated parameters are fixed under different engine operating conditions.

Table 2.5: Calibrated parameters with high sensitivity

α	β	k_m	k_c	A_1	A_2	A_3
0.978	2.608	5.2e-7	295	4.15e10	15.21e16	1.98e8

2.5 Model Validation and Simulation Results

2.5.1 Thermodynamic Properties

This subsection shows the model performance of predicting thermodynamic states in the combustion chamber, such as the in-cylinder pressure, zone temperatures and volumes, and mass transfer between two zones. Since the simulation results are pretty similar for all 5 cases listed in Table 2.2, to simplify the presentation, only the simulation results for cases 3 and 5 are shown in detail for in-cylinder pressure and temperature. For the mass transfer and zone volumes, simulation results

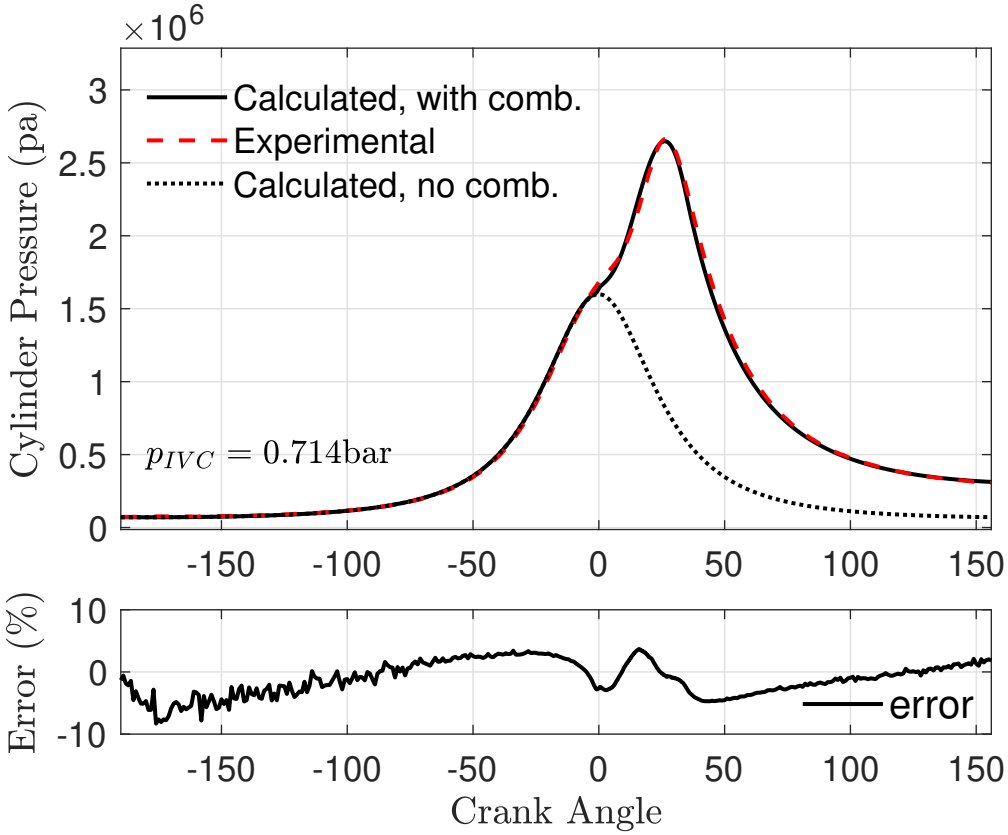

Figure 2.4: Comparison of simulated and experimental in-cylinder pressures with relative error at 1500rpm with 6.78bar IMEP (case 3)

of case 3 are used. The results for all five cases are summarized in Table 2.6 at the end of this section.

In-Cylinder Pressure:

The experimental data of 100 cycle in-cylinder pressure are averaged and used to compare with the simulated one. The experimental and simulated in-cylinder pressures of cases 3, 4 and 5 are compared in Figures 2.4, 2.5 and 2.6, respectively.

The simulated cylinder pressures for the three cases match the experimental data very well. The relative error (%) at the early stage of compression phase (within 50 CAD after IVC) is a little bit high (around 7%). However, we are interested in the error between SOC and EVO for the

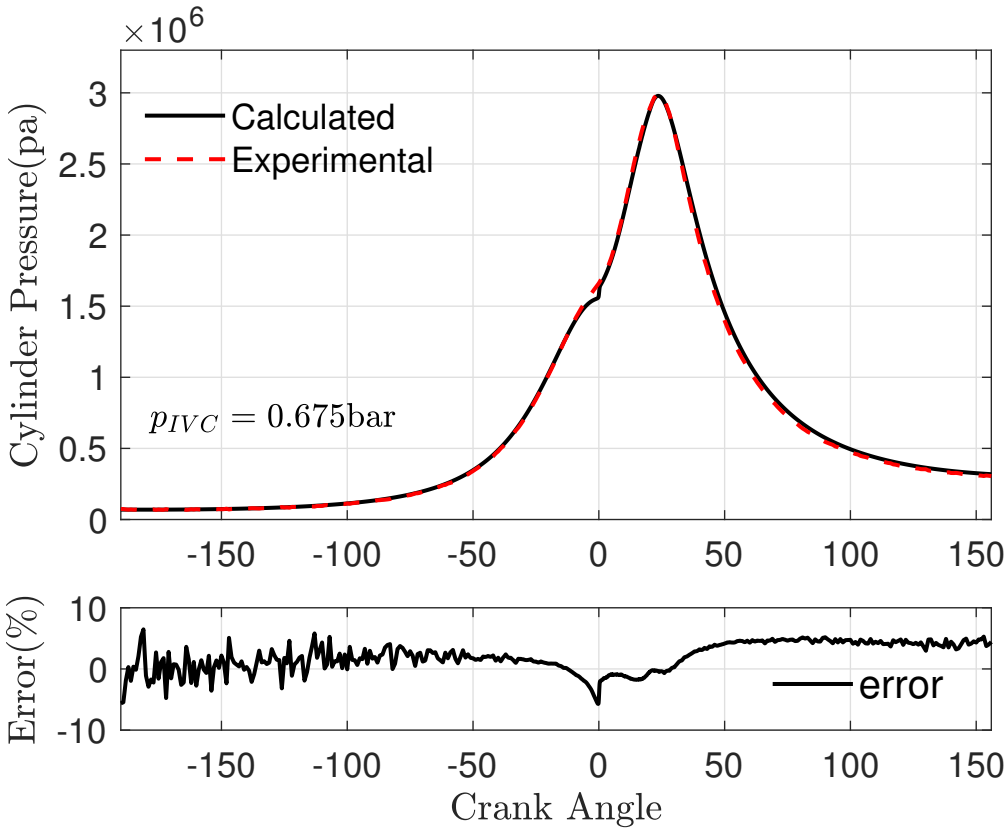

Figure 2.5: Comparison of simulated and experimental in-cylinder pressures at 2000rpm with 6.83bar IMEP (case 4)

developed combustion model. In these cases, the maximum relative error for cases 3, 4 and 5 are 4.09% (occurred at around 20 CAD after top dead center (ATDC)), 5.3% (occurred at around 0 CAD ATDC) and 5.19% (occurred at around 24 CAD ATDC), respectively.

Zone Temperature:

One of the major advantages of the proposed model is its capability of predicting temperatures in both zones. The simulation results of the unburned zone (T_u) and reaction zone (T_r) temperatures are shown in Figure 2.7 for case 3. The averaged temperature over two zones is also plotted in the same figure for comparison purpose. One can see that the two zone temperatures are the same before spark event, and after the spark, combustion starts and the heat release from chemical

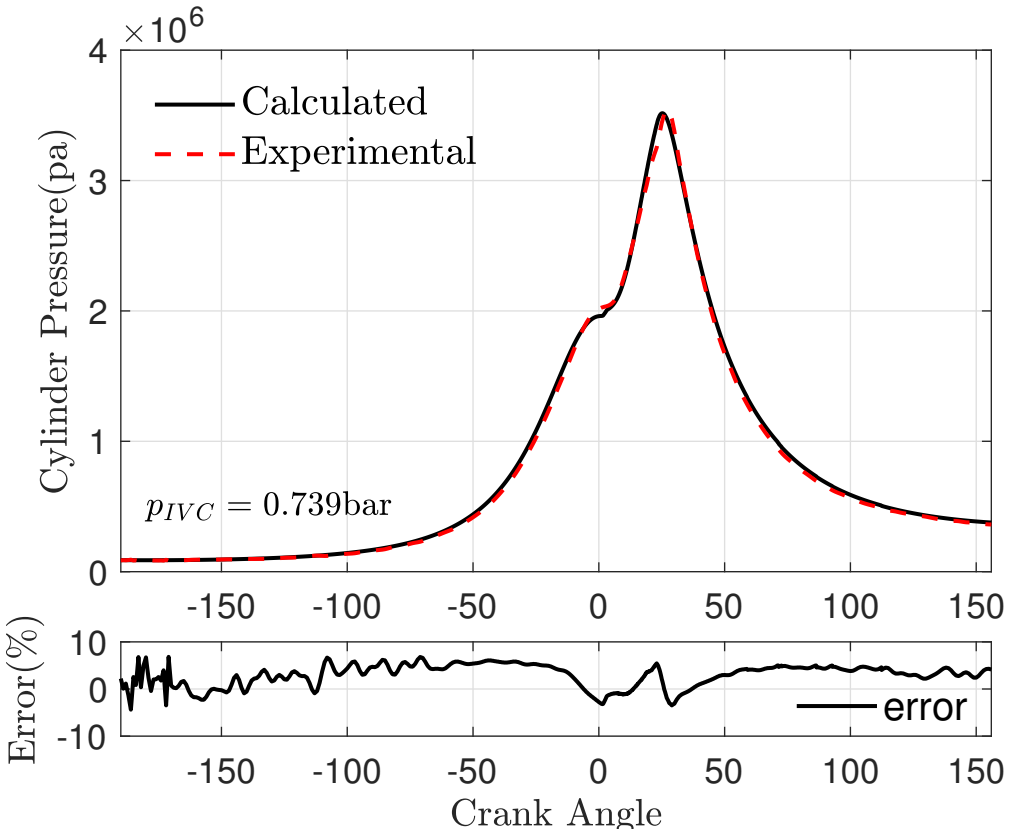

Figure 2.6: Comparison of simulated and experimental in-cylinder pressures at 2000rpm with 8.23bar IMEP (case 5)

reaction increases the reaction zone temperature T_r, while in the unburned zone, the temperature increment is much slower.

For the first half of combustion (between 20 CAD before top dead center (BTDC) and 25 CAD ATDC), over 60% of the total mass in the unburned zone is transferred to the reaction zone with very fast combustion in the reaction zone. As a result, the temperature difference between T_r and T_u increases rapidly and peaks at around 15 CAD ATDC. The chemical energy released in the reaction zone gets transferred to the unburned zone and heats up the mixture in the unburned zone, leading to a mild increment of T_u at this stage. As combustion continues, for the second-half of combustion (between 25 CAD and 40 CAD ATDC), over 95% of the mass in the unburned zone flows to the reaction zone, resulting in a fast decrement of the unburned zone size. The decreased unburned zone size with the continued heat transfer from the reaction zone increases the unburned zone

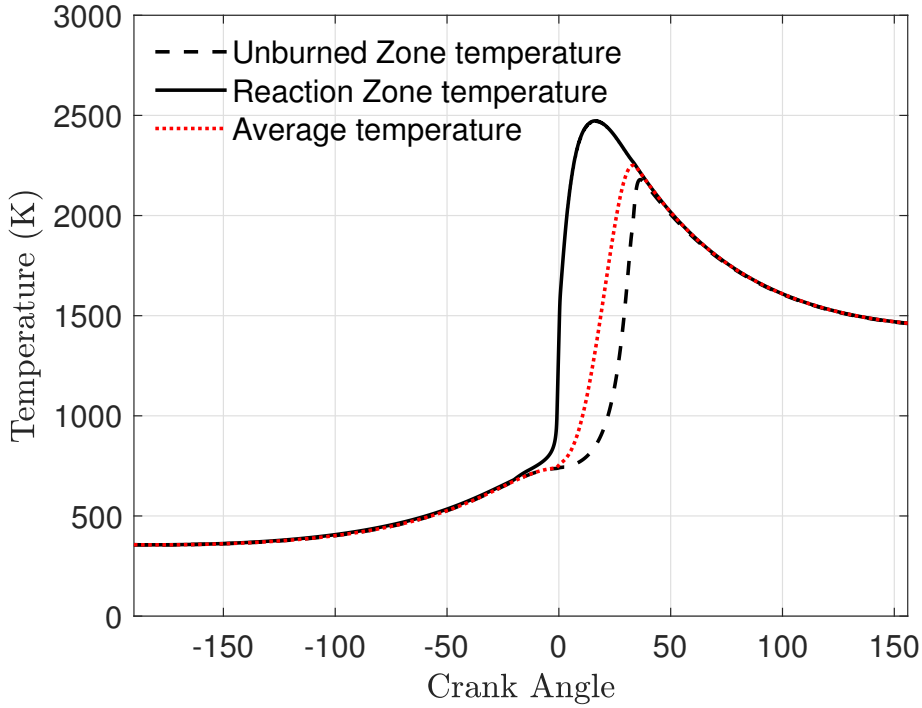

Figure 2.7: Zone and average temperatures at 1500rpm with 6.78bar IMEP (case 3)

temperature quickly and reaches its peak at the end of combustion. After the end of combustion, two zone temperatures converge, and then, decrease due to expansion.

To verify the model performance of predicting in-cylinder temperature, the simulated average temperature T_{avg} is compared with the experimental temperature calculated based on the measured in-cylinder pressure, the experimental in-cylinder temperature T_{exp} is derived using the ideal gas law based on the collected experimental in-cylinder pressure data, including the recorded in-cylinder pressure, volume of the combustion chamber and the total mass in the chamber. The comparison result and the associated error are shown in Figure 2.8. It shows that the simulated average in-cylinder temperature matches with the experimental data very well with a maximum relative error of 4.8% between SOC and EVO occurred at 45 CAD ATDC. The simulation results for case 4 are shown in Figure 2.9, where the maximum relative error, in this case, is 5.7%. Therefore, the capability of predicting the mixture temperature and thermal stratification is demonstrated.

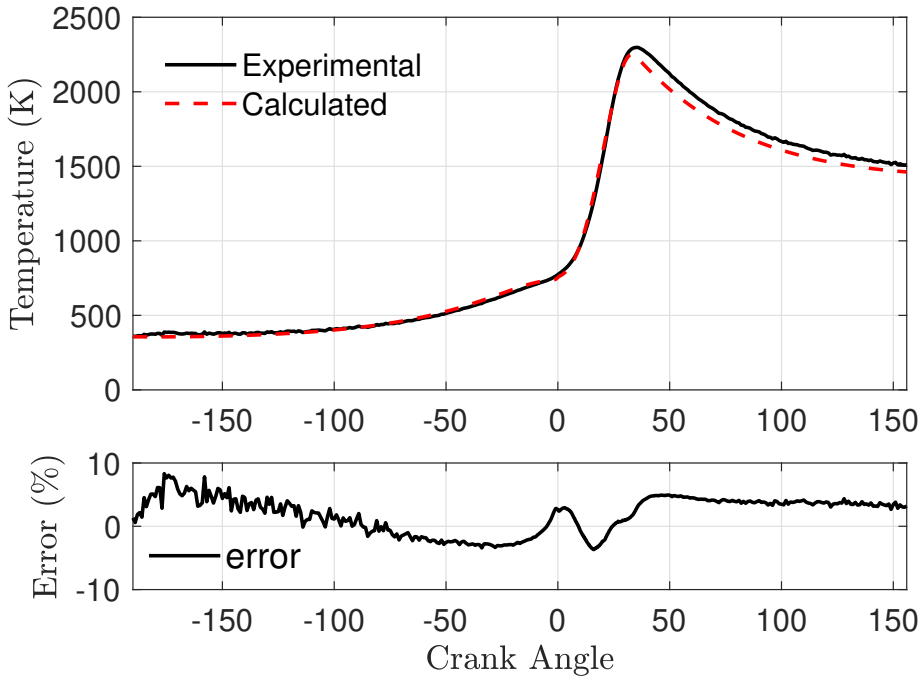

Figure 2.8: Comparison of experimental and simulated cylinder temperatures at 1500rpm with 6.78bar IMEP (case 3)

Mass Transfer:

The mass transfer between the reaction and unburned zones for case 3 are shown in Figure 2.10. As discussed earlier, for this study, the initial unburned zone mass is 98.5% of total mass and the reaction zone is 1.5%. Also, the mass transfer does not occur until combustion is initiated.

The mass transfer rate $\dot{m}_{tr}$ in Figure 2.10 indicates that the mass flow rate is zero before spark. And then, after a small ignition delay, the mass transfer starts and increases rapidly to provide a proper amount of pre-mixed mass to the reaction zone to burn. Two mass curves of the reaction and unburned zones also indicate that mass in both zones remains unchanged before and after combustion. During the combustion, the unburned zone mass decreases very quickly due to mass flow into the reaction zone.

Note that the mass transfer rate does not drop down to zero at the end of combustion. As shown in the zoomed plot in Figure 2.10, mass transfer rate goes to zero very slowly in the combustion

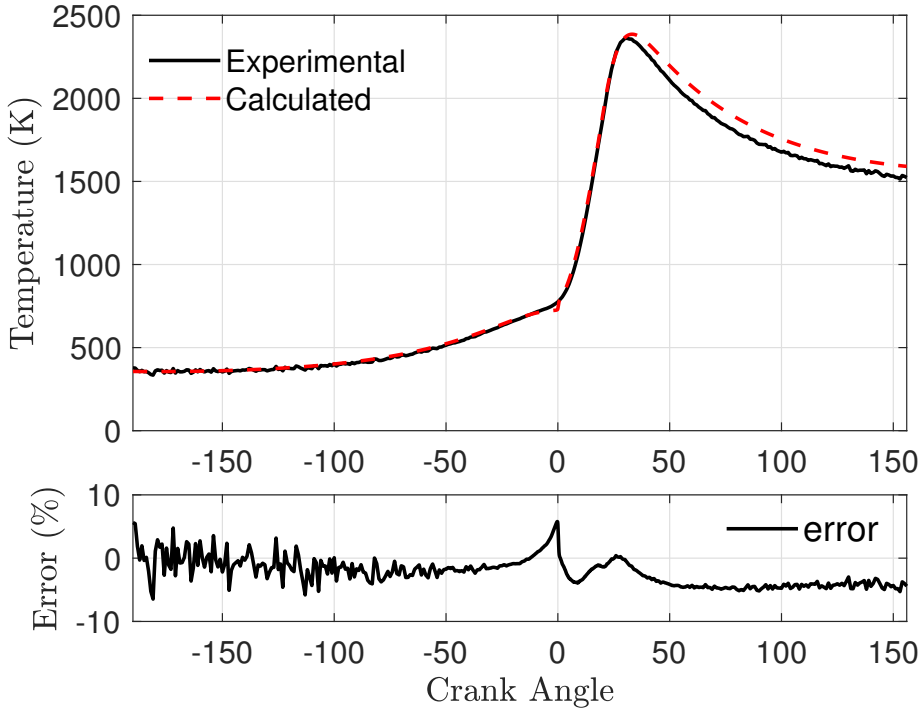

Figure 2.9: Comparison of experimental and in-cylinder average temperatures at 2000rpm with 6.83bar IMEP (case 4)

phase, resulting in a small mass flow into the reaction zone. In this case, only 97% fuel is burned.

Zone Volume:

The volume variations in the two zones are similar to mass case (in Figure 2.10) as the zone volume is governed by the ideal gas law; see Figure 2.11 (case 3).

The unburned zone volume begins decreasing after the start of combustion and the reaction zone volume keeps increasing (with an initial value of 1.5%) due to the mass transfer from the unburned zone to the reaction zone. The reaction zone volume in Figure 2.11 also indicates that the volume increases very quickly between SOC and middle of combustion, and after that, it increases slowly up to 96.9% of total volume at the end of combustion. During the engine expansion process, the volume has a slight increment from 96.9% to 99.3%, due to the small mass flow into the reaction zone (see discussions in the last subsection).

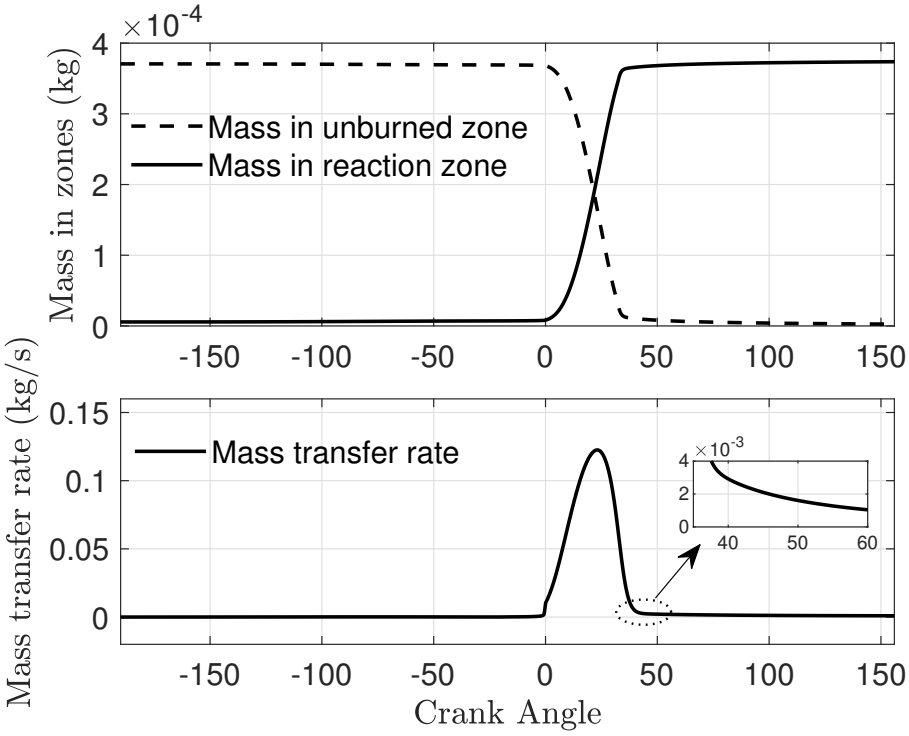

Figure 2.10: Mass transfer and its rate between two zones at 1500rpm with 6.78bar IMEP (case 3)

2.5.2 Combustion Simulation Results

The combustion characteristics of each chemical species in both zones can also be simulated in this model. The simulation results for case 3 are used as an example to discuss the model's capability of predicting the combustion process. To compare the combustion simulation results, the reaction rate ω_{chem} and mass flow-in rate ω_{flow} of fuel and O_2 in the reaction zone are shown in Figure 2.12.

As discussed earlier in the Reaction-Based Combustion Model section, the chemical reaction is modeled using a two-step reaction mechanism and CO is the products from the first reaction step. In the second step, CO gets burned to produce CO_2, and CO_2 splits into CO and $0.5O_2$. As shown in Figure 2.12, the reaction rate (in [kmol/m$^3\cdot$ s]) of fuel and O_2 is negative during the combustion phase, indicating that the fuel and O_2 are reacted. The reaction rates of these two species are zero before the SOC, and then, increase and reach the first peak, indicating that the initial mass in the

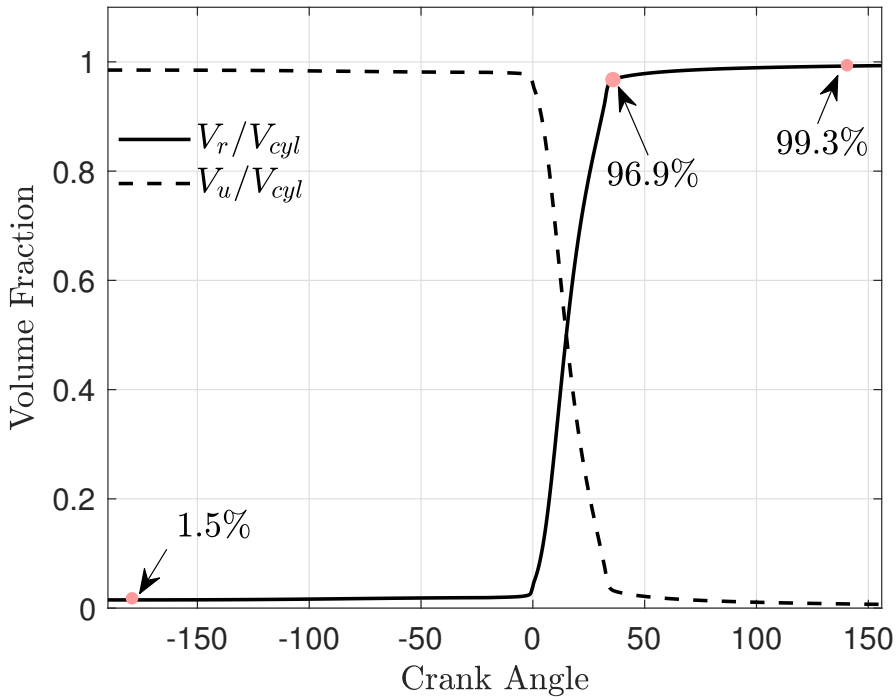

Figure 2.11: Individual volume fractions at 1500rpm with 6.78bar IMEP (case 3)

reaction zone is burned due to the added spark energy. These two peaks are mainly caused by the extremely small initial reaction zone volume (1.5% of total volume) at the start of combustion and the assumed auto-ignition in the ignition zone.

After the combustion starts, the gas mixture starts flowing into the reaction zone and gets burned continuously; see the two smooth positive mass flow (in [kmol/m$^3\cdot$ s]) curves of fuel and O_2 in Figure 2.12. The reaction rates of CO, CO_2, and H_2O changes in a similar way; see Figure 2.13 for the total mass of these species.

The total mass variation trend of each individual chemical species in the entire cylinder is a good indicator for the actual combustion process. Since N_2 takes no part in the chemical reaction, its mass keeps unchanged. The mass variations of other five chemical species (fuel, O_2, CO_2, H_2O, and CO) during the combustion process are shown in Figure 2.13. It indicates that the total fuel mass in the cylinder remains constant until SOC and drops quickly down close to zero at the end of combustion (around 38 CAD ATDC), indicating that the fuel is almost fully burned. The

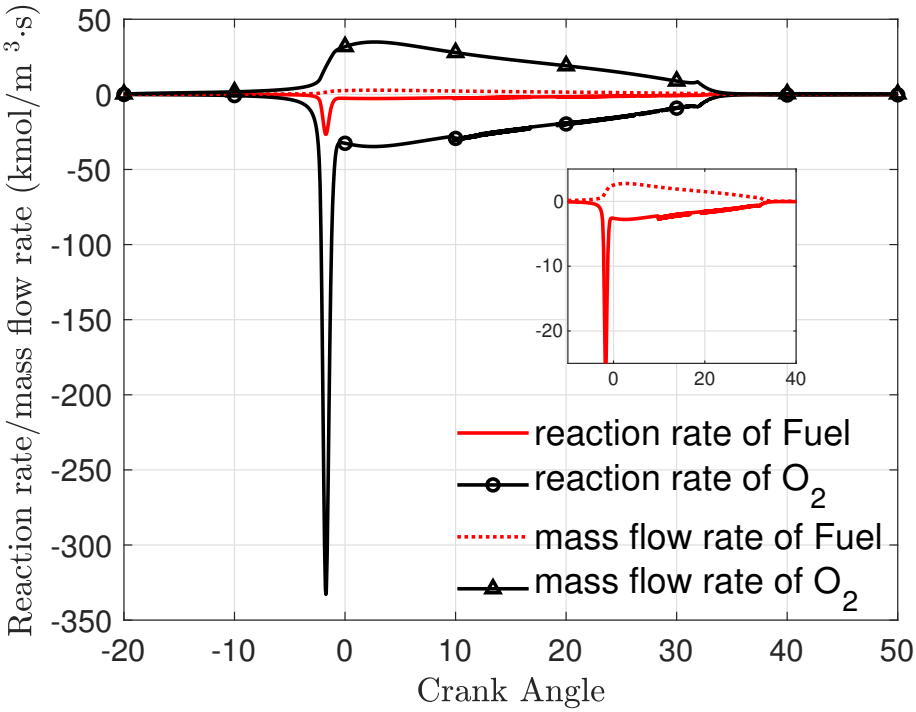

Figure 2.12: Comparison of reaction rates and mass flow rates of fuel and O_2 in the reaction zone at 1500rpm with 6.78bar IMEP (case 3)

corresponding O_2 mass is also changed in a similar way and reduces very fast, however, there is a small amount of O_2 left at the end of combustion since the actual λ was 1.05.

The total mass of species CO increases at the beginning of the combustion and gets burned in the second step. There is a small peak before TDC, which is caused by the spark. Considering the products of the two-step chemical reaction (CO_2 and H_2O), H_2O is zero before SOC and then increases rapidly during the combustion process, remains unchanged after combustion, but the mass of CO_2 has a slight increment after the combustion. By inspecting the CO curve after combustion, the total CO mass drops down to very low (near zero) level, and then, gets burned by reacting with the remaining O_2 slowly during the expansion phase, resulting in a slight increment of CO_2 during the expansion phase.

The predicted MFB of case 4 is shown in Figure 2.14. The slop of this curve shows that the burn rate is very fast from SOC to around 20 CAD ATDC, where 50% of total fuel is burned. After

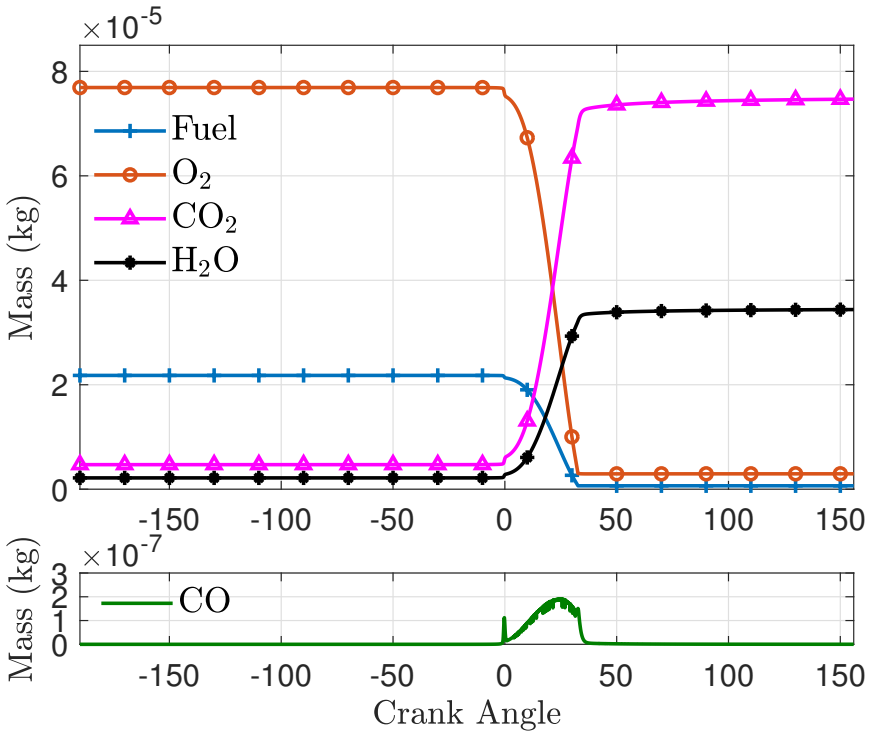

Figure 2.13: Total mass changing of species (fuel, O_2, CO_2, H_2O and CO) at 1500rpm with 6.78bar IMEP (case 3)

that, the burn rate slows down until the end of combustion.

The heat release rate, along with heat transfer related to the mass transfer ($\dot{Q}_m$) and heat transfer to the unburned zone ($\dot{Q}_t$) is shown in Figure 2.15. Comparing the $\dot{Q}_m$ and $\dot{Q}_t$ indicates that most of the total heat transfer ($\dot{Q}_m$) is used to transfer the mass from the unburned zone to the reaction zone during the first half of the combustion process, where significant part of mass is provided to the reaction zone. After that, during the late phase of combustion, the heat transfer to the unburned zone $\dot{Q}_t$ takes a leading role while $\dot{Q}_m$ reduces quickly. This is reasonable since large amount of chemical energy released during combustion is transferred to the unburned zone, which is one of the main reasons for the rapid increment of unburned zone temperature.

The simulation results for the heat loss are shown in Figure 2.16, where the red-line is for the heat loss from the reaction zone to the cylinder head and liner ($\dot{Q}_{w1}$), the blue-line is for the heat loss from the unburned zone to the rest surface area of the cylinder boundary ($\dot{Q}_{w2}$), and the

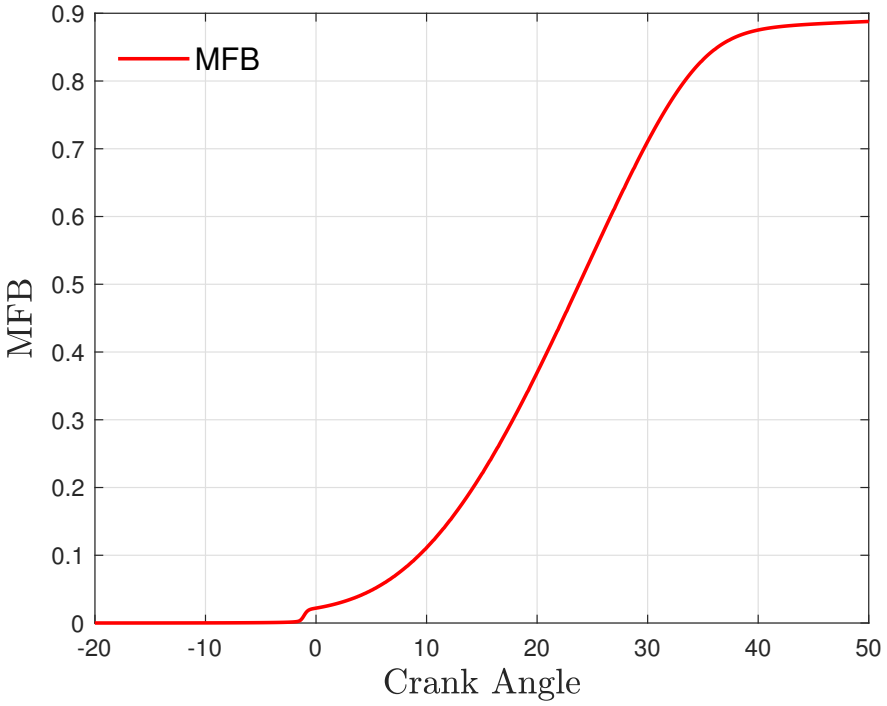

Figure 2.14: Predicted MFB rate at 2000rpm with 6.83bar IMEP (case 4)

purple-line is for the total heat loss from the combustion chamber to the cylinder liner.

$\dot{Q}_{w1}$ is almost zero before the ignition because the reaction zone volume is almost zero compared with that of the unburned zone. After the start of combustion, the released chemical energy increases the reaction zone temperature quickly and the reaction zone expands along with the flame propagation, resulting in the rapid increment of heat loss from the reaction zone to the cylinder boundary. Physically, the heat transfer area from the reaction (burned) zone to the cylinder boundary, after the reaction (burned) zone gets large enough, is the cylinder head surface plus cylinder liner area; see the left drawing of Figure 2.1. However, in this paper, the combustion chamber is assumed to have a hemisphere shape as shown in the right drawing of Figure 2.1, and it is also assumed that the heat transfer from the burned zone to the wall is the base (top) area of the burned zone. With these two assumptions, the base area is not limited by the area of cylinder head. When the calculated area is larger than the cylinder head area, the extra area is considered as the cylinder wall area.

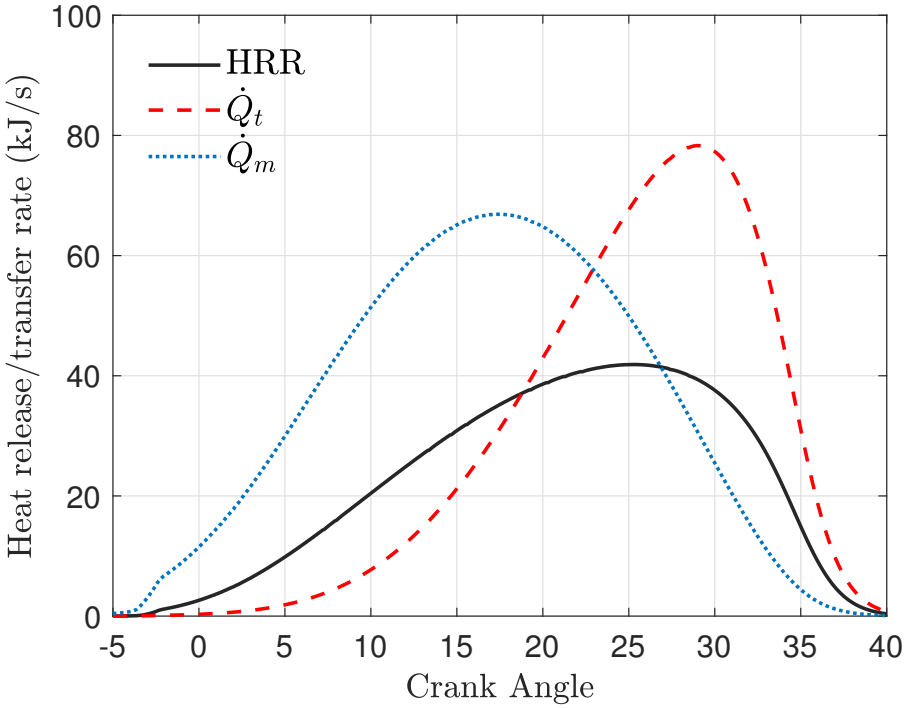

Figure 2.15: Heat release rate and heat transfer rates between two zones at 1500rpm with 6.78bar IMEP (case 3)

The heat loss from the unburned zone to the cylinder boundary $\dot{Q}_{w2}$, comparing with $\dot{Q}_{w1}$, has an obvious delay and increases quickly during the late combustion phase and the expansion phase due to the high temperature of unburned zone mixture. Since the unburned zone becomes a very thin layer by the end of combustion, the heat loss from the unburned zone to the wall is quite small, comparing with the heat loss from reaction zone to the wall. Note that the total heat loss in Figure 2.16 matches these in literature [66, 67, 68].

The calculated indicated mean effective pressure (IMEP) and crank angle, where 50% of fuel was burned (CA50) of all five cases are compared with experimental data in Figures 2.17 and 2.18.

A summary of model prediction error for the in-cylinder pressure is shown in Table 2.6, where the errors shown cover pressure signals between SOC and EVO. Note that the error between IVC and SOC is not the main focus of this paper.

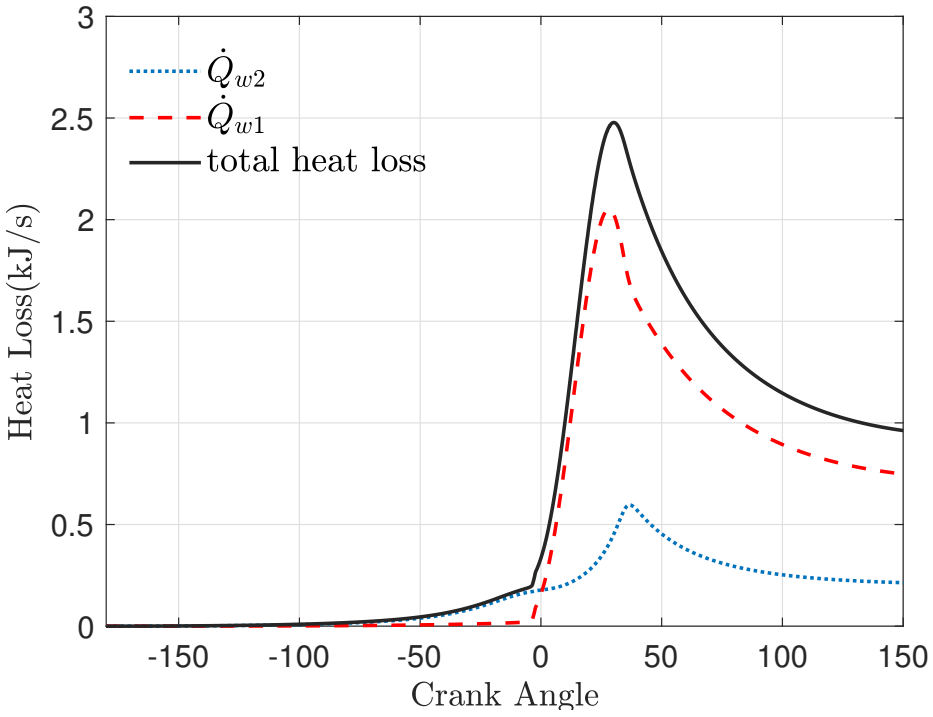

Figure 2.16: Heat losses from reaction and unburned zones to the cylinder boundary at 1500rpm with 6.78bar IMEP (case 3)

Table 2.6: Modeling error of in-cylinder pressure for all five cases between SOC and EVO

Case	Max. relative error	RMSE[bar]
1	6.20%	0.26
2	3.40%	0.24
3	4.09%	0.28
4	5.50 %	0.23
5	5.19%	0.37

2.6 Summary

A control-oriented 0-D reaction-based two-zone thermodynamic model for compression, combustion and expansion phases of spark-ignition engines has been analytically developed, implemented in Matlab/Simulink, calibrated and validated against experimental data in this chapter. The proposed model will be mainly used for predicting thermodynamic characteristics of in-cylinder

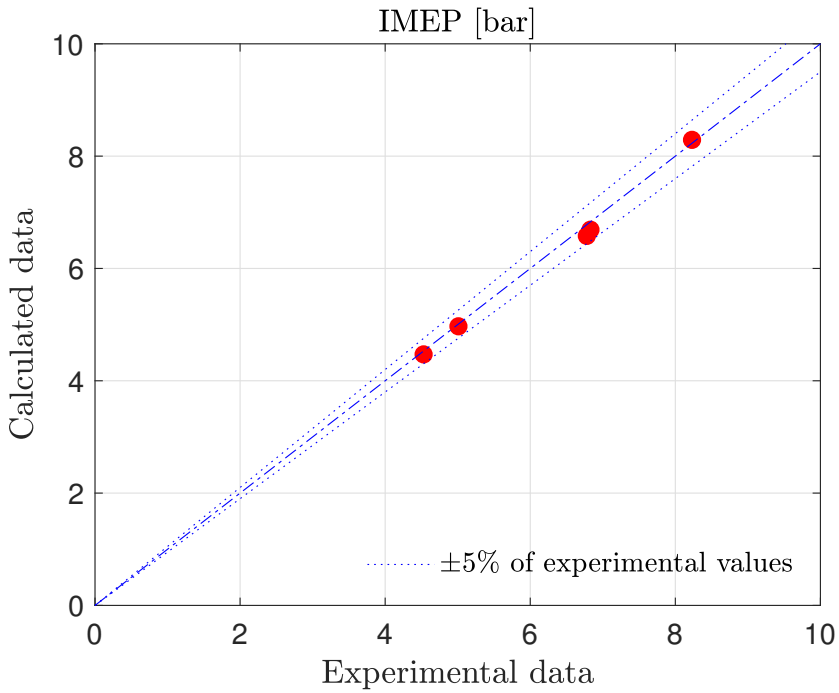

Figure 2.17: Comparison of simulated and experimental IMEPs for all five cases.

mixtures, combustion process, properties of each individual chemical species in both reaction and unburned zones. The experimental validation shows that the proposed two-zone model structure is able to predict the in-cylinder SI combustion process accurately with a simple calibration. Especially, it is able to simulate the in-cylinder thermal stratification characteristics. This confirms that the proposed two-zone model structure with a two-step chemical reaction mechanism can be used for model-based combustion control; and furthermore, the application of two-step chemical reaction mechanism to the proposed model makes it possible to trace individual species state and to predict the mass-fraction-burned, heat release rate, and in-cylinder pressure etc. in real-time. The maximum relative error for the in-cylinder pressure is less than 6.2% under five operational conditions studied with one set of calibration parameters. Therefore, the effect of SI engine control inputs to in-cylinder combustion process can be predicted and can be used for model-based combustion and knock control.

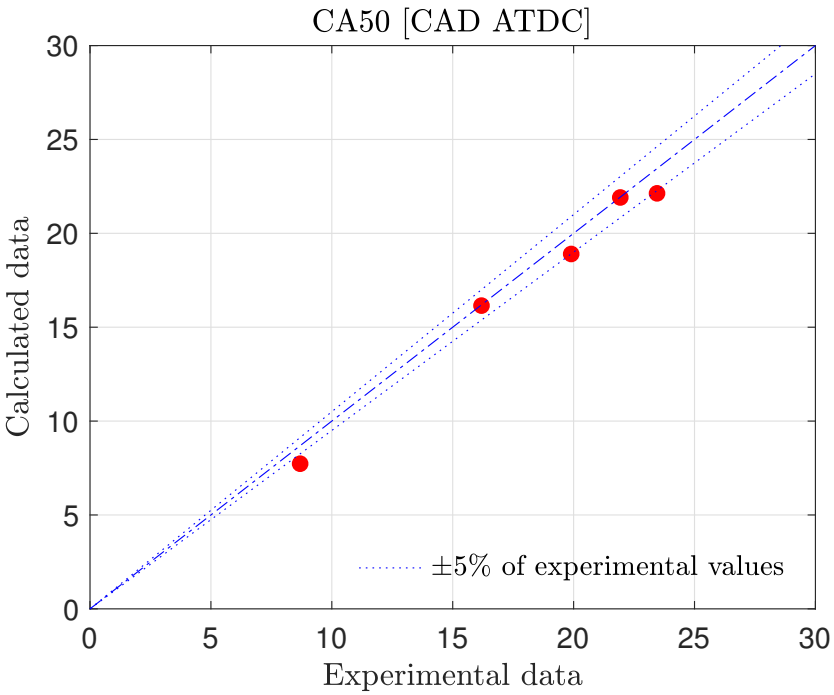

Figure 2.18: Comparison of simulated and experimental CA50 for all five cases.

CHAPTER 3

REAL-TIME PRESSURE WAVE MODELING FOR KNOCK PREDICTION AND CONTROL

The in-cylinder pressure under knocking combustion can be defined as

$$p_{cyl} = \bar{p} + \Delta p \tag{3.1}$$

where p_{cyl} is the in-cylinder pressure; $\bar{p}$ is the average in-cylinder pressure without knock and it can be predicted by the reaction-based 0-D two-zone combustion model developed in Chapter 2; Δp is the pressure wave generated by the shock waves due to knocking combustion and it is zero before the knock onset. A knock pressure wave model will be developed in this chapter to predict Δp. Combined with the combustion model, the in-cylinder pressure under knocking combustion can be predicted and analyzed for the study of knock characteristics; see Figure 3.1.

For the further development of the pressure wave model, the initial conditions at knock onset, such as the in-cylinder pressure, volumes and their rates of the two zones, are required and they can be obtained based on the two-zone reaction-based combustion model. As discussed in Chapter 2, the average in-cylinder pressure without knocking combustion ($\bar{p}$) is obtained based on the ideal gas law shown in (2.35), and volumes and their rates of the two zones can be calculated based on the following two equations.

$$V_u = \frac{m_u R_u T_u}{\bar{p} M W_u}, \dot{V}_u = \frac{dV_u}{dt} \tag{3.2}$$

$$V_r = V_{cyl} - V_u, \dot{V}_r = \dot{V}_{cyl} - \dot{V}_u \tag{3.3}$$

where m_u, T_u, and MW_u are mass, temperature and average molecular weight of the unburned zone mixture, respectively; V_r and V_{cyl} are the volume of the reaction zone and the cylinder, respectively.

The relation between the two-zone reaction-based combustion model and the proposed pressure wave model is shown in Figure 3.2.

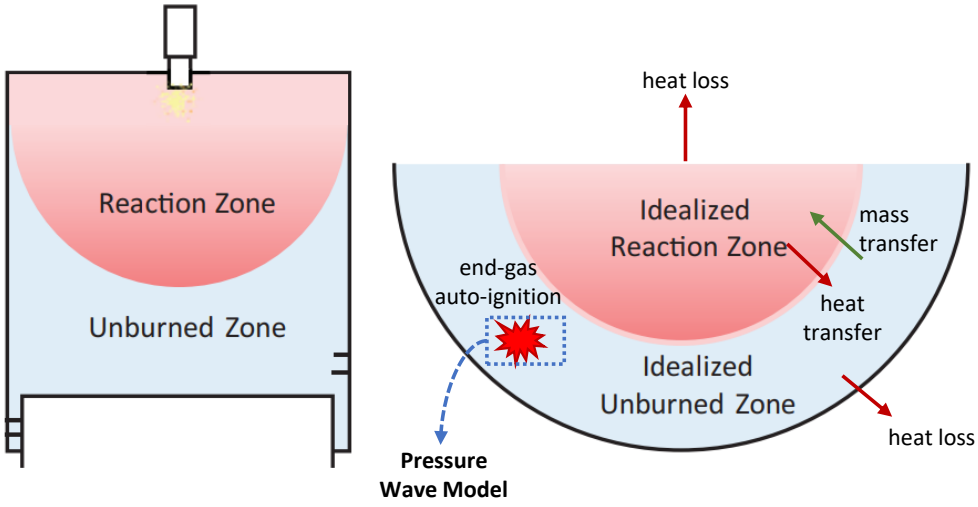

Figure 3.1: 0-D reaction-based two-zone combustion model and the pressure wave model

3.1 Derivation of Pressure Wave Model

The general 3-D wave equation was first applied to the internal combustion engine by Draper [51] to study the in-cylinder pressure oscillations. And the pressure wave is a physical fluid motion that can be described by the pressure wave equation in rectangular coordinates; see (3.4) below.

$$\frac{\partial^2 \Delta p}{\partial x^2} + \frac{\partial^2 \Delta p}{\partial y^2} + \frac{\partial^2 \Delta p}{\partial z^2} = \frac{1}{c^2} \frac{\partial^2 \Delta p}{\partial t^2} \tag{3.4}$$

where Δp is the in-cylinder pressure perturbations; and c is the sound of speed. Assuming that mixture in the unburned zone is ideal and adiabatic gas, the small-amplitude sound speed theory [69] can be applied and c is a constant, leading to the adiabatic sound

$$c = \sqrt{\frac{\gamma \bar{p}_0}{\rho_0}} \tag{3.5}$$

where γ is the heat capacity ratio, assumed to be a constant for the ideal gas. Note that the zero subscript indicates that the pressure and density in (3.5) are taken at the equilibrium conditions.

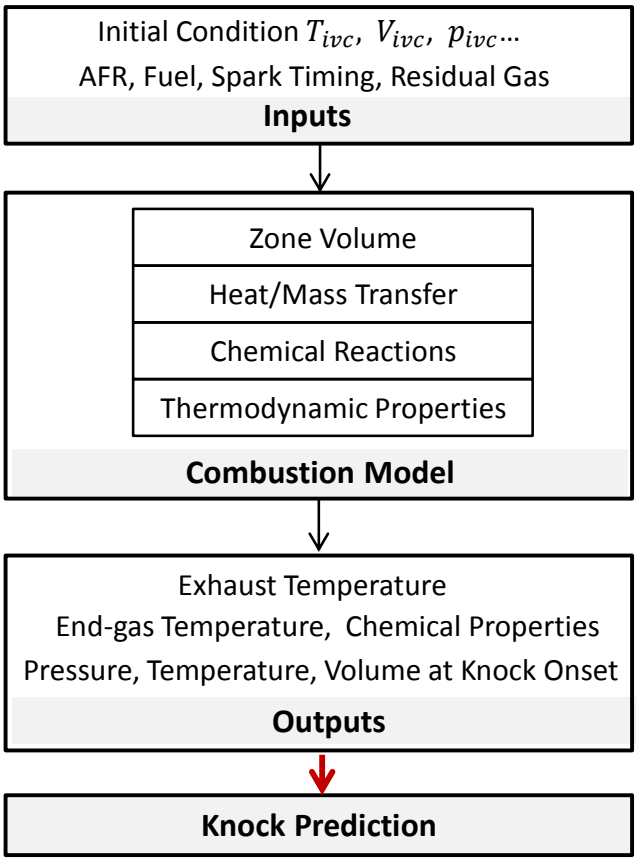

Figure 3.2: Connection between the two-zone reaction-based combustion model and pressure wave model

This 3-D wave equation (3.4) can be written in the cylindrical coordinates to describe the pressure oscillations conveniently; see (3.6) below.

$$\frac{\partial^2 \Delta p}{\partial r^2} + \frac{1}{r}\frac{\partial \Delta p}{\partial r} + \frac{1}{r^2}\frac{\partial^2 \Delta p}{\partial \theta^2} + \frac{\partial^2 \Delta p}{\partial z^2} = \frac{1}{c^2}\frac{\partial^2 \Delta p}{\partial t^2} \tag{3.6}$$

Draper [51] gave a general solution of this pressure wave equation to study the pressure-wave frequencies and vibration modes. But the magnitude decay of the in-cylinder pressure wave, a very important knock property, was not considered. To study the actual pressure waves under knocking combustion, Gaeta ect. [53] proposed a Damped Wave Equation (DWE) by introducing

a time-dependent dissipation term in Draper's wave equation; see (3.7) below.

$$\begin{aligned}&\frac{\partial^2 \Delta p}{\partial r^2}+\frac{1}{r}\frac{\partial \Delta p}{\partial r}+\frac{1}{r^2}\frac{\partial^2 \Delta p}{\partial \theta^2}+\frac{\partial^2 \Delta p}{\partial z^2}\\&=\frac{1}{c^2}\left(\frac{\partial^2 \Delta p}{\partial t^2}+\sigma\frac{\partial \Delta p}{\partial t}\right)\end{aligned} \tag{3.7}$$

where $\sigma\frac{\partial \Delta p}{\partial t}$ is the damping term used to describe the pressure oscillations deadening behavior due to the progressive energy loss of the in-cylinder pressure wave caused by the heat transfer, friction and piston movement. And σ is the damping coefficient to be calibrated.

This chapter focuses on developing a control-oriented real-time knock pressure wave model capable of predicting the main characteristics of engine knock, such as the knock onset timing, intensity, and frequency. A simplified pressure wave equation is proposed, assuming that the pressure wave is uniform in the circumferential and axial directions. The assumption of uniformity in circumferential direction is due to the pre-assumed knock onset location is at 60% of the unburned zone radius. Therefore, the in-cylinder pressure perturbation Δp becomes a function of radius location r and time t. That is $\Delta p = \Delta p(r, t)$; see (3.8) below.

$$\frac{\partial^2 \Delta p}{\partial r^2}+\frac{1}{r}\frac{\partial \Delta p}{\partial r}=\frac{1}{c^2}\left(\frac{\partial^2 \Delta p}{\partial t^2}+\sigma\frac{\partial \Delta p}{\partial t}\right) \tag{3.8}$$

Assuming that t and r in (3.8) are independent, the wave equation can be solved using separating variable method and Fourier series. For the method of separating variables, the solution of wave equation (3.8) can be written in the form below

$$\Delta p(r, t) = R(r)T(t) \tag{3.9}$$

That is a product of two functions, $R(r)$ and $T(t)$, and each depending on only one of the two variables r and t. Differentiating equation (3.8) yields the following two ordinary differential equations (ODEs)

$$T'' + \sigma T' + \lambda^2 T = 0 \tag{3.10}$$

and

$$R'' + \frac{1}{r}R' + \frac{\lambda^2}{c^2}R = 0 \tag{3.11}$$

where $-\lambda^2$ is the separation constant. Solving (3.10) and (3.11) leads to the general solutions of $T(t)$ and $R(r)$ below.

$$T(t) = e^{-\frac{\sigma}{2}t}\left[A\cos\omega t + B\sin\omega t\right] \tag{3.12}$$

where A and B are constants determined by the initial and boundary conditions; ω is the vibration frequency:

$$\omega = \lambda\sqrt{1-(\frac{\sigma}{2\lambda})^2} \tag{3.13}$$

Equation (3.11) can be reduced to Bessel's equation by setting $k = \lambda/c$ and $s = kr$. Then, the derivative of R can be obtained by the chain rule

$$R' = k\frac{dR}{ds} \quad and \quad R'' = k^2\frac{d^2R}{ds^2} \tag{3.14}$$

Substituting (3.14) into (3.11) yields the following Bessel's equation with order $\nu = 0$ below.

$$\frac{d^2R}{ds^2} + \frac{1}{s}\frac{dR}{ds} + R = 0 \tag{3.15}$$

Solutions of equation (3.15) are the Bessel function J_0 and Y_0 of the first and second kind. But Y_0 becomes infinite at 0 and cannot be kept. Therefore, the solution of (3.15) is $R(r) = J_0(s) = J_0(kr)$, where J_0 is the Bessel function of the first kind with order of 0, which will be discussed in detail in the next section.

3.2 Boundary and Initial Conditions

Engine knock is the auto-ignition of unburned mixture in the combustion chamber, so the initial conditions for the knock event can be grouped into two parts: before and at knock onset the pressure wave magnitude is zero and at the moment right after knock onset the pressure wave rate is non-zero in the unburned mixture and zero in the burned mixture; see (3.16) and (3.17).

$$\Delta p(r, t=0) = 0, \quad r \in [0, R_c] \tag{3.16}$$

and

$$\left.\frac{\partial \Delta p}{\partial t}\right|_{r,t=0} = \begin{cases} 0 & \text{in the reaction zone} \\ f(r) & \text{in the unburned zone} \end{cases} \tag{3.17}$$

where R_c is the radius of the engine cylinder; and $f(r)$ is the pressure wave rate at knock onset.

For the boundary conditions, it is assumed that the cylinder wall is a rigid body, so the pressure oscillation rate at the wall is zero; see (3.18).

$$\frac{\partial \Delta p}{\partial r}\Big|_{r=R_c,t} = 0 \quad \text{for all} \quad t \geq 0 \tag{3.18}$$

3.2.1 Bessel's Equation

The solution J_0 to Bessel's equation (3.15) has infinite number of roots denoted by $\alpha_{0,m}(m = 1, 2, ...)$, and its derivative $\dot{J}_0$ also has infinite number of roots denoted by $\beta_{0,m}(m = 1, 2, ...)$. The roots of Bessel functions and their derivatives for orders 0 and 1 are shown in Table 3.1. It indicates that the roots are not regularly spaced on the axis. Note that m is the corresponding vibration normal mode and the roots in the third and fourth columns will be used in this paper.

Table 3.1: Roots of Bessel functions and the derivative for order $\nu = 0$ and 1 [1]

m	$J_0(\alpha_{0,m})$	$J_1(\alpha_{1,m})$	$\dot{J}_0(\beta_{0,m})$	$\dot{J}_1(\beta_{1,m})$
1	2.4048	3.8317	3.8317	1.8412
2	5.5201	7.0156	7.0156	5.3314
3	8.6537	10.1735	10.1735	8.5363
4	11.7915	13.3237	13.3237	11.7060
5	14.9309	16.4706	16.4706	14.8636

To satisfy the boundary condition (3.18), the pressure wave equation (3.9) can be derived as

$$\frac{\partial \Delta p}{\partial r}\Big|_{r=R_c,t} = T(t)\dot{J}_0(kr)\Big|_{r=R_c} = 0. \tag{3.19}$$

The time function $T(t)$ is non-zero, and therefore, the derivative of Bessel function is

$$\dot{J}_0(kR_c) = 0 \tag{3.20}$$

Since the derivative $\dot{J}_0$ of Bessel function with order $\nu = 0$ has infinite number of positive roots (Table 3.1), the boundary condition for (3.17) can be satisfied and (3.20) leads to

$$kR_c = \beta_{0,m} \quad \text{thus} \quad k = k_m = \frac{\beta_{0,m}}{R_c}, \quad m = 1, 2, ... \tag{3.21}$$

where roots ($\beta_{0,m}$) are given in Table 3.1.

Therefore, the solution of ODE (3.11) satisfying the boundary condition (3.18) is

$$R(r) = J_0(k_m r) = J_0\left(\frac{\beta_{0,m}}{R_c} r\right), \quad m = 1, 2, \ldots \tag{3.22}$$

Note that although the knock onset location is assumed at 60% of unburned zone radius, the solution $R(r)$ varies as a function based on radius r due to the expansion of the reaction zone during combustion.

3.2.2 Time Function

By satisfying the first initial condition (3.16), the time function $T(t)$ provide initial condition $T(t = 0) = A = 0$. Thus, the general solution of the time function $T(t)$ is

$$T(t) = Be^{-\frac{\sigma}{2}t} \sin \omega t \tag{3.23}$$

where B is a constant and $B \neq 0$; σ is the damping coefficient to be calibrated; and the wave frequency is $\omega/(2\pi)$ Hz, where ω is computed by

$$\omega = \omega_m = \lambda_m \sqrt{1 - \left(\frac{\sigma}{2\lambda_m}\right)^2}, \quad \lambda_m = k_m c \tag{3.24}$$

Note that the adiabatic sound speed c, which is a constant, can be further derived based on the small-amplitude of sound speed theory and ideal gas law

$$c = \sqrt{\frac{\gamma \bar{p}_0}{\rho_0}} = \sqrt{\gamma \frac{R_u}{MW_u} \bar{T}} \tag{3.25}$$

where R_u is the universal gas constant; MW_u is the average molar weight of unburned zone mixtures; and $\bar{T}$ is the average temperature of end-gas at the equilibrium condition. The sound of speed is used for calculating the pressure wave frequency. It is found experimentally that the influence of temperature $\bar{T}$ to the knock frequency is small enough and can be neglected, comparing with the effect of engine geometry. Furthermore, the knocking combustion occurs rapidly and the temperature change can also be neglected. Therefore, $\bar{T}$ is assumed to be constant (constant sound of speed) and becomes a calibration parameter based on the experimental knock frequency.

The damping coefficient σ is a bounded constant. Since parameter ω in (3.24) is defined as a positive real number, the following root solution should be positive

$$1 - \left(\frac{\sigma}{2\lambda_m}\right)^2 > 0 \tag{3.26}$$

and therefore,

$$0 < \sigma < 2\lambda_m = 2k_m c = \frac{2c}{R_c}\beta_{0,m} < \frac{2c}{R_c}\min\left[\beta_{0,m}\right] \tag{3.27}$$

Based on the characteristics of Bessel function ($\min\left[\beta_{0,m}\right] = \beta_{0,1} = 3.8317$), damping coefficient σ is up-bounded by $\sigma < 2c\beta_{0,1}/R_c$. Then, the corresponding general solution of ODE (3.10) is

$$T_m(t) = B_m e^{-\frac{\sigma}{2}t} \sin \omega_m t \tag{3.28}$$

Hence, the general solution of the pressure wave equation (3.8) satisfying the boundary condition (3.18) and the first initial condition (3.16) is

$$\begin{aligned} \Delta p(r,t) &= \sum_{m=1}^{\infty} R_m(r) T_m(t) \\ &= \sum_{m=1}^{\infty} B_m e^{-\frac{\sigma}{2}t} \sin(\omega_m t) J_0\left(\frac{\beta_{0,m}}{R_c} r\right) \end{aligned} \tag{3.29}$$

3.2.3 Coefficient B_m

Knock is an auto-ignition of the unburned end-gas in the combustion chamber, so the pressure wave equation for knock prediction is for the unburned zone. Therefore, the first initial condition in (3.17) regarding pressure waves in the reaction zone is ignored. As a result, coefficient B_m can be determined by using the second initial condition in (3.17). Differentiating (3.29) with respect to t and using initial condition (3.17) lead to

$$\left.\frac{\partial \Delta p}{\partial t}\right|_{r,t=0} = \sum_{m=1}^{\infty} B_m \omega_m J_0\left(\frac{\beta_{0,m}}{R_c} r\right) = f(r) \tag{3.30}$$

This is the Fourier-Bessel series representing $f(r)$ in terms of $J_0(\beta_m r/R_c)$. And the corresponding coefficients B_m can be determined as

$$B_m = \frac{2}{\omega_m {R_c}^2 {J_1}^2(\beta_{0,m})} \int_0^{R_c} r f(r) J_0\left(\frac{\beta_{0,m}}{R_c} r\right) dr \tag{3.31}$$

where $J_1(\beta_m)$ is the Bessel function of the first kind with order $\nu = 1$. Since the square of norm of the Bessel function J_0 is

$$\begin{aligned}\left\| J_0\left(\frac{\beta_{0,m}}{R_c}r\right)\right\|^2 &= \int_0^{R_c} r J_0^2\left(\frac{\beta_{0,m}}{R_c}r\right) dr \\ &= \frac{{R_c}^2}{2} {J_1}^2\left(\beta_{0,m}\right)\end{aligned} \tag{3.32}$$

Therefore, term $J_1^2(\beta_{0,m})$ can be obtained by

$$J_1^2(\beta_{0,m}) = \frac{2}{{R_c}^2}\int_0^{R_c} r J_0^2\left(\frac{\beta_{0,m}}{R_c}r\right) dr \tag{3.33}$$

Then, substituting equation (3.33) into (3.31), the coefficient B_m can be written as

$$B_m = \frac{\displaystyle\int_0^{R_c} r f(r) J_0\left(\frac{\beta_{0,m}}{R_c}r\right) dr}{\omega_m \displaystyle\int_0^{R_c} r J_0^2\left(\frac{\beta_{0,m}}{R_c}r\right) dr} \tag{3.34}$$

where r is in the interval of $[0, R_c]$.

3.2.4 Pressure Rate at Knock Onset

The mass conservation equation for the in-cylinder flow field can be written as

$$\frac{\partial \Delta p}{\partial t} + c^2 \nabla \cdot (\rho \boldsymbol{u}) = 0 \tag{3.35}$$

where ρ is the mass density; $\boldsymbol{u}$ is the velocity vector; and Δp is the in-cylinder pressure perturbations under knock combustion. Using this equation for the unburned zone where knock occurs and calculating the integral over the total unburned zone volume yield,

$$\int_{V_u} \frac{\partial \Delta p}{\partial t} dV_u + \int_{V_u} c^2 \nabla \cdot (\rho \boldsymbol{u}) dV_u = 0 \tag{3.36}$$

and it can be further simplified to

$$\frac{\partial \Delta p}{\partial t} = \frac{-c^2 \rho \dot{V}_u}{V_u} \tag{3.37}$$

Combining equations (3.25) and (3.37), the in-cylinder pressure rate at knock onset, denoted by $f(r)$, can be found; see below.

$$\left.\frac{\partial \Delta p}{\partial t}\right|_{r,t=0} = f(r) = \gamma \bar{p}_0 \frac{1}{V_{u,0}} \frac{\mathrm{d}V_{r,0}}{\mathrm{d}t} \tag{3.38}$$

where γ is the heat capacity ratio; $\bar{p}_0$ is the average in-cylinder pressure at knock onset; $V_{u,0}$ and $V_{r,0}$ are the volume of the unburned and reaction zone at knock onset, respectively. All these variables can be obtained by the two-zone combustion model developed in Chapter 2.

3.3 Solution of Pressure Wave Equation for Knock Prediction

Based on these results from the previous section, the general solution of the pressure wave equation satisfying the boundary and initial conditions is in a series form; see (3.29), and each term in the equation can be calculated, where m is the vibration mode of the in-cylinder pressure wave. Therefore, equation (3.29) is a general solution covering all vibration modes from $m = 1$ to ∞. The details for different vibration modes can be found in reference [70].

In this dissertation, the first vibration mode ($m = 1$) is used for modeling the knock pressure wave, and the associated solution is

$$\Delta p(r,t) = B_1 e^{-\frac{\sigma}{2}t} \sin(\omega_1 t) J_0\left(\frac{\beta_{0,1}}{R_c} r\right) \tag{3.39}$$

where coefficient B_1 is

$$B_1 = \frac{\gamma \bar{p}_0 \dot{V}_{r,0} \int_0^{R_c} r J_0\left(\frac{\beta_{0,1}}{R_c} r\right) dr}{\omega_1 V_{u,0} \int_0^{R_c} r J_0^2\left(\frac{\beta_{0,1}}{R_c} r\right) dr} \tag{3.40}$$

Note that $\dot{V}_{r,0} = dV_{r,0}/dt$; β_1 is the first (minimum) root of the derivative of Bessel function J_0; and ω_1 is the damped frequency. Combining equations (3.21) and (3.24), ω_1 can be found; see below.

$$\omega_1 = \sqrt{\frac{{\beta_{0,1}}^2 c^2}{{R_c}^2} - \frac{\sigma}{4}} \tag{3.41}$$

Therefore, the in-cylinder pressure p_{cyl} can be obtained, based on equation (3.1). It can be further analyzed to predict the knock characteristics, such as the knock onset timing, frequency, intensity and even the cycle-to-cycle variability.

3.4 Evaluation Methods of Knock Phenomenon

3.4.1 Knock Onset

The Livengood-Wu correlation [36] was widely used as an empirical method to predict the knock timing of spark-ignition engines. And based on the proposed reaction-based combustion model, a chemical kinetic-based method based on the Arrhenius integral (ARI) is developed from Livengood-Wu correlation and used in this paper to predict the start of combustion (SOC) in the unburned zone, where ARI is defined below.

$$\mathrm{ARI} = \int_{\theta_{IVC}}^{\theta_i} A_{knk} {p_{cyl}}^{a_{knk}} [\mathrm{C_8H_{18}}]^{b_{knk}} [\mathrm{O_2}]^{c_{knk}} e^{-\frac{T_{a,knk}}{T_u(\theta)}} \mathrm{d}\theta \tag{3.42}$$

where $A_{knk}, a_{knk}, b_{knk}, c_{knk}$ are auto-ignition coefficients to be calibrated based on experimental data under knocking combustion; $[\mathrm{C_8H_{18}}]$ and $[\mathrm{O_2}]$ are the molar concentration of fuel and oxygen, respectively; and T_u is the unburned zone temperature. Note that the molar concentration and zone temperatures are provided by the reaction-based two-zone combustion model developed earlier; $T_{a,knk}$ is the activation temperature defined by

$$T_{a,knk} = \frac{E_{a,knk}}{R_u} \tag{3.43}$$

$E_{a,knk}$ (J/mol) in (3.43) is the activation energy of the chemical reaction in the unburned zone; and R_u is the universal gas constant. Note that $E_{a,knk}$ is a constant to be calibrated.

Equation (3.42) can be interpreted as an integral of chemical reaction rate of the unburned mixture (end-gas); and this equation also indicates that the ARI is positive and the integral is increasing monotonically. The criterion for auto-ignition is at the crank angle when ARI reaches one, that is

$$ARI = 1. \tag{3.44}$$

3.4.2 Knock Intensity

Engine knock properties are generally characterized in terms of knock onset timing, knock intensity and frequency based on in-cylinder pressure waves. In reality, the knock onset timing is the most important factor and is investigated by many literature. The knock intensity and frequency are the other two important factors to describe the knock severity and physical characteristics. There are three widely used measures for knock intensity and they are Maximum Amplitude of Pressure Oscillations (MAPO), Integral of Modulus of Pressure Gradient (IMPG), and Integral of Modulus of Pressure Oscillation (IMPO), where the MAPO method is used in the rest of paper to represent the knock intensity due to its simpleness; see below.

$$\text{MAPO} = \frac{1}{N}\sum_{1}^{N} \max_{\theta_0;\theta_0+\zeta} |\Delta p| \tag{3.45}$$

where Δp is the pressure perturbations; N is the number of pressure wave peaks; θ_0 is the crank angle of knock onset; ζ is the knock window length, and it is defined to be 20 CAD from knock onset. So MAPO can be presented as KI20 as well.

3.5 Model Calibration and Validation

3.5.1 Experiment Setup and Model Calibration

The experimental data used to calibrate and validate the proposed reaction-based 0-D pressure wave model is collected from a 4-cylinder, four-stroke SI engine through dynamo-meter experiments. The engine parameters are listed in Table 2.1.

The test data for two typical steady-state engine operating conditions (high load at 1500rpm and 2000rpm) are used for validation and is summarized in Table 3.2, where the relative air-fuel ratio is controlled to be close to stoichiometric. Note that the ignition timing under these two operational conditions are controlled to be near the engine knock limit, making it possible to validate the pressure wave model.

An A&D CAS (combustion analysis system) is used to record the in-cylinder pressure, intake manifold pressure, ignition coil dwell current, etc. The calibrated parameters are listed in Table

Table 3.2: Engine operating conditions (at knock limit).

Case	1	2
IMEP[bar]	7.5	8.23
Engine Speed[rpm]	1500	2000

3.3. Parameters listed in Table 3.3 can be classified into two groups. The first group consists of $A_{knk}, a_{knk}, b_{knk}, c_{knk}$ and E_{knk}, which are related to the knock onset prediction; and the second group parameters, σ and $\bar{T}$, are related to knock frequency. The first group parameters are calibrated based on the knock onset timing obtained from experimental data, where $a_{knk} \sim E_{a,knk}$ are coefficients corresponding to the chemical reactions of knocking combustion and have low sensitivity to engine geometry and operating conditions, and they are calibrated first. A_{knk} has a high sensitivity and is calibrated by keeping the other four parameters constant. σ is used to describe the pressure wave deadening behavior and it is bounded; see (3.26) and (3.27), and $\bar{T}$ is the average temperature of unburned zone mixture, and was assumed to be constant. Based on (3.25), $\bar{T}$ is used to calculate the sound of speed and then, combining with (3.41), to obtain the knock frequency. As a summary, σ and $\bar{T}$ are calibrated based on the knock frequency obtained from the experiment data. Note that these parameters keep unchanged under different operating conditions, which is one of the major advantages of the proposed pressure wave model and can be conveniently used for the model-based knock control.

Table 3.3: Calibrated parameters.

A_{knk}	a_{knk}	b_{knk}	c_{knk}	$E_{a,knk}$	σ	$\bar{T}$
3e7	0.5e-10	0.25	1.5	1.8691(J/mol)	0.015	2080K

3.5.2 Knock Onset and Intensity Prediction

Generally, the knock pressure wave is dominated by its first and second vibration modes, and the first mode frequency is around 6 kHz and the second mode frequency is around 12.5 kHz. In the

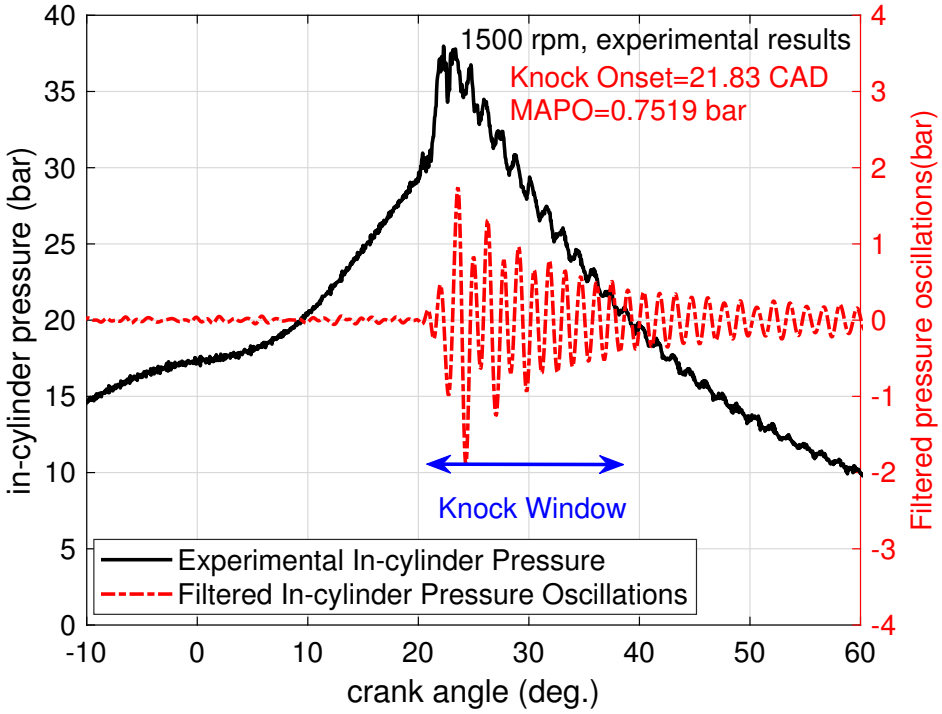

Figure 3.3: Experimental in-cylinder pressure and filtered pressure wave of the first knock cycle at 1500 rpm with IMEP = 7.5 bar (case 1)

simulation study, the first mode frequency is investigated in this paper. It is well-known that the in-cylinder pressure signal contains rich information of key knock characteristics. Figure 3.3 shows the experimental in-cylinder pressure of the first knock cycle and its bandpass-filtered pressure signals at 1500 rpm with IMEP of 7.5 bar. The black solid-line presents the unfiltered in-cylinder pressure signal under knocking combustion and the red dash-dotted line presents the pressure wave obtained using a band-pass filter of 3~10 kHz (first knock mode). The knock window is between knock onset to 20 CAD after knock onset, which is used to calculate MAPO (KI20). As a result, knock onset timing and intensity can be obtained using the in-cylinder pressure signal, and the knock frequency can be found by processing the filtered pressure wave using fast Fourier transform (FFT), which will be discussed later. The model's ability of predicting the knock onset timing, knock intensity and frequency will be discussed in next two subsections by analyzing the simulated in-cylinder pressures.

The second part for model validation is regarding the knock cycle-to-cycle variability, which is kind of random but could be related to the mixture properties at intake valve close (IVC). For a fixed engine operating condition, the knock intensity could change cycle-by-cycle and vary from low to high. Although it is difficult to predict the random knock intensity variation accurately, the correlation between knock intensity and the in-cylinder mixture properties at IVC will be studied using the simulated pressure signal from the proposed model in the third subsection.

In this subsection, the capability of estimating knock onset and intensity is demonstrated under two engine operating conditions: case 1 (1500 rpm, 7.5 bar, Figure 3.3) and case 2 (2000 rpm, 8.2 bar, Figure 3.6), where the first knock cycle pressure signals for both cases are used. The main reason to use the first knock cycle data is that the in-cylinder mixture properties at IVC are relatively consistent for the first knock cycle and after knock occurs the properties at IVC are influenced by the previous knock cycle.

To validate the proposed model, first, the experimental in-cylinder pressure of case 1 is processed using a band-pass filter of 3∼10 kHz, where the first knock cycle data is shown in Figure 3.3. The black solid-line is the recorded in-cylinder pressure of the first knock cycle, and the red dash-dotted line is the pressure wave obtained using a band-pass filter. Figure 3.3 shows that the knock onset timing is 21.83 CAD ATDC and the knock intensity MAPO calculated based on the filtered pressure wave within the knock window is 0.7519 bar.

For predicting knock onset timing based on the developed model, Equations (3.42) and (3.44) are used to simulate the unburned zone Arrhenius integral (ARI) and the associated rate for case 1; see Figure 3.4. Note that the upper plot in Figure 3.4 is the Arrhenius integral rate in the unburned zone and the lower one is the corresponding ARI. The rate of ARI is a measure representing the knock severity. For instance, a steep increment of ARI rate indicates a heavy knock cycle. Based on early discussion, ARI is positive and monotonically increasing (see Equation (3.42)). The calculated ARI confirms it and increases from 0 and reaches 1 (marked with a red dot) at 21.3 CAD ATDC, indicating knock onset timing of 21.3 CAD ATDC. Note that the experimental data shows a knock onset timing of 21.83 CAD ATDC, and therefore, the predicting error is about 2.43%.

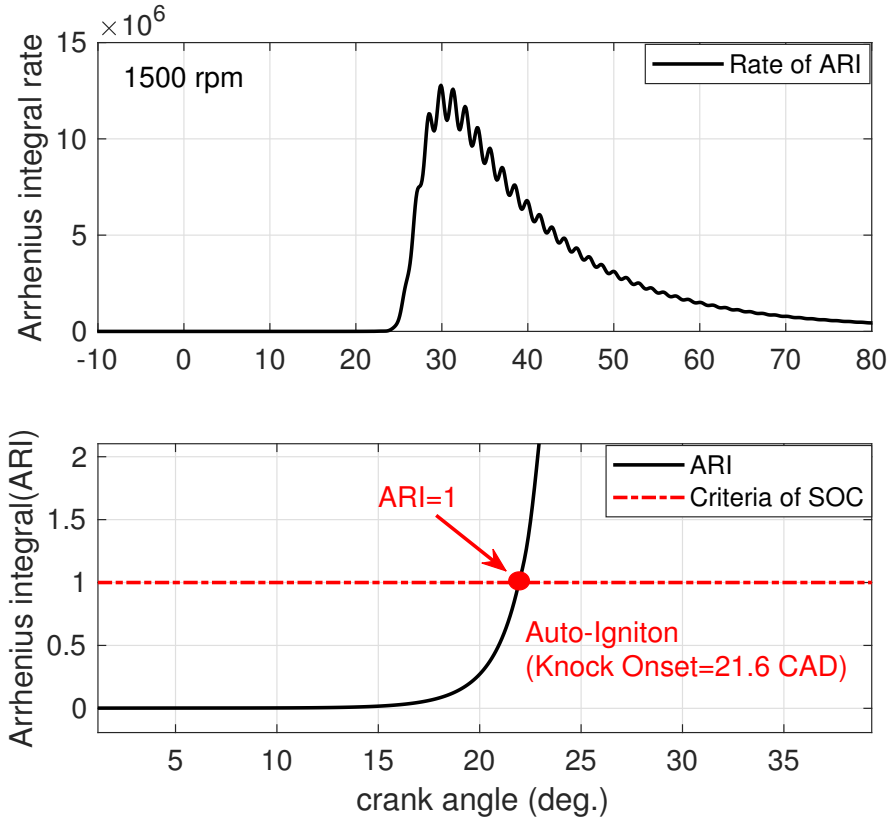

Figure 3.4: Simulated ARI and its rate in the unburned zone of the first knock cycle at 1500 rpm with IMEP = 7.5 bar (case 1)

The initial conditions at knock onset, such as the in-cylinder pressure and its rate, the unburned zone volume and the volume rate of the reaction zone, are required to model the knock pressure waves. With the predicted knock onset timing, the initial conditions can be obtained via the two-zone reaction-based combustion model developed earlier; see Table 3.4.

Table 3.4: Initial conditions at knock onset for the first knocking cycle of cases 1 and 2.

	$\bar{p}_0$[bar]	V_u[m^3]	$\dot{V}_r$[m^3/s]	$\left.\frac{\partial p}{\partial t}\right\|_{r,t=0}$[bar/s]
case 1	34.45	1.186e-5	0.03796	1.1696e5
case 2	32.16	1.382e-5	0.03614	1.1791e5

The simulated in-cylinder pressure and pressure wave are shown in Figure 3.5, where the

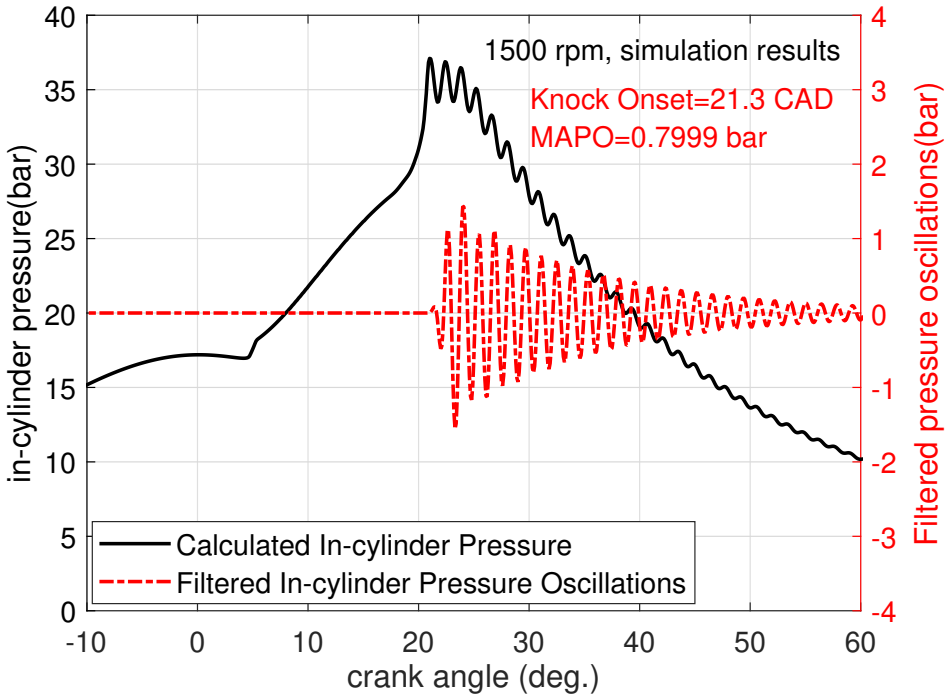

Figure 3.5: Calculated in-cylinder pressure wave at 1500 rpm with IMEP = 7.5 bar (case 1)

predicted in-cylinder pressure is filtered with a 3~10 kHz band-pass filter (same one used for processing the experimental data). Next, the knock intensity is calculated and it is 0.7999 bar with a predicting error of 6.38% over the experimental data shown in Figure 3.3.

Similarly, the proposed model is simulated at 2000 rpm using the boundary conditions shown in Table 3.4. Case 2 experimental in-cylinder pressure of the first knock cycle is filtered using the same band-pass filter and the results are shown in Figure 3.6, indicating a knock onset timing of 24 CAD ATDC and the MAPO of 1.173 bar.

For predicting the knock onset timing under this operating condition, the simulated ARI and its rate in the unburned zone are shown in Figure 3.7. The ARI increases from 0 and reaches 1 at 23.6 CAD ATDC, indicating the knock onset timing of 23.6 CAD ATDC. Comparing with the experimental onset timing of 24 CAD ATDC (see Figure 3.6), the predicting error is only 1.67%.

The simulated in-cylinder pressure and pressure wave obtained using the same band-pass filter are shown in Figure 3.8. The calculated MAPO is 1.1969 bar with a predicting error of 2.037%,

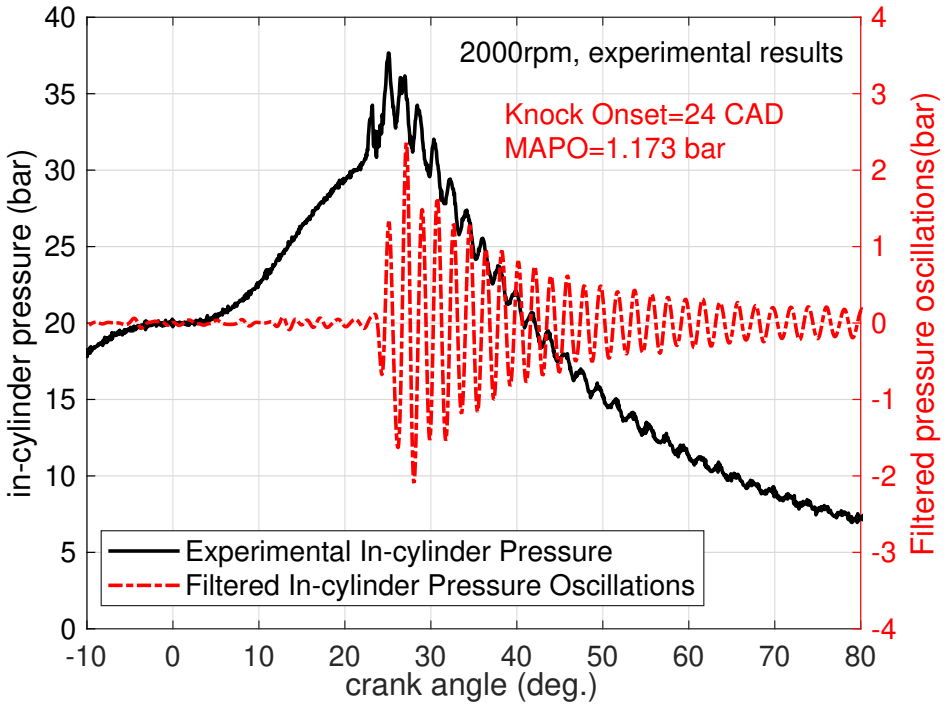

Figure 3.6: Experimental in-cylinder pressure and filtered pressure wave of a typical knock cycle at 2000rpm with IMEP = 8.23 bar (case 2)

comparing with the experimental data in Figure 3.6.

As a summary, the model's capability of predicting the knock onset timing and intensity under two different engine operating conditions are demonstrated by comparing with the experiment results. The maximum predicting error for knock intensity is 6.38% (case 1) and maximum prediction error for knock onset timing is 2.43% (case 1).

3.5.3 FFT Analysis of In-Cylinder Pressure Waves

The knock pressure wave frequency is mainly determined by engine geometry and remains unchanged throughout the combustion process under different operating conditions. In general, the fast Fourier transform (FFT) is a well-known method for analyzing the knock signal in frequency domain. To find the knock frequency, FFT is used to analyze both experimental and simulated in-cylinder pressure waves for cases 1 and 2. The FFT results of experimental simulated data of

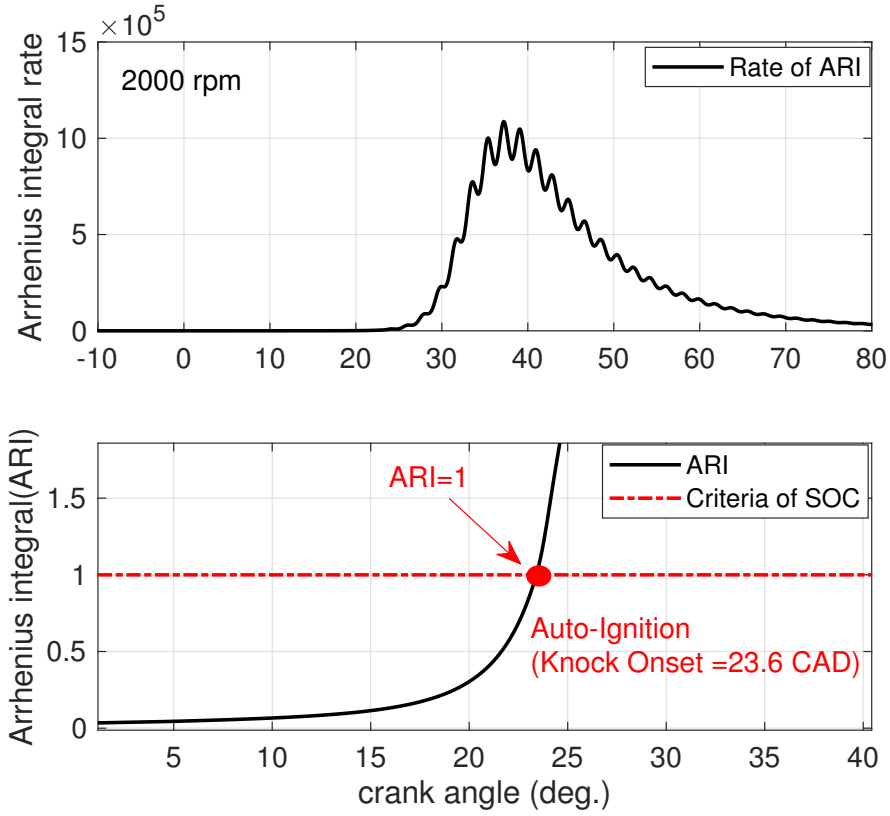

Figure 3.7: Simulated ARI and its rate in the unburned zone for the first knocking cycle at 2000 rpm with IMEP = 8.23 bar (case 2)

cases 1 and 2 are shown in Figures 3.9 and 3.10. These two figures indicate that the experimental knock frequency is 6.303 kHz and remains unchanged under different engine operating conditions while the predicted knock frequency for both cases (see Figures 3.9 and 3.10) are 6.310 kHz. Note that the magnitude of the pressure waves in two figures are different due to the difference in knock intensity.

These results match with the experimental ones, and the predicting error of knock frequency is less than 0.2%, indicating that the proposed model is able to predict knock frequency accurately.

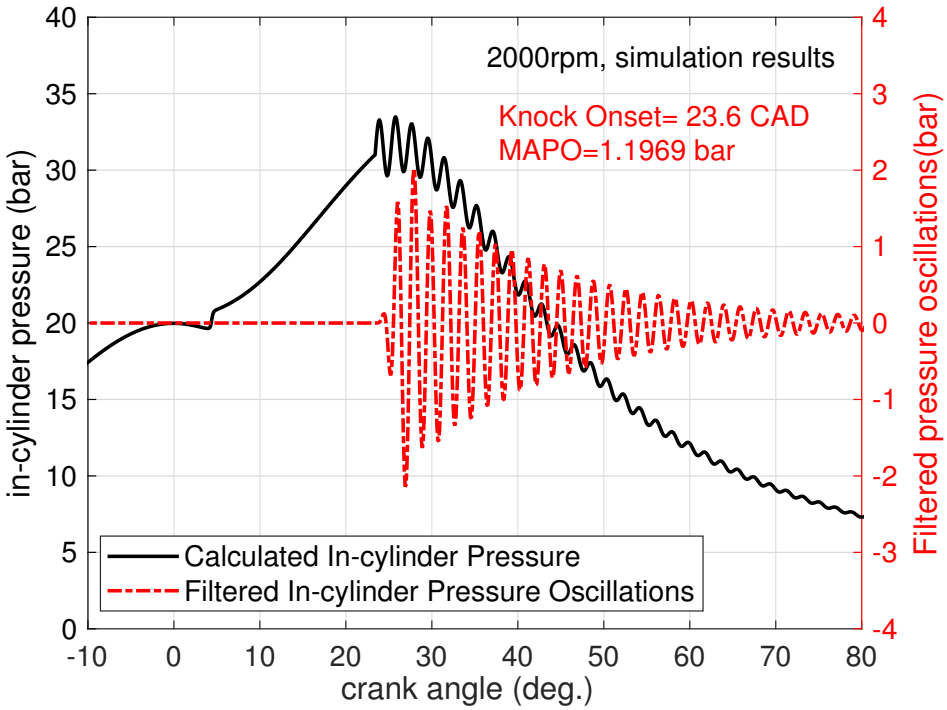

Figure 3.8: Simulated in-cylinder pressure and pressure wave with a 3~10 kHz band-pass filter at 2000 rpm with IMEP = 8.23 bar (case 2)

3.5.4 Knock Cycle-to-Cycle Variability

The engine knock phenomenon shows cycle-to-cycle variability even under a steady-state engine operating condition. Figure 3.11 shows the experimental in-cylinder pressures for 6 consecutive engine cycles under knocking combustion when the engine is operated at 1500 rpm with IMEP of 7.5 bar (case 1 in Table 2.2). It is clear that the knock intensity changes cycle-by-cycle, where cycle #1 has light knock, cycle #2 heavy knock, cycles #3 to #5 medium knock, and cycle #6 normal combustion (without knock - baseline cycle), where the baseline cycle pressure has a small rate of rise after the ignition and the peak pressure is around 27 bar. Comparing with the baseline cycle, the knock cycles shows faster pressure rate of rise and the heavy knock cycle has the most steep rate of rise. The difference of peak in-cylinder pressure between heavy knock and based-line cycles can be up to 17 bar.

The experimental in-cylinder pressures under 2000 rpm with 8.23 bar IMEP (case 2) are

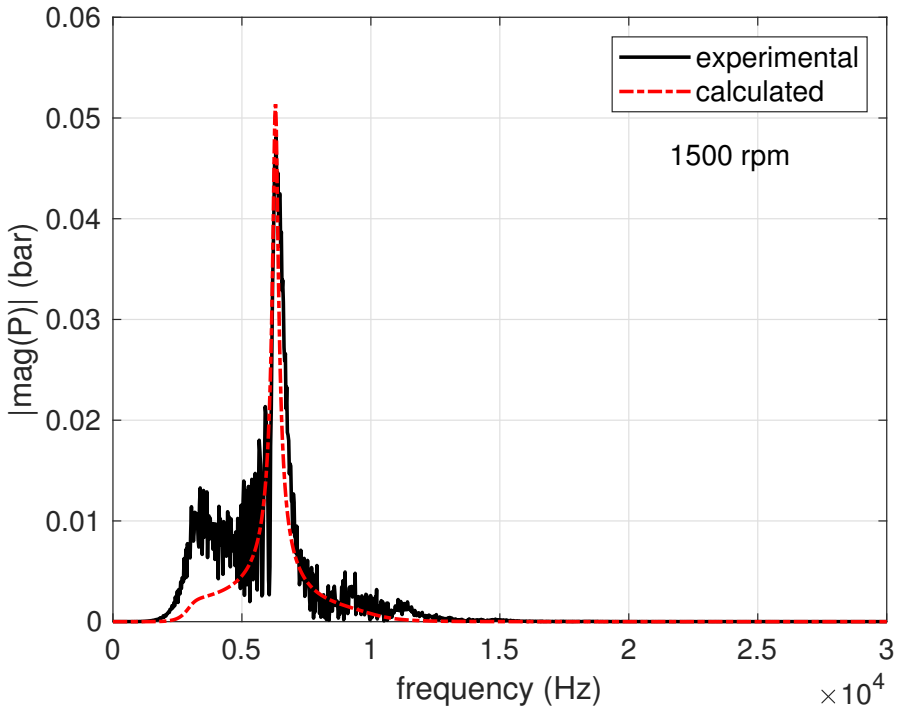

Figure 3.9: FFT analysis of the experimental in-cylinder pressure wave at 1500rpm, IMEP=7.5 bar (case 1)

analyzed as well. As shown in Figure 3.12, 20 consecutive engine cycles under knocking combustion condition are bandpass-filtered and the corresponding MAPOs are calculated. The knock intensity plot shown in Figure 3.12 indicates cycle-to-cycle variability. Although it is kind of random but with a repeatable pattern, where a high knock intensity cycle is always followed by a low knock intensity one for most of the cases. Note that MAPO pattern repeats but its value is different, indicating that the knock servility varies, and the MAPO can drop down to zero (no knock), after repeating the pattern a few times; see cycles #14 and #19. Furthermore, the mean value and standard deviation of knock intensity for these 20 consecutive engine cycles are 1.0009 bar and 0.5713 bar, respectively.

The cycle-to-cycle variability of knock phenomenon may be related to the in-cylinder mixtures properties at IVC, which is influenced by the last combustion cycle. Therefore, the correlation between cycle-to-cycle knock variability and mixture properties at IVC will be studied in this

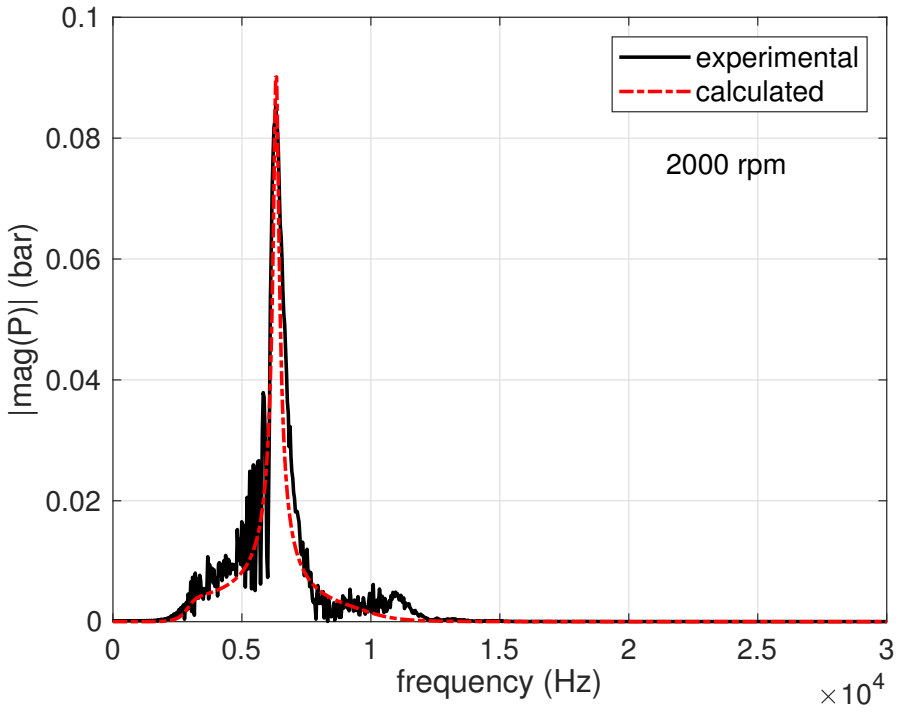

Figure 3.10: FFT analysis of the experimental in-cylinder pressure wave at 2000rpm, IMEP=8.23 bar (case 2)

section using the calibrated pressure wave model.

In this study, the external EGR valve was closed for engine tests and hence there is no external EGR. As a result, the mixture at IVC consists of the pre-mixed fresh air, fuel, and the trapped residual gas from the last cycle. Based on our study, the mixtures properties, especially the mixture temperature at IVC (T_{IVC}), has significant influence to the combustion characteristics, heat transfer and gas temperature at exhaust valve open (EVO). For a knock cycle, the knocking combustion in the unburned zone leads to high pressure rate of rise and rapid heat loss to the wall. As a result, the net heat transfer rate in the unburned zone $\dot{Q}_u$ will be smaller than the normal combustion cycle. Based on Equation (2.33), the unburned zone temperature at EVO (T_{EVO}) will decrease, too. Therefore, the mixture temperature at IVC for the following cycle will decrease due to the reduced temperature of the trapped residual gas, which further affects the next combustion cycle. This could be one of the reasons for the cycle-to-cycle knock variability.

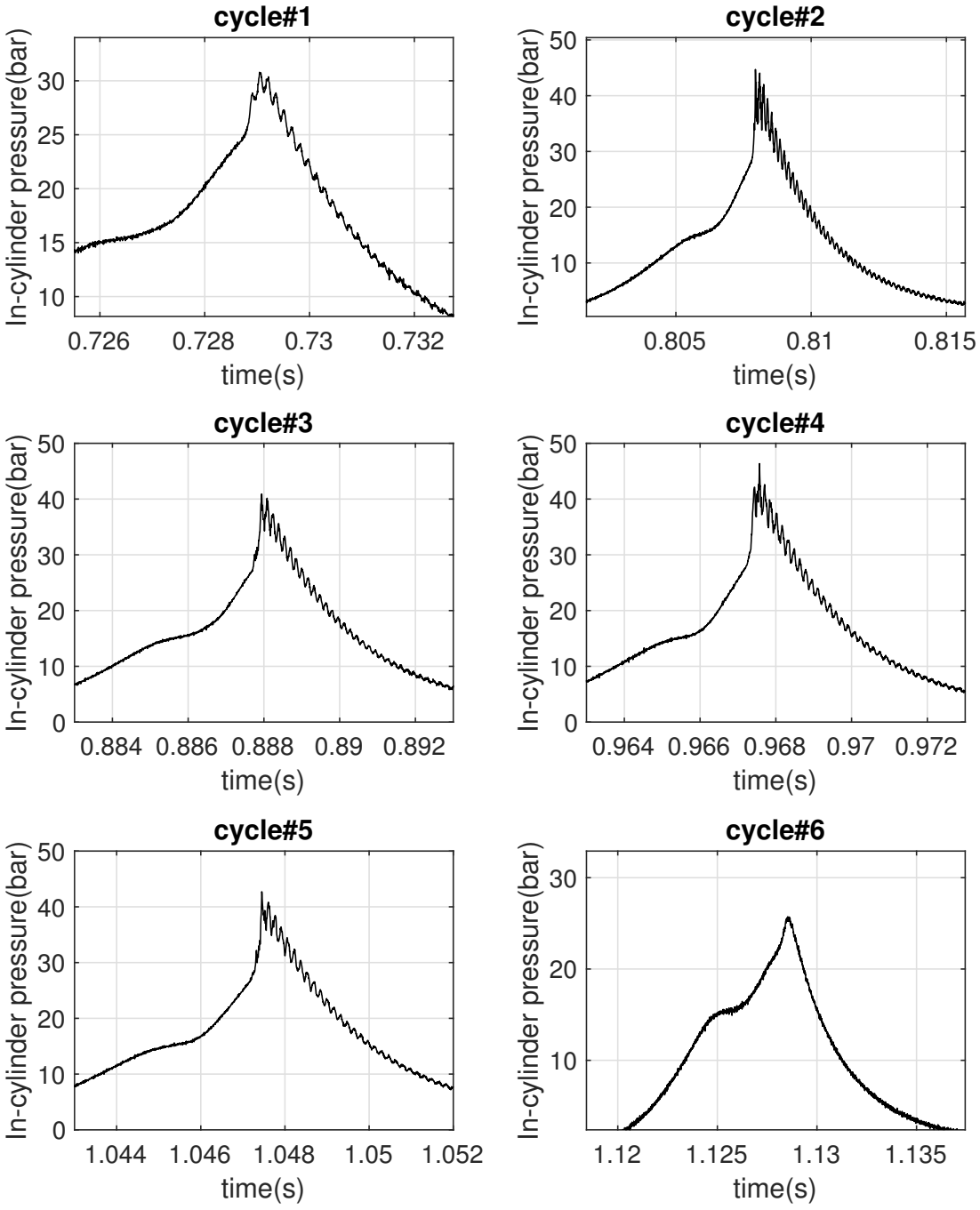

Figure 3.11: Experimental in-cylinder pressure of 6 consecutive cycles under knocking combustion, engine operated at 1500rpm, IMEP=7.5bar (case 1)

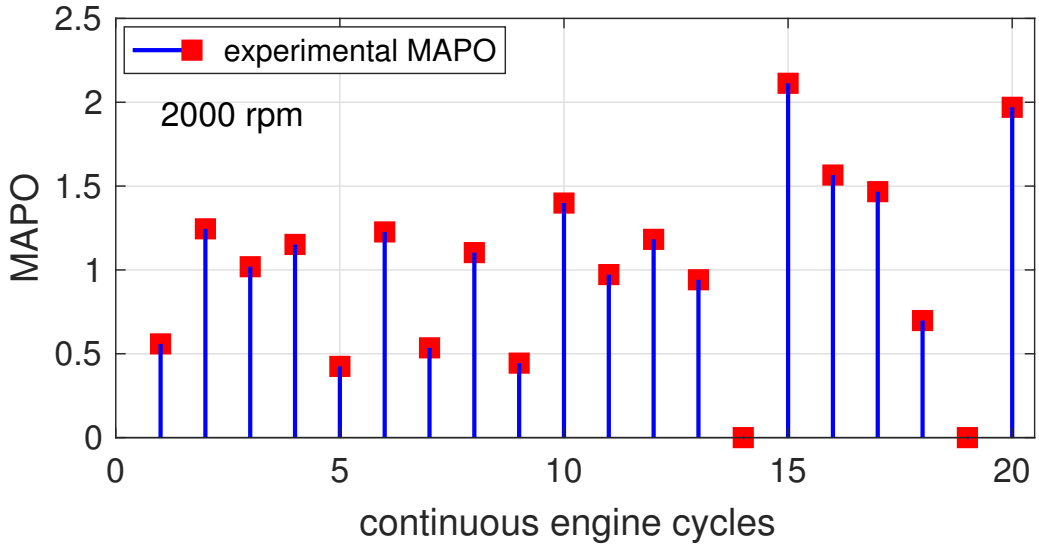

Figure 3.12: MAPO of 20 consecutive engine cycles calculated based on the experimental in-cylinder pressure at 2000rpm, IMEP=8.23bar (case 2). SD: Standard deviation

To verify this assumption and study the influence of T_{IVC} to the knock intensity and T_{EVO}, 6 combustion cycles are simulated at 2000 rpm with 8.23 bar IMEP for a given set of monotonically decreasing T_{IVC}, along with the proposed pressure wave model, to generate pressure and its wave signals. The associated results are shown in Table 3.5 with the highest T_{IVC} of 389K and lowest 349K. The exhaust temperate at EVO (T_{EVO}) is predicted by the two-zone reaction-based combustion model (see Equation (2.33)) developed earlier. The predicted unburned zone temperature are shown in Figure 3.13.

Table 3.5: Simulation results for 6 engine cycles with monotonically decreasing T_{IVC}.

Cycles	T_{IVC} [K]	T_{EVO} [K]	MAPO [bar]
#1	389	1537	2.3759
#2	376	1549	1.7679
#3	370	1558	1.5773
#4	366	1565	0.9912
#5	358	1586	0.8211
#6	349	1634	0

As shown in Table 3.5 and Figure 3.13, the first cycle starts with the highest T_{IVC} of 389K, the

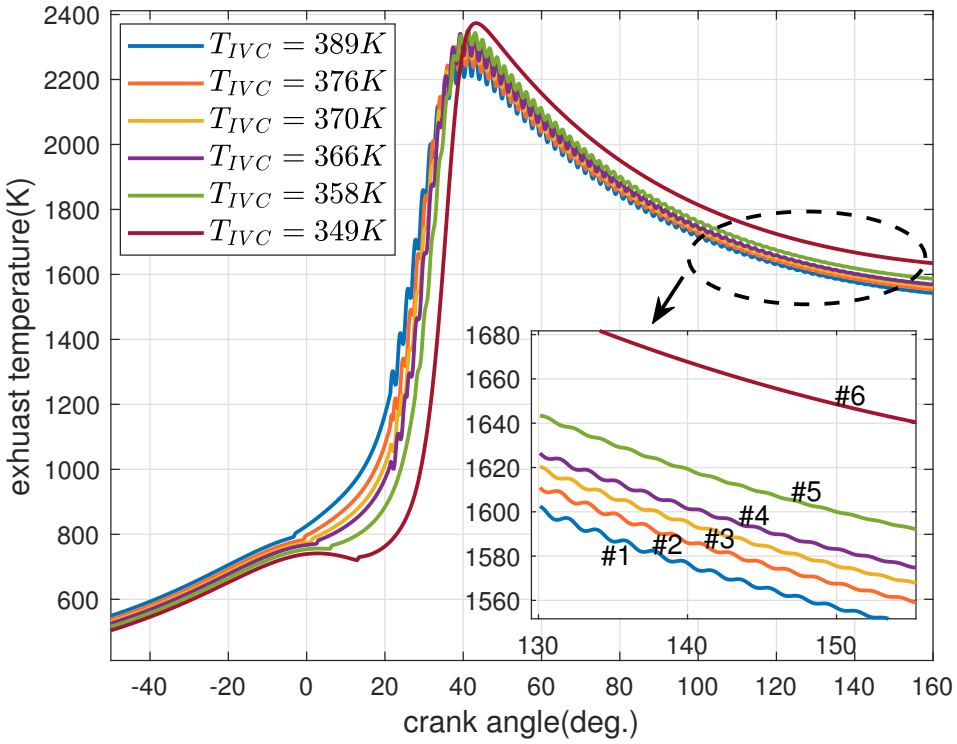

Figure 3.13: Reaction zone temperature (6 cycles) with monotonically decreasing T_{IVC} at 2000 rpm, IMEP = 8.23 bar (case 2)

combustion is very fast, leading to high reaction rate and unburned zone temperature, resulting in fast heat loss to the cylinder wall and low rest net heat transfer in the unburned zone (small $\dot{Q}_u$). Based on equation (2.33), the exhaust temperature will decrease. In addition, knocking combustion could also destroy the cylinder-wall oil film and lead larger heat transfer (loss), comparing to the normal combustion cycle. Based on the energy balance, increased energy (heat) lost during knock combustion results in reduced exhaust temperature. Therefore, the first cycle has the lowest exhaust temperature (T_{EVO}), comparing with 5 other cycles.

A little bit lower T_{IVC} is given to the next (second) cycle, and the simulation results indicate that T_{EVO} increases by 12K and the corresponding knock intensity (MAPO) decreases by 25.5%. This trend continues as the temperature at IVC reduces. Therefore, the simulation results confirm the hypothesis that T_{IVC} is highly correlated to knock intensity. That is, the high the T_{IVC} is, the

high the knock intensity.

In addition, for the engine cycles under knock combustion at a fixed operating condition, the mixture temperature at IVC of cycle $k+1$ ($T_{IVC}(k+1)$) could be influenced by the residual gas (exhaust) temperature of cycle k ($T_{EVO}(k)$).Generally, the knock variability could be caused by many factors, such as the mixture properties at IVC, hot spots, the concentration of fuel, air and residual gas throughout the chamber, locations of auto-ignition. Among them, T_{IVC} is one of the main factors. In order to study the cycle-to-cycle knock variability due to T_{IVC} variation, the experimental in-cylinder pressures of 50 consecutive engine cycles and the proposed pressure wave model are used to predict the next cycle $T_{IVC}(k+1)$ based on the exhaust temperature $T_{EVO}(k)$ of current cycle. Assuming that T_{IVC} is only affected by the exhaust temperature of the previous cycle, 50 engine cycles are simulated to generate in-cylinder pressure and its knock wave. For each cycle, T_{IVC} is optimized by minimizing the prediction error of in-cylinder pressure. The results are shown in Figure 3.14, where each blue-square marker represents one cycle experimental data point. the error bar presents the influence of other factors. Note that there are many repeated temperate points $T_{IVC}(k+1)$ and the number of markers in Figure 3.14 is less than 50.

As shown in Figure 3.14, the experimental $T_{IVC}(k+1)$ and $T_{EVO}(k)$ show an obvious correlation, and the fitted curve (red solid-line) can be used to predict the T_{IVC} of next cycle based on the exhaust temperature of current cycle. However, the fitted curve only reflects the influence of T_{IVC} due to the last cycle exhaust temperature. In order to have an accurate prediction of T_{IVC}, the influence of other factors are included by adding a random variable to this fitted curve; see below.

$$T_{IVC(k+1)} = f_{cf}(T_{EVO}(k)) + \psi \tag{3.46}$$

where f_{cf} is the fitted curve (red solid-line) in Figure 3.14, and ψ is a zero-mean random variable with normal distribution, that is, $\psi \sim \mathcal{N}(0, 30)$.

Therefore, the correlation between knock intensity and mixture temperature at IVC is further studied based on (3.46), where the simulated current cycle exhaust temperature is used to find the mixture temperature at IVC for the next cycle. For the simulation study, the mixture temperature at IVC for the first cycle is assigned to 348K (relative low) and the predicted exhaust temperature

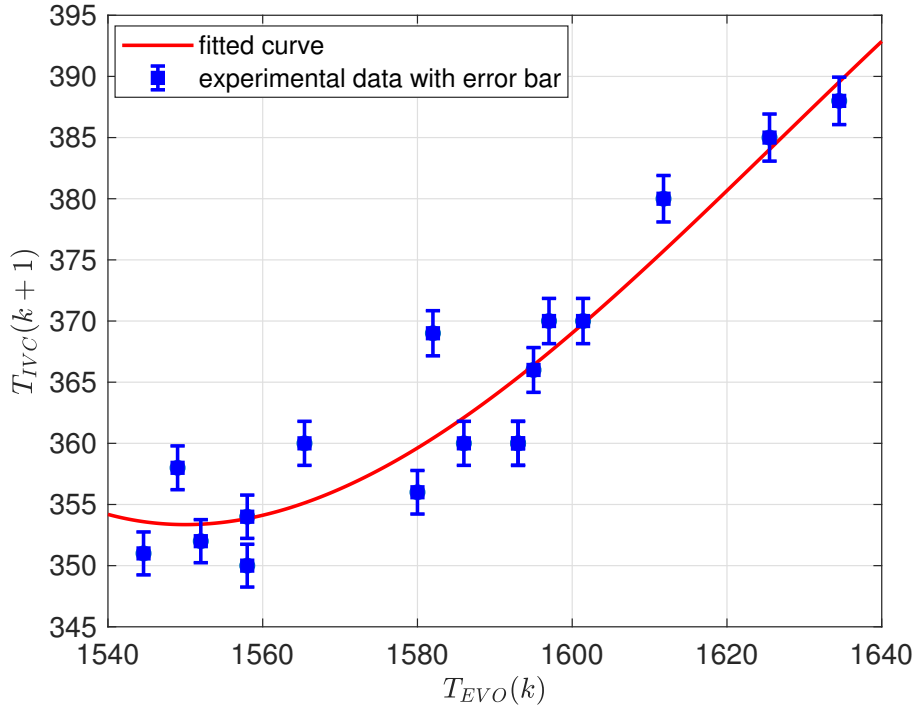

Figure 3.14: Curve fitting for predicting the mixture temperature at IVC of next cycle based on the exhaust temperature at current cycle

(using the proposed pressure wave model) is 1634K and note that this cycle is not knocking with MAPO of 0. Based on (3.46), the predicted T_{IVC} of the second cycle is 390.25K. Therefore, the second cycle simulation is based on $T_{IVC}(k = 2)$ of 390.25K. This process continues for 20 engine cycles; see Table 3.6 for calculated T_{IVC} and simulated MAPO results. As shown in Table 3.6 and Figure 3.15, it is obvious that the heavy knock cycle (high knock intensity) is followed by a light knock cycle (low knock intensity) for most cases. This simulation results match the experimental results (shown in Figure 3.12) in the terms of knock intensity mean and standard deviation (SD), where the mean and SD from simulations are 0.9741 and 0.7605, respectively and these from experiments (shown in Figure 3.12) are 1.0009 and 0.5713, respectively. The capability of the proposed pressure wave model in predicting cycle-to-cycle variability based on in-cylinder mixture temperature at IVC is demonstrated. We believe that the different could be caused by the un-modeled mixture characteristics at IVC.

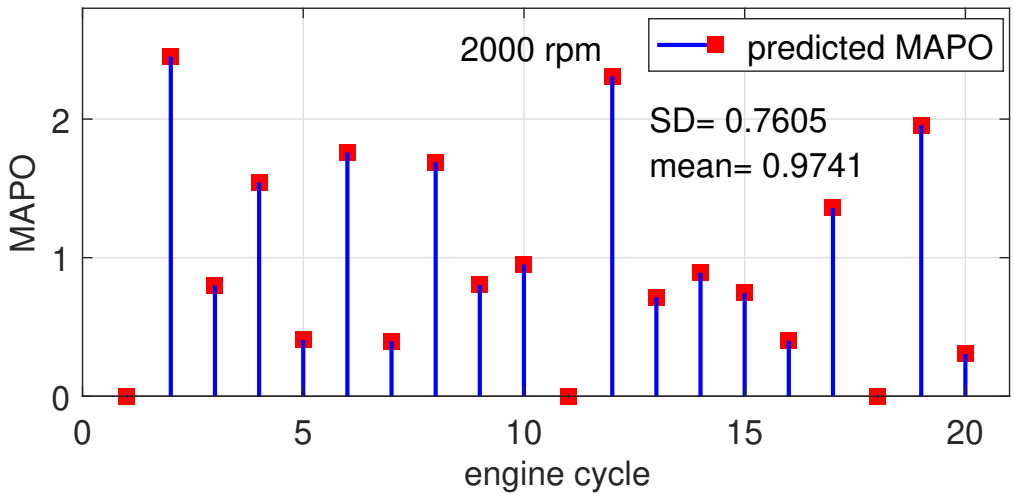

Figure 3.15: Predicted MAPOs of 20 consecutive engine cycles

In summary, the simulation results with the given monotonically decreasing T_{IVC} confirms that the high T_{IVC} is, the high knock intensity is. Also, heavy knocking combustion leads to low exhaust temperature, and hence, low mixture temperature at IVC for the next cycle. The simulation results of 20 consecutive engine cycles show that current cycle T_{IVC} is affected by the last cycle knock intensity and variation of T_{IVC} is one of the main cause for cycle-to-cycle knock variability at a fixed engine operating condition.

3.6 Summary

A control-oriented knock pressure wave model, based on outputs of a two-zone reaction-based combustion model, for spark-ignited (SI) engines is developed to predict knocking combustion in this Chapter. The developed model is calibrated and validated by experimental data. The simulation results confirm model's capable of predicting the key knock characteristics such as knock onset timing, knock frequency and intensity. The maximum prediction error under two engine operating conditions is less than 2.5% and the maximum prediction error for knock intensity (MAPO) is less than 6.38%; the knock frequency prediction is even small (less than 0.2%). In addition, the capability of predicting the cycle-to-cycle knock variability is studied by correlating the knock

Table 3.6: Simulation results (20 consecutive cycles) using predicted T_{IVC}(case 2)

Cycles	T_{IVC} [K]	T_{EVO} [K]	MAPO [bar]
#1	348	1634	0
#2	390.25	1536	2.4512
#3	357.49	1588	0.7986
#4	370.09	1557	1.5429
#5	351.86	1593	0.4073
#6	372.19	1554	1.7591
#7	350.64	1604	0.3985
#8	371.49	1555	1.6881
#9	357.87	1587	0.8043
#10	363.20	1570	0.9509
#11	347.87	1635	0
#12	387.67	1540	2.3088
#13	355.87	1591	0.7139
#14	360.18	1576	0.8915
#15	356.91	1590	0.7453
#16	351.52	1594	0.4014
#17	368.49	1562	1.3589
#18	347.52	1635	0
#19	378.51	1546	1.9567
#20	350.47	1608	0.3052

intensity to the in-cylinder mixture temperature at intake valve closing. Simulation results confirms the hypothesis that the in-cylinder mixtures temperature at IVC is one of the key factor leading to cycle-to-cycle knock variability, and the proposed model is able to replicate this phenomenon, where a high knock-intensity cycle is often followed by a low knock-intensity cycle.

CHAPTER 4

MODEL-BASED STOCHASTIC KNOCK LIMIT CONTROL

4.1 Reaction-Based Knock Predictive Model

The knock predictive model used for the model-based stochastic knock limit control is consisted with two real-time models: the 0-D reaction-based two-zone combustion model and the pressure wave model, that are developed in Chapters 2 and 3, respectively. The correlations of the two models and the model-based knock limit control design are shown in Figure 4.1. As discussed earlier, the reaction-based combustion model is developed to predict the physical combustion process of SI engine in real-time. The inputs are the initial conditions at intake valve close (IVC); see Figure 4.1. Importantly, the combustion model is capable of predicting the properties of species involved in the chemical reactions and the thermodynamic conditions in the combustion chamber, which are the inputs of the pressure wave model. The pressure wave model is developed based on the simplified pressure wave equations, and the corresponding boundary and initial conditions to predict the in-cylinder pressure oscillations due to the shock waves generated in the chamber by the knocking combustion. Based on these two models, the major characteristics of knocking combustion, such as the knock onset timing, knock intensity, and cycle-to-cycle variability, can be predicted and used for the model-based stochastic knock limit control design, which will be discussed in this Chapter.

4.2 Model-Based Prediction of Knock Cyclic Variability

4.2.1 Knock Intensity - KI20 (MAPO)

Knock intensity is the most important criterion to describe the engine knock phenomenon. The experimental in-cylinder pressure of an engine cycle under knocking combustion is shown in Figure 4.2 (the black solid-line). In order to calculate the knock intensity, this in-cylinder pressure is filtered with a 6th order butterworth band-pass filter; see the red solid-line in Figure 4.2. The amplitudes of

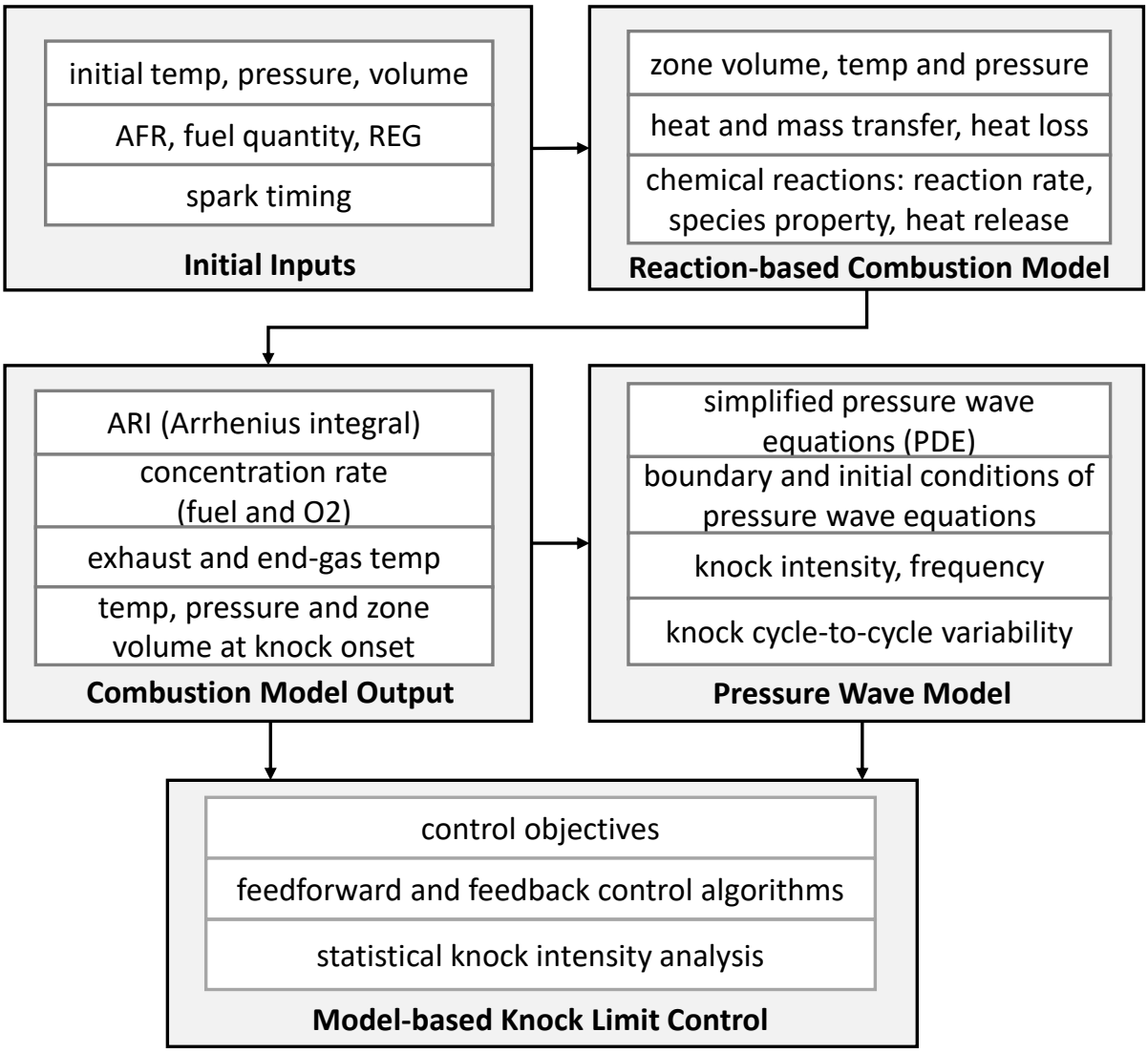

Figure 4.1: Correlation diagram of reaction-based two-zone combustion model, the pressure wave model, and model-based stochastic knock limit control

filtered in-cylinder pressure wave keep decreasing due to the knock intensity decay. To present the knock intensity appropriately, MAPO (KI20) that is to calculate the average amplitude of filtered in-cylinder pressure wave in a pre-defined knock window is used in this dissertation. The calculation formula of MAPO is shown in (3.45). Note that the knock window is defined from knock onset to 20 CAD after it in this dissertation. Therefore, to better indicate the knock intensity with the 20

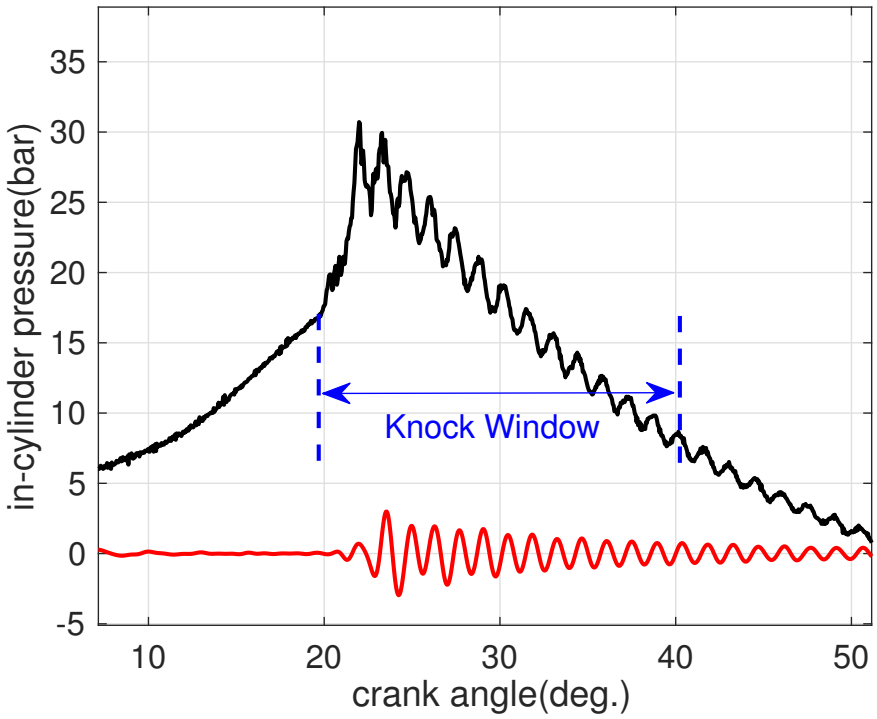

Figure 4.2: Experimental in-cylinder pressure and band-pass filtered pressure wave of one engine cycle

CAD knock window, the knock intensity in this Chapter is presented as KI20 instead of MAPO.

4.2.2 Knock Predictive Model Calibration and Validation

The reaction-based combustion model and pressure wave model discussed in Chapters 2 and 3 were calibrated and validated with the experiment data obtained from the engine bench shown in Table 2.1. The engine was run at 6 different conditions, as shown in Table 4.1. Note that cases 4 and 6 were run at knock limit while the other cases are general conditions. The reaction-based combustion model was calibrated and validated first with the experiment data from cases 1, 2, 3 and 5, and the results demonstrated good model accuracy. Based on the combustion model, the pressure wave model was further calibrated and validated with the experiment data from cases 4 and 6. The model calibration coefficients and validation results can be found in Chapters 2 and 3. The results indicated the capability of the pressure wave model to predict the in-cylinder pressure

Table 4.1: Engine operating conditions.

Case	1	2	3	4 (knock)	5	6 (knock)
IMEP[bar]	4.53	5.01	6.78	7.5	6.83	8.23
Engine Speed[rpm]	1100	1500	1500	1500	2000	2000

under knocking condition with high accuracy of knock onset timing, frequency and intensity, which are three major characteristics of engine knock during one cycle. And this is the foundation for model-based knock control.

4.2.3 Intake Temperature with Knock Cycle-to-Cycle Variability

Engine knock not only has the characteristics presenting with knock onset timing, frequency and intensity but also shows a strong cycle-to-cycle variability that makes the control of knock difficult. By analyzing the experiment data of in-cylinder pressure measured at cases 4 and 6 shown in Table 4.1, it turns out that the knock intensity presented with KI20 has a strong cycle-to-cycle variability even at a steady-state engine operating condition. There are many factors result in the knock cycle-to-cycle variability, but T_{ivc} takes an important role. The high intake manifold temperature will lead to a heavy knocking combustion, with the high temperature in the chamber and heat loss to the wall, and led to the low exhaust temperature. Low exhaust temperature will consequently reduce the intake temperature of next cycle due to the REG trapped in the chamber and then further influence the knock intensity of next cycle. The knock prediction model described in last section was used to study the correlation of T_{ivc} and the exhaust temperature and knock intensity of each cycle. It was verified that the exhaust temperature of each cycle has a strong correlation with the intake manifold temperature T_{ivc} of next cycle. And an experiment data based fitting curve has been found to predict the T_{ivc} of next cycle with the estimated exhaust temperature of current cycle, which can be utilized to study the correlation of knock cycle-to-cycle variability and intake temperature T_{ivc}; see Figure 4.3.

The blue squares represent the experiment data based exhaust temperature (T_{evo}) with the

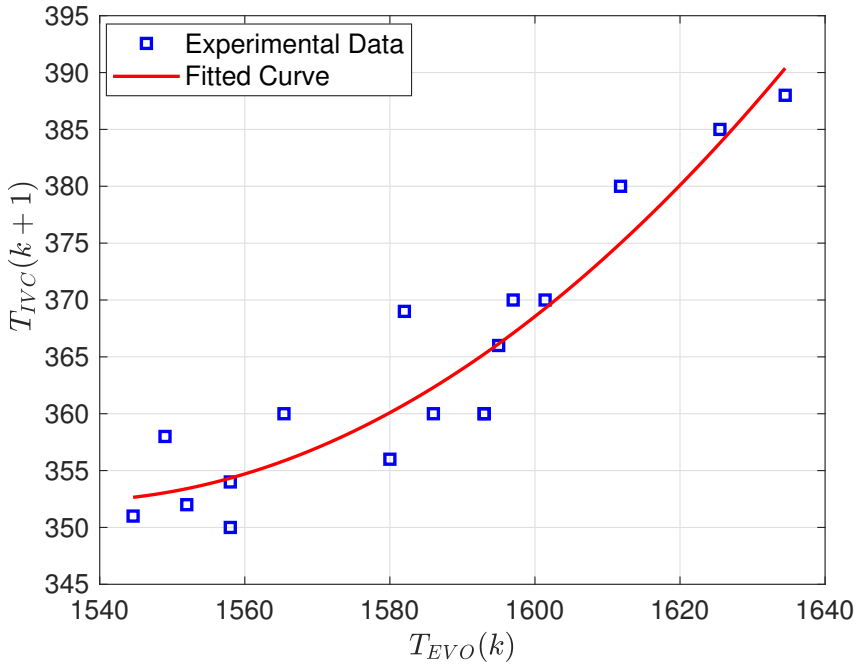

Figure 4.3: Fitted correlation curve between current cycle $T_{evo}(k)$ and next cycle $T_{ivc}(k+1)$

corresponding T_{ivc} of next cycle. The red solid-line is the fitted curve. Based on this fitted curve, the intake manifold temperature of each cycle can be predicted based on the exhaust temperature of the last cycle.

4.2.4 Spark Timing with Knock Cycle-to-Cycle Variability

After the correlation of T_{ivc} and knock intensity KI20 and cycle-to-cycle variability have been obtained, the influence of spark timing and T_{ivc} to the knock cycle-to-cycle variability has been studied as well. Note that the statistic method has been utilized to analyze the knock cycle-to-cycle variability. Especially, the experimental data shows that the knock intensity distribution fits the Gaussian curve, so the mean value and deviation of knock intensity have been used to present the knock cycle-to-cycle variability in this dissertation.

First, the correlation of knock intensity (KI20) and in-cylinder mixture temperature at IVC (Tivc) is studied as well using the knock predictive model. Sixty continuous engine cycles are

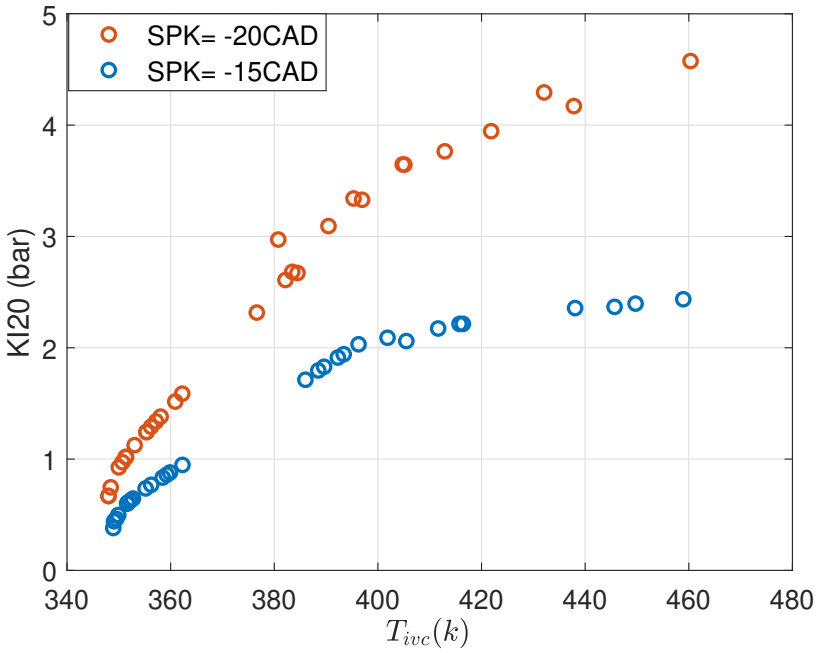

Figure 4.4: Intake temperature T_{ivc} with knock intensity

simulated, and the spark timing of the first 30 cycles is 20 CAD BTDC while the other 30 cycles have a spark timing of 15 CAD BTDC. For each cycle, the in-cylinder mixture temperature at IVC (T_{ivc}) is predicted based on the exhaust temperature from the combustion model and the fitted curve shown in Figure 4.3. The knock intensity (KI20) of each cycle is calculated by processing the in-cylinder pressure signal from the knock predictive model. And the results are shown in Figure 4.4. It indicates that the knock intensity has a strong polynomial correlation with T_{ivc}, and advancing spark timing increases knock intensity.

The extensive simulations are executed over different spark timing (from 10 CAD BTDC to 20 CAD BTDC, with 1 CAD increment). Based on the simulation results, Figure 4.4 has been extended under different spark timing, shown in Figure 4.5. Therefore, T_{ivc} can be used to predict the knock intensity, which is the foundation for the model-based stochastic knock limit control design in next section.

Second, the knock predictive model is used to study the influence of spark timing to the knock

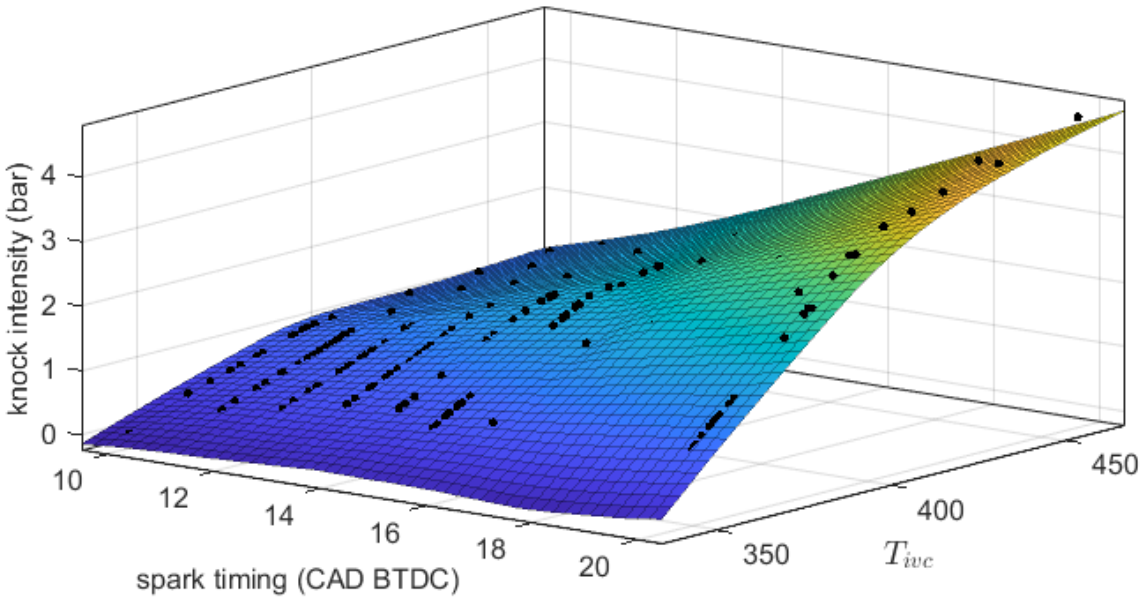

Figure 4.5: Interpreted map for the correlation of intake temperature T_{ivc} and knock intensity as long as the spark timing

cycle-to-cycle variability. The simulation results of the sixty continuous cycles with the spark timing of 20 CAD BTDC and 15 CAD BTDC are analyzed to study this impact and the result is shown in Figure 4.6.

As shown in Figure 4.6, the red bars are the KI20 of 30 continuous engine cycles with spark timing of 20 CAD BTDC while the blue bars are for another 30 continuous cycles with retarded spark timing of 15 CAD BTDC. It is obvious that the knock intensities with retarded spark timing are more gentle than the results with advanced spark timing. Since the experimental data studies show that the knock intensity distribution fits the Gaussian curve, so the mean value, standard deviation and the three standard deviation confidence interval up limit ($\text{CIL}_{3\sigma}$) are used to evaluate the impact of spark timing to the knock cycle-to-cycle variability.

The mean value and standard deviation for the spark timing of 20 CAD BTDC are 2.3169 bar and 1.0291 bar while they are 1.4527 bar and 0.6481bar for 15 CAD BTDC. With 5 degrees retarded

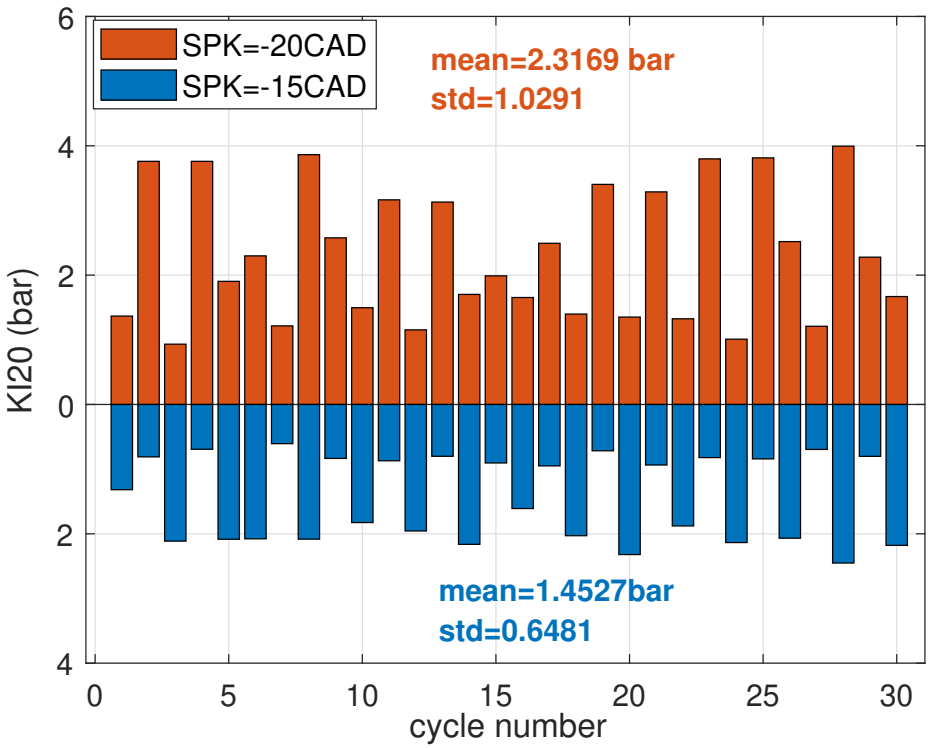

Figure 4.6: The influence of spark timing to knock intensity cycle-to-cycle variability

Table 4.2: Statistic analysis for the impact of spark timing to the knock cycle-to-cycle variability.

case	mean[bar]	std[bar]	$CIL_3\sigma$[bar]
SPK=20[CAD BTDC]	2.3169	1.0291	5.4042
SPK=15[CAD BTDC]	1.4527	0.6481	3.3970

$CIL_3\sigma$: three standard deviation confidence interval up limit

spark timing, the mean value of KI20 reduced by 37.3% and the standard deviation reduced by 37.02%. The three standard deviation confidence interval up limit ($CIL_{3\sigma}$) for spark timing of 20 CAD BTDC is 5.4042 bar while the case with 15 CAD BTDC is 3.3970 bar, moved 2.0072 bar to left; see Table 4.2. In summary, the knock intensity of each cycle can be controlled by tuning the sparking timing of the corresponding cycle, and the knock cycle-to-cycle variability can be further reduced as well.

4.3 Stochastic Knock Limit Control and Results Discussion

4.3.1 Control Objectives

In this dissertation, the stochastic knock limit control strategy is designed based on the knock predictive model, where the control input of the knock predictive model is the spark timing of each cycle and the output is the predicted knock intensity of the associated cycle. It is assumed that the knock intensity fits the Gaussian distribution, and the stochastic knock limit control performance is evaluated by analyzing its mean value, standard deviation and $\text{CIL}_{3\sigma}$ of knock intensity over certain cycles. Moreover, the knock limit and MBT timing constraint of each cycle are considered as well for the best fuel economy.

There are three objectives for the stochastic knock limit control design.

1. The mean value of the knock intensity should be below the desired limit KI20_{desire}, where KI20_{desire} is defined to be 1 (KI20_{desire} = 1bar) in this study.

2. Since analysis indicates that the knock intensity fits the Gaussian distribution, the second control objective is to reduce the cycle-to-cycle knock intensity. In this paper, this interval is defined as the three standard deviation interval with the up-bound presented as $\text{CIL}_{3\sigma}$. Both the knock limit control and MBT timing control are considered at each cycle by compensating spark timing. For the cycle that the knock intensity is within the desired limit, the spark timing should be gradually advanced to the MBT timing.

3. The three standard deviation confidence interval up-bound $\text{CIL}_{3}\sigma$ should be close to 1, which guarantees the knock intensity distribution staying within a desired bound with minimum cycle-to-cycle variability.

Therefore, a feedforward knock limit control algorithm is proposed first to control the knock intensity cycle-by-cycle to reduce the cyclic variation. Based on this feedforward control algorithm, a closed-loop stochastic knock limit control algorithm is further proposed. The two control

algorithms are based on the knock predictive model developed earlier and the two fitted curves shown in Figures. 4.3 and 4.4 are used to compensate the spark timing cycle-by-cycle.

4.3.2 Model-Based Feedforward Knock Limit Control

4.3.2.1 Control Algorithm

Based on the discussion in the last section, the engine knock cycle-to-cycle variability has a strong correlation with intake temperature T_{ivc}. Under knock condition, the T_{ivc} of each cycle is influenced by the knocking combustion and exhaust temperate of the last cycle. The fitted curve shown in Figure 4.3 can be used to predict the T_{ivc} of next cycle. With the predicted T_{ivc} and the fitted curve shown in Figure 4.4, the knock intensity of next cycle can be predicted. Note that the fitted curve shown in Figure 4.4 has been extended under different spark timing by sweeping the spark timing from 10 to 20 CAD BTDC with 1 CAD increment; see Figure 4.5. Therefore, the spark timing can be retarded for knock limit control or advanced for MBT timing control. A feedforward knock limit control algorithm has been proposed in this section to control the knock intensity cycle-by-cycle; see Figure 4.7.

As shown in Figure 4.7, the initial spark timing ($\theta_{spk,T}$) is defined based on a calibrated table as a function of current engine operating condition to achieve MBT timing. With $\theta_{spk,T}$ and other initial inputs, such as $T_{ivc}, p_{ivc}, AFR, m_f$, etc., the exhaust temperature of current cycle $T_{evo}(k)$ can be obtained from the knock predictive model. With the $T_{evo}(k)$, the intake temperature of next cycle $T_{ivc,p}(k+1)$ can be predicted based on the fitted curve shown in Figure 4.3. Note that a zero-mean random variable ϕ with normal distribution disturbance (see equation (4.1)) is added to the predicted $T_{ivc,p}(k+1)$ to represent the influence of other factors to the engine knock.

$$T_{ivc}(k+1) = T_{ivc,p}(k+1) + \phi, \quad \phi \in \mathcal{N}(0, 30) \tag{4.1}$$

As a result, the next cycle knock intensity $\mathrm{KI20}_p(k+1)$ can be predicted based on the fitted curve shown in Figure 4.5 based on $\theta_{spk,T}$ and estimated $T_{ivc}(k+1)$. As a result, there are two cases for

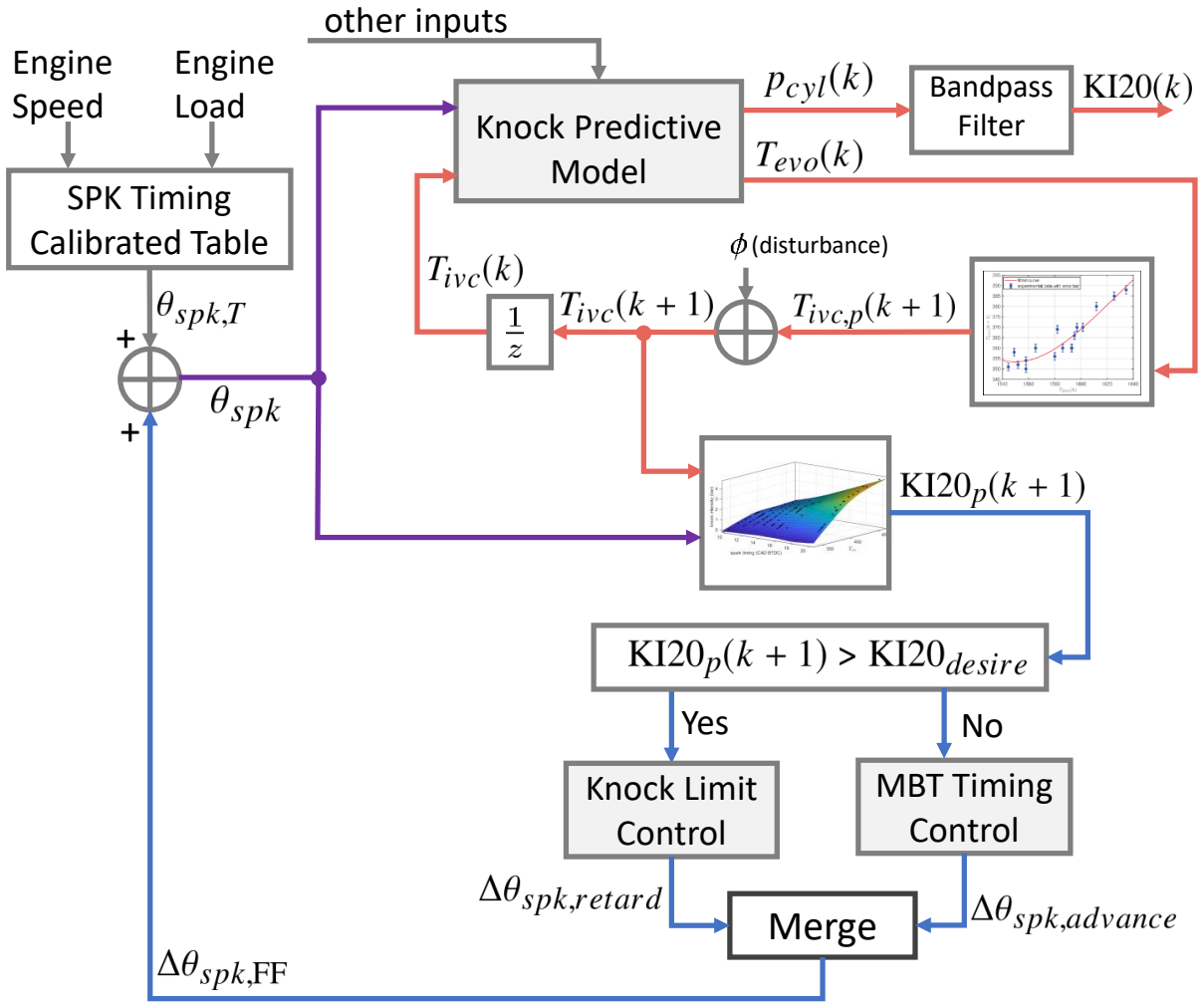

Figure 4.7: Model-based stochastic feedforward knock limit control diagram

spark timing control: knock limit control and MBT timing control.

Knock Limit Control: If the predicted knock intensity is greater than the desired knock intensity limit (KI20$_p(k+1)$ > KI20$_{desire}$), the spark timing of the next cycle will be retarded. The compensation of spark timing, represented by $\Delta\theta_{spk,retard}$, can be obtained based on $T_{ivc}(k+1)$, KI20$_{desire}$ = 1 bar and the map in Figure 4.5.

MBT Timing Control: If the predicted knock intensity is within the desired limit (KI20$_p(k+1)$ < KI20$_{desire}$), there will be no knock spark timing correction and the calibrated engine MBT

timing should be used. The MBT timing is obtained by the peak cylinder pressure location (PPL). In general, the PPL should be maintained at 15 CAD ATDC (desired MBT timing). The compensation of MBT spark timing in this case is represented by $\Delta\theta_{spk,advance}$. Note that the compensated MBT spark timing should not be greater than the knock limited spark timing. $\Delta\theta_{spk,advance}$ can be obtained based on $T_{ivc}(k+1)$, KI20_{desire} = 1 bar and the map in Figure 4.5.

4.3.2.2 Results and Discussion

To validate the control performance of the proposed diagram shown in Figure 4.7, a baseline simulation of 30 continuous engine cycles without control was conducted first, and then the feedforward control was turned on for another 20 continuous cycles. The results are shown in Figure 4.8. Note that the first 30 cycles has a constant spark timing of 20 CAD BTDC, and the spark timing for the cycles from 31 to 50 is controlled cycle-by-cycle based on the control scheme in Figure 4.7.

The spark timing from cycles 31 to 50 (total of 20 cycles) with feedforward control is shown in Figure 4.9, where the red bars present the spark timing of each cycle without the compensation $\Delta\theta_{spk,FF}$, while the blue bars are with the feedforward compensation. The difference between red and blue bars is the advanced or retarded spark timing generated by the feedforward control scheme shown in Figure 4.7. For these cycles that predicted knock intensity are greater than the desired level, the spark timing is retarded with a downward arrow presented in Figure 4.9 (for example, cycles 31, 32, 35, etc.). For these cycles that the predicted knock intensity is below the desired level, the spark timing is advanced but not over the knock limit to be as close to the MBT timing as possible; see upward arrow in Figure 4.9 (for example, cycles 36, 37, 38, etc.). For these cycles, with the predicted knock intensity very close to the desired level but not over it, the spark timing will not be compensated ($\Delta\theta_{spk,FF} = 0$) (for example, cycles 33 and 34).

Th details of knock intensity from cycles 31 to 50 are shown in Figure 4.10. Figures 4.8 and 4.10 demonstrate that the knock cycle-to-cycle variation and mean value have be significantly improved. As shown in Figure 4.8, the mean value and standard deviation of the knock intensity

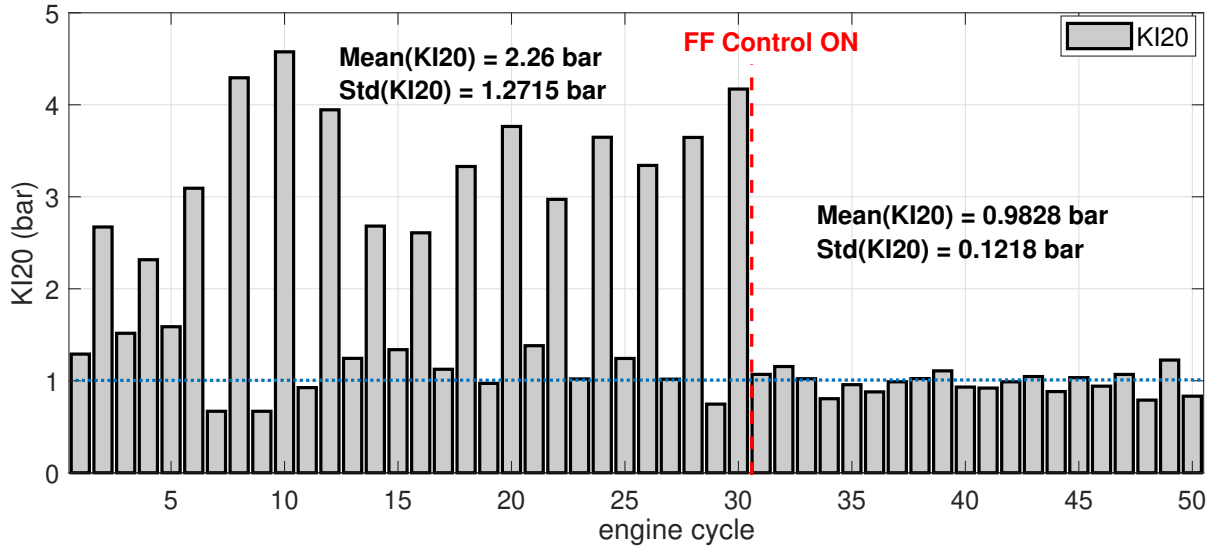

Figure 4.8: Model-based stochastic feedforward knock limit control performance

of the first 30 cycles are 2.26 bar and 1.2715 bar, respectively. Therefore, the corresponding confidence limit $\text{CIL}_{3\sigma}$ is 6.0745 bar. With the stochastic feedforward control, the mean value and standard deviation for cycles 31 to 50 are reduced to 0.9828 bar and 0.1218 bar, respectively. The corresponding $\text{CIL}_{3\sigma}$ is reduced down to 1.3482 bar, with a 77.81% improvement. Figure 4.10 shows that the knock intensity of each cycle is maintained closed to the desired level with the spark timing compensated for each cycle by the proposed feedforward control.

The knock intensity of each cycle before and after the compensation of spark timing ($\Delta\theta_{spk,FF}$) is also compared, and the result is shown in Figure 4.11. The blue solid-line with marker presents the knock intensity of each cycle without the compensation of spark timing while the red solid-line with marker is with compensated spark timing. Based on the discussion of feedforward control scheme shown in Figure 4.7, the knock intensity without spark timing compensation is $\text{KI20}_p(k+1)$ that is predicted based on the $\theta_{spk}(k)$ and $T_{ivc}(k+1)$. If the spark timing is not compensated (without $\Delta\theta_{spk,FF}$), $\theta_{spk}(k+1) = \theta_{spk}(k)$ and the knock intensity of next cycle $\text{KI20}(k+1) = \text{KI20}_p(k+1)$, presented with a blue marker in Figure 4.11. With the feedforward control, the spark timing will be compensated and $\theta_{spk}(k+1) = \theta_{spk}(k) + \Delta\theta_{spk,FF}$, with which the predicted knock intensity

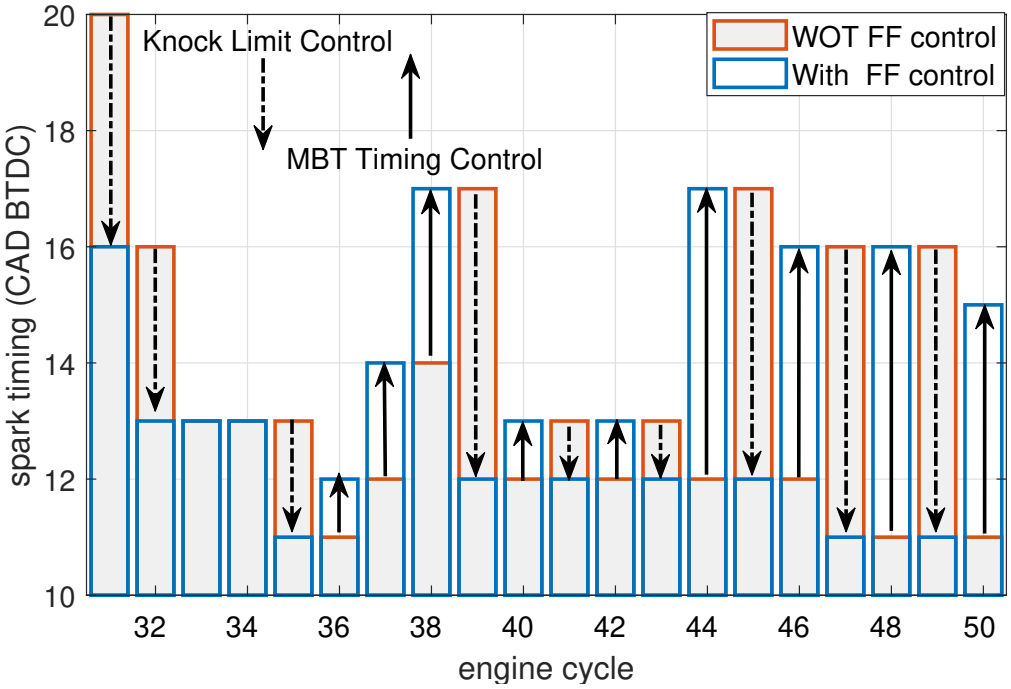

Figure 4.9: Cycle-based spark timing for knock limit and MBT timing control

$KI20_p(k+1)$ will be reduced to $KI20(k+1)$, presented with a red marker in Figure 4.11. Figure 4.11 demonstrates the significant improvement of knock intensity of each cycle with the proposed feedforward control algorithm shown in Figure 4.7.

In addition, with the Gaussian distribution assumption, the comparison of both probability density function (PDF) for the first 30 cycles without control and another 20 cycles with feedforward control is shown in Figure 4.12. It indicates that 99.7% of knock intensity is within the interval of [0.6174, 1.3482] bar after the feedforward control is turn on, that is a significant improvement of knock cycle-to-cycle variability.

4.3.3 Closed-Loop Stochastic Knock Limit Control

4.3.3.1 Control Algorithm

The details of knock intensity of the cycles 31 to 50 in Figure 4.8 with the proposed feedforward control algorithm are shown in Figure 4.10. It indicates the knock intensity variation has been

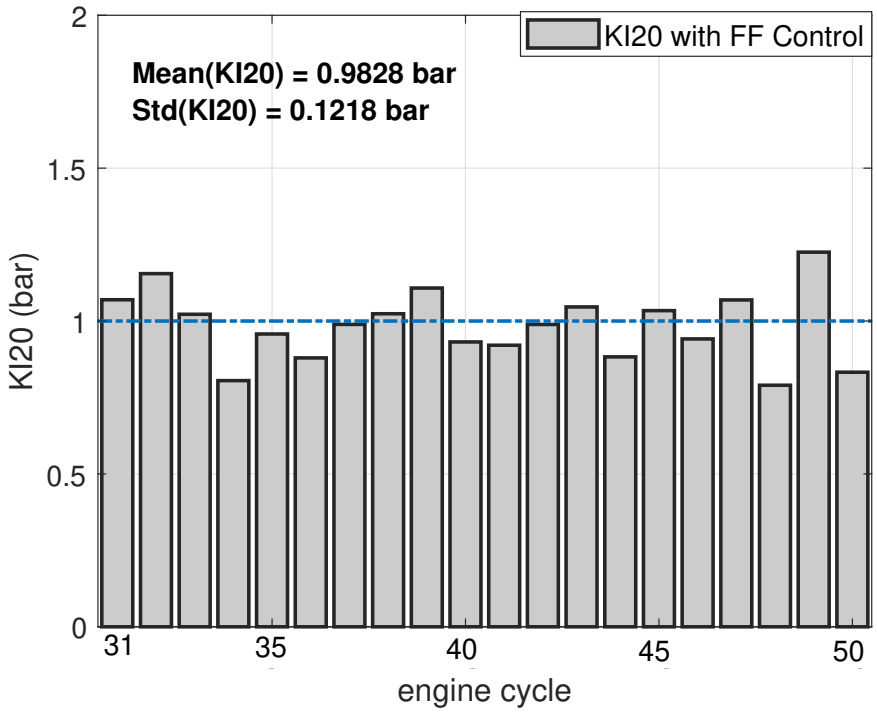

Figure 4.10: Details of knock intensity under model-based stochastic feedforward knock limit control

improved significantly and the mean value has been controlled within the desired bound. However, there are certain cycles that knock intensity is lightly over the desired bound, even with the open-loop spark timing compensation. This is resulted by the factors other than T_{ivc}, that is not included in this knock predictive model; see the error bar shown in Figure 3.14. The influence of these factors are considered using a zero-mean disturbance to be added to predict the intake temperature T_{ivc}. Therefore, a closed-loop stochastic knock limit control algorithm is developed based on Figure 4.7 to improve the control performance of knock intensity of each cycle by further reducing the mean value of knock intensity and also regulating the confidence limit $\text{CIL}_{3\sigma}$ to be close to KI20_{desire}. The proposed closed-loop stochastic knock limit control algorithm is shown in Figure 4.13.

For the proposed closed-loop stochastic knock limit control algorithm, the spark timing of each cycle is compensated not only by the feedforward control developed in the last section but also by

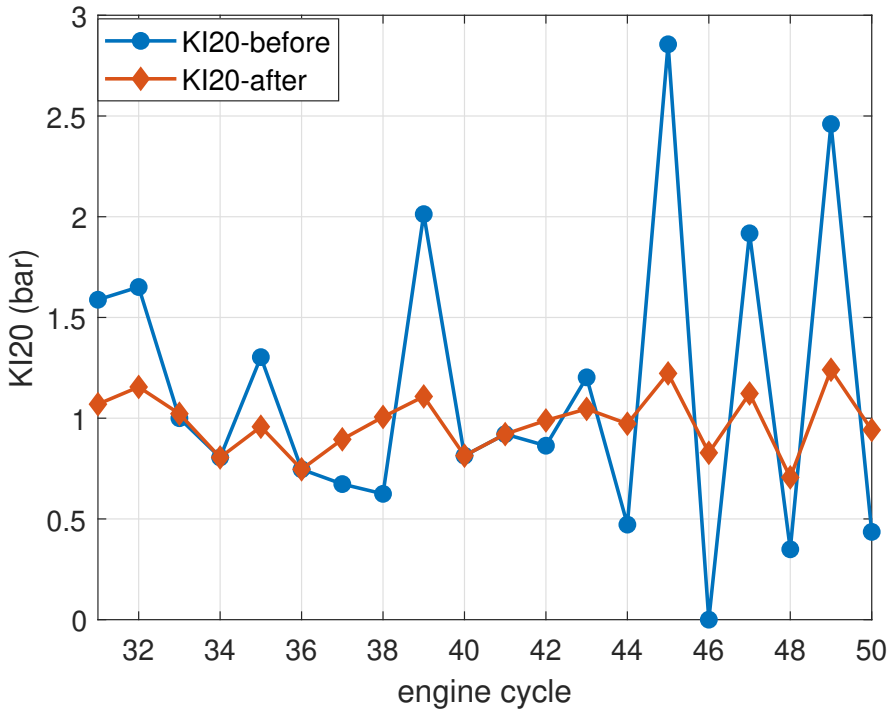

Figure 4.11: Comparison of knock intensity before and after the compensation of spark timing for each cycle

a PI controller in the feedback loop; see (4.2) and Figure 4.13.

$$\theta_{spk} = \theta_{spk,T} + \Delta\theta_{spk,FF} + \Delta\theta_{spk,FB} \tag{4.2}$$

where $\theta_{spk,T}$ is the spark timing based on a calibrated table as a function of current engine operating condition to achieve MBT timing. It remains constant over engine cycles under a steady-state engine condition; $\Delta\theta_{spk,FF}$ is the spark timing compensation by the feedforward control algorithm developed earlier shown in Figure 4.7; $\Delta\theta_{spk,FB}$ is the spark timing compensation from the PI controller in the feedback control loop and will be discussed in this section; and θ_{spk} is the actual spark timing used as an control input to the developed knock predictive model to predict the in-cylinder pressure and exhaust temperature of individual cycle.

As shown in Figure 4.13, the compensated spark timing θ_{spk} and intake temperature T_{ivc} will be the two important inputs to the knock predictive model, a combination of the reaction-based combustion model and pressure wave model. The model has two outputs: exhaust temperature

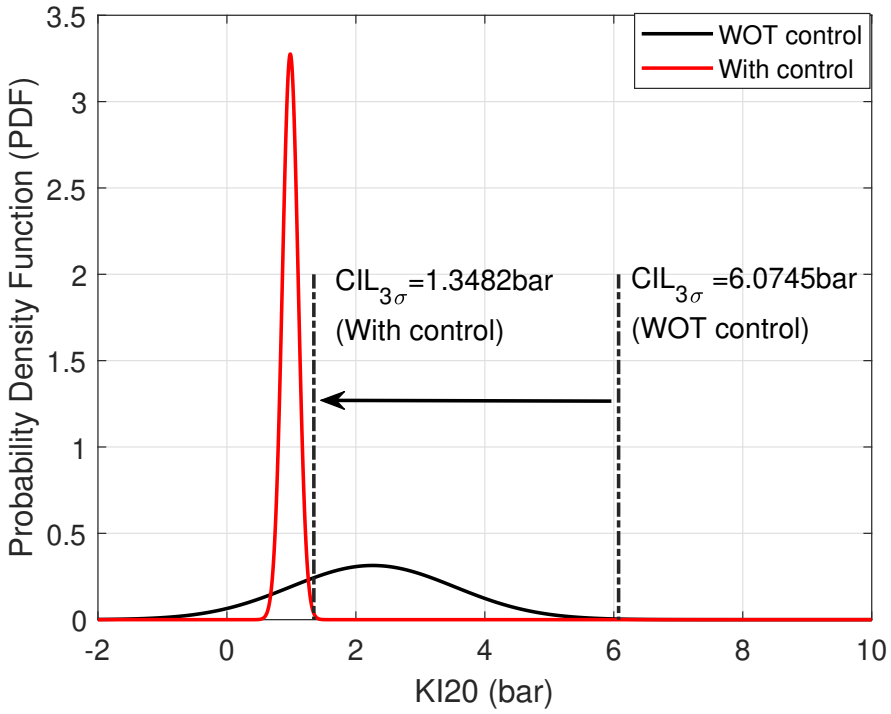

Figure 4.12: Gaussian distribution comparison for knock intensity with and without the proposed feedforward knock limit control algorithm

(T_{evo}) and in-cylinder pressure (p_{cyl}), where T_{evo} is used for the feedforward control discussed in the previous section and in-cylinder pressure p_{cyl} will be processed by a butterworth band-pass filter to generate the knock intensity KI20 of the current cycle. Then KI20 of each cycle will be stored in a buffer for the statistical analysis. Note that the buffer stored the knock intensity of total N continuous cycles as a first in, first out (FIFO) queue: the new predicted knock intensity will be stored as the latest value in the FIFO queue and the previous value stored as KI20(0) will be pop out so that the total length in the buffer is maintained as N cycles; see Figure 4.14.

Based on the stored last N cycles knock intensities, the knock intensity distribution can be analyzed to achieve the mean value, standard deviation and $\text{CIL}_{3\sigma}$. Therefore, the error between the desired knock intensity (KI20_{desire}) and the confidence limit ($\text{CIL}_{3\sigma}$) will be regulated with a PI controller in the feedback loop; see the yellow solid line in Figure 4.13. The spark timing

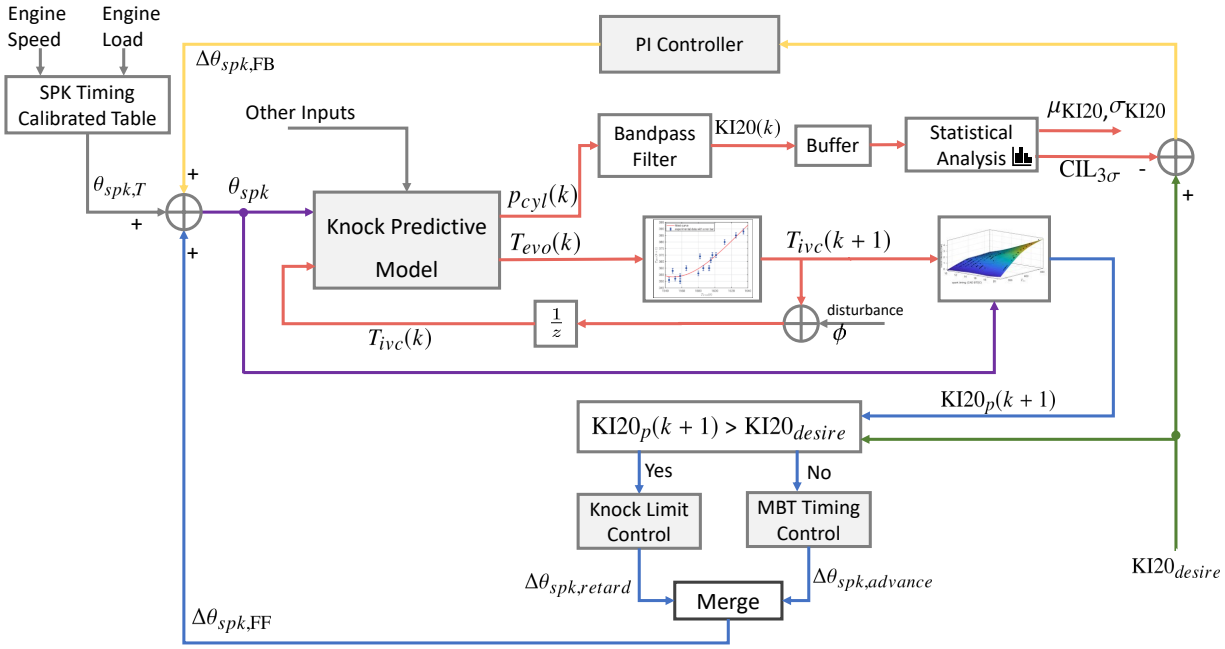

Figure 4.13: Model-based closed-loop stochastic knock limit control diagram

compensation by this loop is calculated by

$$\Delta\theta_{spk,FB} = K_p e(\tau) + K_i T_s \sum_{j=1}^{\tau} e(j) \tag{4.3}$$

where K_p and K_i are two control coefficients for the PI controller; T_s is the time step. Similar with the feedforward control loop which compensates the spark timing for every engine cycle, the feedback control loop also executes at every cycle. And the length of cycles N in the buffer is defined as 20 cycles in the paper. So $\Delta\theta_{spk,FB}$ compensates the spark timing with time step of T_s.

$$T_s = \frac{720}{6N_e} \tag{4.4}$$

where N_e is the engine speed.

4.3.3.2 Results and Discussion

The closed-loop stochastic knock limit control performance is validated by conducting 130 continuous engine cycles. For the 130 cycles, the first 30 cycles are conducted without the two proposed

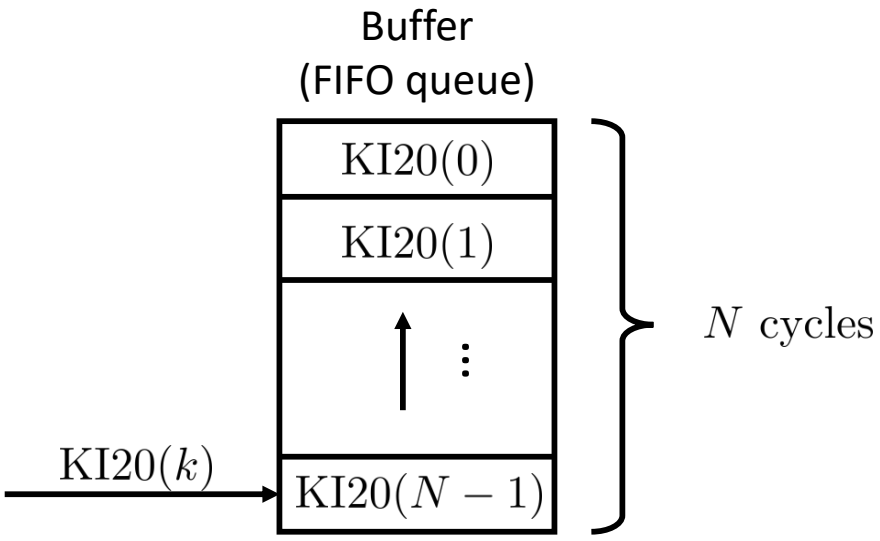

Figure 4.14: Buffer formation for the statistical analysis of knock intensity distribution

control algorithms, and then the feedforward control algorithm shown in Figure 4.7 is turned on from cycles 31 to 50. After that, the closed-loop control algorithm shown in Figure 4.13 is turned on from cycles 51 to 130 to compensate the spark timing at every cycle. Similar to the feedforward control algorithm, the control performance of the closed-loop control algorithm is evaluated based on the statistic analysis of the knock intensity over certain cycles: the mean value, standard deviation and confidence limit.

The time-based spark timing of the 130 continuous engine cycles is shown in Figure 4.15 and the simulation results of knock intensity are shown in Figure 4.16. Since the spark timing is not compensated by $\Delta\theta_{spk,FF}$ and $\Delta\theta_{spk,FB}$ for the first 30 cycles, it remains unchanged (20 CAD BTDC) as shown in Figure 4.15. As discussed in last section, the knock intensity over this duration shows a high deviation and the mean value is over the desired knock intensity limit. With the feedforward control, the knock intensity of each cycle is improved significantly and the mean value is controlled within the bound, and $\mathrm{CIL}_{3\sigma}$ is reduced to be close to the target at 1 bar. However, there are some cycles with knock intensity slightly over the bound. Therefore, both the feedback

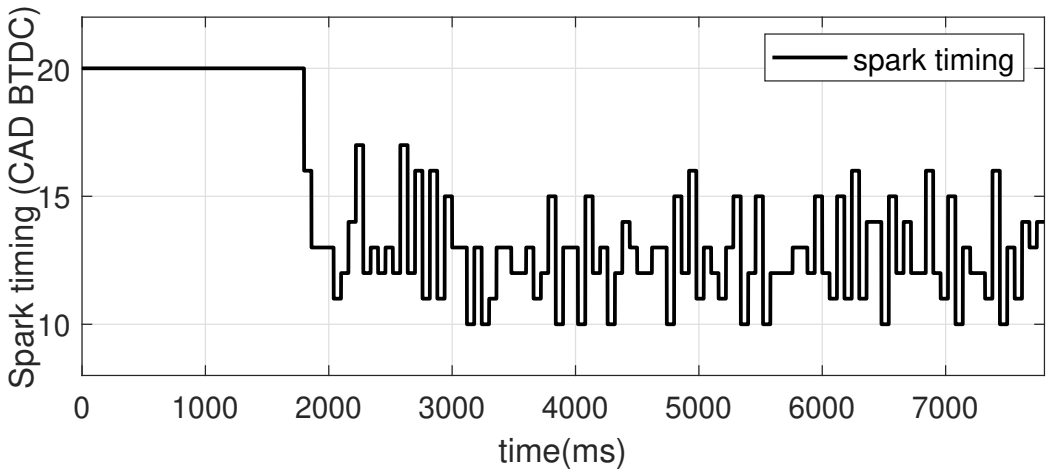

Figure 4.15: Time-based spark timing with the closed-loop stochastic knock limit control algorithm

Table 4.3: Stochastic analysis of cycle-to-cycle knock intensity.

Conditions	Cycles	μ_{KI20}[bar]	σ_{KI20}[bar]	$CIL_{3\sigma}$ [bar]
WOT control	1-30	2.26	1.2715	6.0745
Feedforward control	31-50	0.9828	0.1218	1.3482
Closed-loop control	31-130	0.9432	0.0187	0.9993

and feedforward control loops start to compensate the spark timing from cycle 51. Figure 4.16a shows that the knock cycle-to-cycle variability has been further improved. The performance of two control algorithms is compared in Figure 4.16b. It indicates that the mean value of knock intensity is further reduced with the closed-loop stochastic knock limit control and $CIL_{3\sigma}$ is controlled to be closed to the desired knock intensity bound, which demonstrates the improvement of knock cycle-to-cycle variability.

The statistic analysis results of the 130 cycles are summarized in Table 4.3. It indicates that the mean value of knock intensity has been reduced from 2.26 bar to 0.9828 bar with the feedforward control. Then with the closed-loop control, the mean value has been further reduced down to 0.9432 bar after another 80 continuous cycles. Note that the mean value is slightly reduced with the closed-loop control. The reason is that the MBT timing control regulates the knock intensity

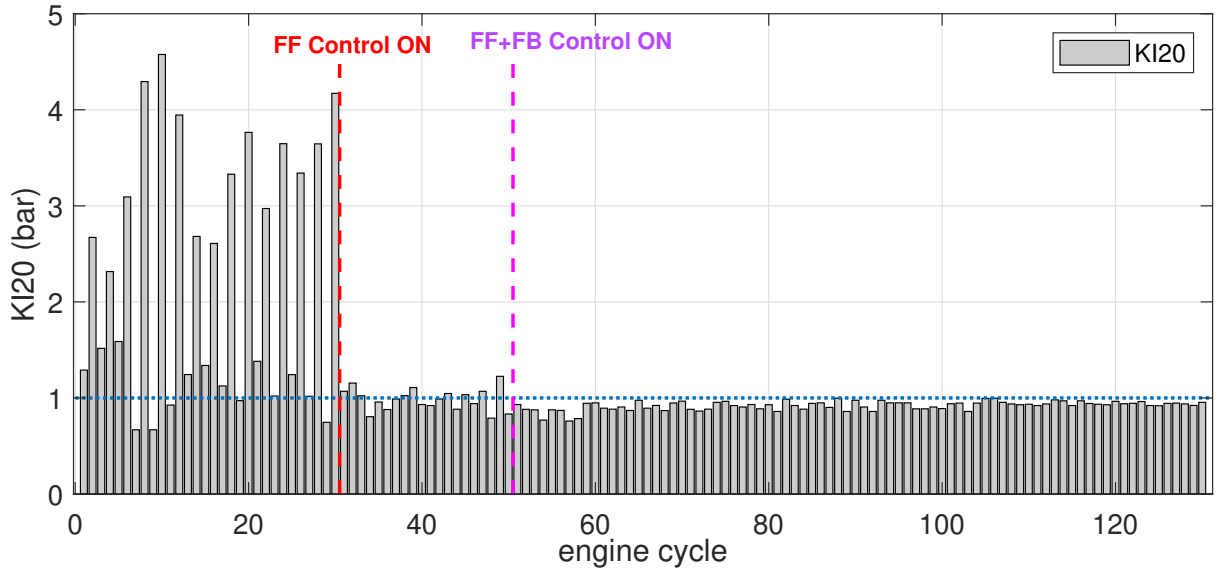

(a)

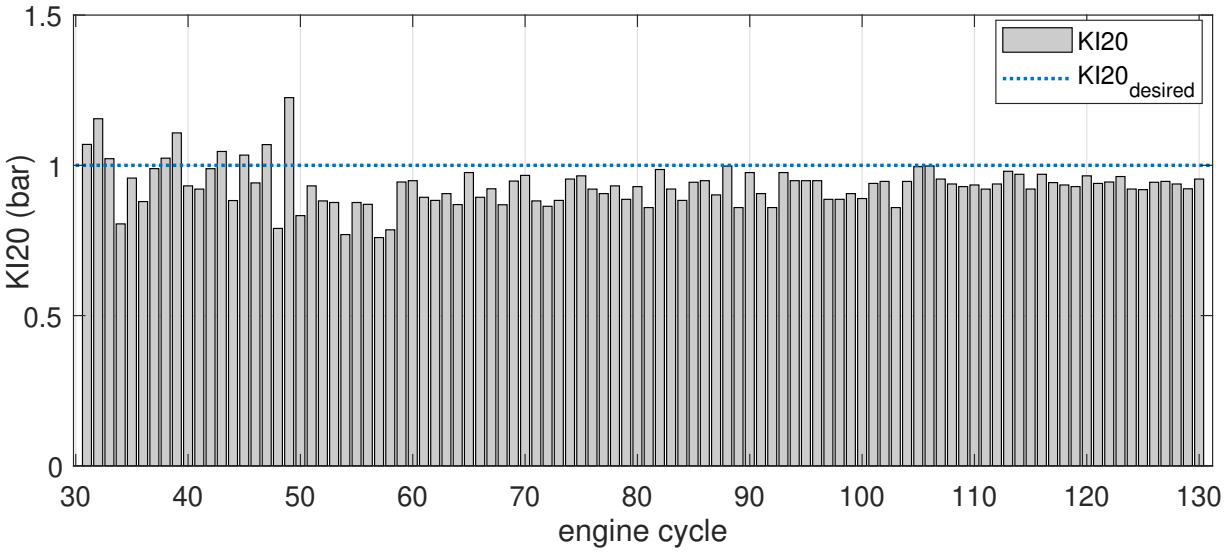

(b)

Figure 4.16: Closed-loop stochastic knock limit control performance

to be close to the bound for the 50 cycles with predicted knock intensity below the desired knock intensity bound. Especially, comparing with the feedforward control, the knock intensity standard deviation with the closed-loop control is significantly reduced from 0.1218 bar to 0.0187 bar, with 86.4% improvement. The confidence limit $\text{CIL}_{3\sigma}$ is driven from 1.3482 bar to 0.9993 bar, very close to $\text{KI20}_{desired}$ and the three standard deviation interval ($[\mu_{\text{KI20}} - 3\sigma_{\text{KI20}}, \mu_{\text{KI20}} + 3\sigma_{\text{KI20}}]$)

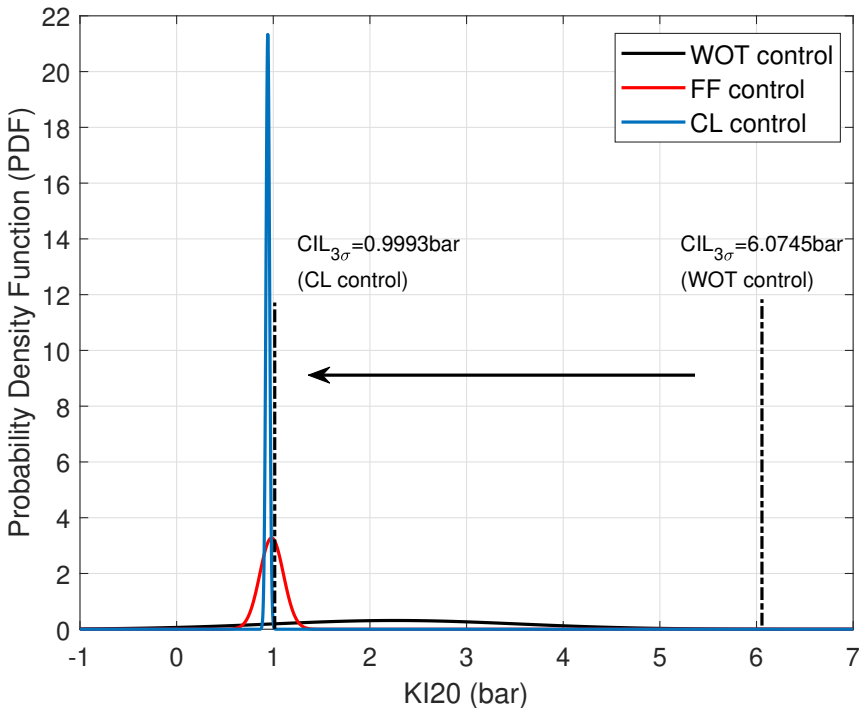

Figure 4.17: Comparison of knock intensity distribution PDF with different control methods

gets narrow. This results indicate that the developed closed-loop control shown in Figure 4.13 is able to control the knock intensity of individual cycle within the bound, and limit the knock intensity distribution in a small interval close to the bound and the knock cycle-to-cycle variability is minimized.

The probability density function (PDF) of the 130 cycles is studied as well to evaluate the closed-loop stochastic knock limit control performance in reducing the knock cycle-to-cycle variability; see Figure 4.17, which shows the knock intensity distribution of 130 cycles without and with different control method. Figure 4.18 shows the details for the cycles that the spark timing is compensated by the proposed two control algorithms. The black solid-line in Figure 4.17 is the PDF curve for the first 30 cycles without control, and the red solid line is for the feedforward control, the blue solid line is for the closed-loop control. The two black dash-dot lines present the confidence limit of cycles 1 to 30 and 31 to 130, respectively. It is obvious that $\text{CIL}_{3\sigma}$ has been reduced from 6.0745 bar to 0.9993 bar after 130 cycles, and is very close to the desired knock intensity

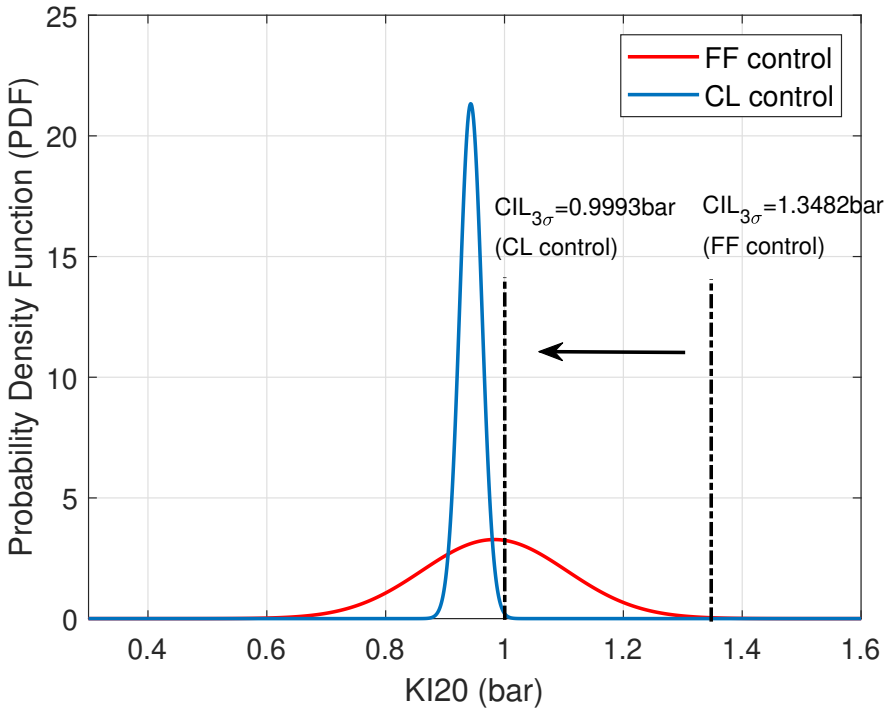

Figure 4.18: Knock intensity distribution PDF with closed-loop stochastic knock limit control

bound. The overall improvement is 83.5% and only 0.15% of cycles have the knock intensity greater than 0.9993 bar. Figure 4.18 shows the knock intensity distribution comparison with two control methods. It indicates that the mean value is gently moved to left and the confidence interval gets narrow significantly. The confidence limit $\text{CIL}_{3\sigma}$ is reduced from 1.3482 bar to 0.9993 bar with 25.87% improvement. This result shows that the capability of closed-loop control has a better performance than the feedforward control for reducing the knock cycle-to-cycle variability.

4.4 Summary

A model-based stochastic feedforward and closed-loop knock limit control strategy is demonstrated in this chapter to regulate the cycle-by-cycle knock intensity within the desired limit and also maintain the knock intensity distribution within the three times of standard deviation confidence interval. The knock predictive model is based on a 0-D two-zone reaction-based combustion model and the pressure wave model developed and validated earlier. The individual cycle spark timing is

retarded or advanced based on the knock limit control or MBT timing control in the feedforward control strategy, respectively. And a PI controller is designed for the closed-loop knock limit control to further improve the control performance. The control performance is demonstrated through simulation studies over 130 continuous engine cycles. With the proposed stochastic feedforward knock limit control strategy, the mean value of knock intensity is reduced from 2.26 bar to 0.9828 bar. The three times of standard deviation confidence limit $\mathrm{CIL}_{3\sigma}$ is reduced from 6.0745 bar to 1.3482 bar, with a 77.81% improvement. With the proposed closed-loop stochastic knock limit control, the mean value has been lightly reduced from 0.9828 bar to 0.9432 bar, and $\mathrm{CIL}_{3\sigma}$ is significantly reduced from 1.3482 bar to 0.9993 bar, with a 25.87% improvement, comparing with the feedforward control. These results indicate the capability of the proposed two control algorithms for improving the knock cycle-to-cycle variability and fuel efficiency due to controlling the spark timing close to MBT. Especially, the closed-loop stochastic knock limit control has a better performance comparing with the feedforward one.

CHAPTER 5

CONCLUSIONS AND FUTURE WORK

5.1 Conclusions

The conclusions of this dissertation can be summarized as follows:

1. A control-oriented, zero-dimensional, two-zone, reaction-based combustion model for compression, combustion and expansion phases of spark ignition engines is developed, calibrated, and validated against experimental data in this dissertation. The developed model is capable of predicting thermodynamic characteristics of in-cylinder chemical mixtures, combustion process, properties of individual chemical species in both unburned and reaction zones. Furthermore, it is also able to predict the auto-ignition in the unburned zone (engine knock). Simulation results show that the developed two-zone combustion model is able to predict the in-cylinder thermal states and combustion process of spark ignition engines, such as the start of combustion, flame propagation process, and in-cylinder heat and mass transfer. The proposed combustion model is capable of accurately predicting combustion process, including the mass variation and thermal properties of each chemical species. Note that the ability to simulate the zone stratification and species molar concentrations allows predicting engine knock. A sensitivity based calibration process divides calibration parameters into two groups with low and high sensitivity, where the default values are used for low sensitivity ones and seven high sensitivity ones are carefully calibrated using experimental data. Especially, the presented simulation results uses only one set of calibration parameters, which means that the model does not need to be re-calibrated under different operational conditions.

2. A real-time pressure wave model is developed utilizing the results from the two-zone reaction-based combustion model to predict the knock characteristics of SI engines. Using the chemical kinetic characteristics of the unburned mixtures, the knock onset timing can be

predicted using the chemical-based Arrhenius integral (ARI). A pressure wave equation, including the pressure oscillation magnitude decay behavior, is obtained by simplifying the 3-D wave equation for real-time simulations, where the initial and boundary conditions for the knock combustion are obtained from the reaction-based combustion model. The proposed in-cylinder pressure perturbation signal is combined with the pressure from the reaction-based combustion model for the composite pressure signal under knock combustion. The capability of this proposed model is validated using the experimental data for knock onset timing, knock intensity and frequency. First, the ARI is calculated and indicates that the knock onset timing is at 21.04 CAD after TDC from experimental data and 21.06 CAD after TDC from simulated data with a prediction error of less than 1.00%. Second, the experimental and simulated in-cylinder pressure signals are used to calculate the knock intensity, where the knock intensity is 1.0088 and 1.0143 bar from experimental and simulated data, respectively. The prediction error is less than 7.0%. Last, the model's ability of predicting the knock frequency is validated by FFT analysis and it shows that the knock frequencies are 6.303 kHz and 6.330 kHz for experimental and simulated data, respectively, where the prediction error is less than 0.5%. s a summary, the proposed in-cylinder pressure wave model is able to accurately predict the key knock characteristics such as the knock onset timing, knock intensity and frequency.

3. A model-based feedforward and closed-loop stochastic knock limit control algorithm is proposed to control the engine knock intensity cycle-by-cycle and reduce the knock cyclic variability. The feedforward control algorithm includes the knock limit control and MBT timing control to compensate the spark timing of individual cycle. The closed-loop control algorithm is developed based on the feedforward and feedback controllers. With the feedforward control, the mean value of knock intensity distribution is reduced from 2.26 to 0.9828 bar and the three standard deviation up-bound limit $\mathrm{CIL}_{3\sigma}$ is reduced from 6.0745 to 1.3482 bar, with a 77.81 % improvement, indicating the significant improvement in reducing the knock cycle-to-cycle variability with MBT timing constraint. With the closed-loop control,

the mean value of knock intensity has been further reduced and $CIL_{3\sigma}$ has been further reduced by 7.42% as well, indicating the closed-loop stochastic knock limit control algorithm has improved performance for reducing the knock cyclic variability comparing with the feedforward control only case.

5.2 Recommendations for Future Work

The following future work is recommended for the knock predictive model-based stochastic knock limit control:

1. For the two-zone reaction-based combustion model, it can be extended in the future by modeling the air-path system of SI engines with EGR and turbocharger. This will be a significant improvement for the control-oriented SI engine model and it will have an extensive application for the model-based engine control.

2. For the knock predictive model:

    a) The fitted curve for intake temperature prediction of each cycle based on the exhaust temperature can be further improved and validated based on the experiment data of extensive engine conditions.

    b) The interpreted 3-D map shown in Figure 4.5 can be further calibrated with the on-board machine learning method in the future bench testing to improve the model-based stochastic knock limit control performance.

3. For the feedforward and closed-loop stochastic knock limit control algorithm, the control performance can be validated in the hardware-in-loop testing with dSPACE and the engine bench testing in the future. And the results can be used to calibrate the PI controller gains in the feedback loop.

BIBLIOGRAPHY

BIBLIOGRAPHY

[1] Abramowitz M, Stegun IA and Romer RH. Handbook of mathematical functions with formulas, graphs, and mathematical tables, 1988.

[2] Wang Z, Liu H and Reitz RD. Knocking combustion in spark-ignition engines. *Progress in Energy and Combustion Science* 2017; 61: 78–112.

[3] Rakopoulos C and Michos C. Development and validation of a multi-zone combustion model for performance and nitric oxide formation in syngas fueled spark ignition engine. *Energy Conversion and Management* 2008; 49(10): 2924 – 2938.

[4] Siano D, Panza MA and D'Agostino D. Knock detection based on mapo analysis, ar model and discrete wavelet transform applied to the in-cylinder pressure data: results and comparison. *SAE International Journal of Engines* 2015; 8(1): 1–13.

[5] Li RC and Zhu GG. A real-time pressure wave model for knock prediction and control. *International Journal of Engine Research* 2019; : 1468087419869161.

[6] Li RC and Zhu GG. A real-time pressure wave model for predicting engine knock. In *ASME 2019 Dynamic Systems and Control Conference*. American Society of Mechanical Engineers Digital Collection.

[7] Jones JCP, Shayestehmanesh S and Frey J. A bayesian knock event controller. *IEEE Transactions on Control Systems Technology* 2019; .

[8] Jones JCP, Spelina JM and Frey J. Likelihood-based control of engine knock. *IEEE Transactions on Control Systems Technology* 2013; 21(6): 2169–2180.

[9] Zhu GG, Haskara I and Winkelman J. Stochastic limit control and its application to knock limit control using ionization feedback. *SAE transactions* 2005; : 40–47.

[10] Men Y, Haskara I and Zhu G. Multi-zone reaction-based modeling of combustion for multiple-injection diesel engines. *International Journal of Engine Research* 2018; : 1468087418788488.

[11] Guzzella L and Onder C. *Introduction to Modeling and Control of Internal Combustion Engine Systems*, volume 53. Berlin: Springer, 2010.

[12] Verhelst S and Sheppard C. Multi-zone thermodynamic modelling of spark-ignition engine combustion - An overview. *Energy Conversion and Management* 2009; 50(5): 1326–1335.

[13] Ghojel JI. Review of the development and applications of the Wiebe function: A tribute to the contribution of Ivan Wiebe to engine research. *International Journal of Engine Research* 2010; 11(4): 297–312.

[14] Yasar H, Soyhan HS, Walmsley H et al. Double-wiebe function: An approach for single-zone hcci engine modeling. *Applied Thermal Engineering* 2008; 28(11-12): 1284–1290.

[15] Miyamoto N, Chikahisa T, Murayama T et al. Description and analysis of diesel engine rate of combustion and performance using wiebe's functions. *SAE transactions* 1985; : 622–633.

[16] Fagundez J, Sari R, Martins M et al. Comparative analysis of different heat transfer correlations in a two-zone combustion model applied on a si engine fueled with wet ethanol. *Applied Thermal Engineering* 2017; 115: 22–32.

[17] Tolou S and Schock H. Experiments and modeling of a dual-mode, turbulent jet ignition engine. *International Journal of Engine Research* 2019; : 1468087419875880.

[18] Li R, Huang Y, Li G et al. Calibration and validation of a mean value model for turbocharged diesel engine. *Advances in Mechanical Engineering* 2013; 5.

[19] Shapiro H and Gerpen J. *Two Zone Combustion Models for Second Law Analysis of Internal Combustion Engines*. Warrendale, PA : Society of Automotive Engineers, 1989.

[20] Loganathan S, Manohar R, Thamaraikannan R et al. Direct Injection Diesel Engine Rate of Heat Release Prediction using Universal Load Correction Factor in Double Wiebe Function for Performance Simulation. *SAE Technical Paper 2011-01-2456,* 2012; .

[21] Saad C, Maroteaux F, Millet JB et al. Combustion Modeling of a Direct Injection Diesel Engine Using Double Wiebe Functions: Application to HiL Real-Time Simulations. *SAE Technical Paper 2011-24-0143,* 2011; .

[22] Borg JM and Alkidas AC. Investigation of the Effects of Autoignition on the Heat Release Histories of a Knocking SI Engine Using Wiebe Functions. *SAE Technical Paper 2008-01-1088,* 2008; .

[23] Rakopoulos C and Michos C. Availability analysis of a syngas fueled spark ignition engine using a multi-zone combustion model. *Energy* 2008; 33(9): 1378 – 1398.

[24] Hvězda J. Multi-Zone Models of Combustion and Heat Transfer Processes in SI Engines. *Journal of Middle European Construction and Design of Cars* 2012; 10(2): 14–22.

[25] Sadabadi K, Shahbakhti M, Bharath A et al. Modeling of combustion phasing of a reactivity-controlled compression ignition engine for control applications. *International Journal of Engine Research* 2015; 17(4): 421–435.

[26] Shivapuji A and Dasappa S. Experiments and zero D modeling studies using specific Wiebe coefficients for producer gas as fuel in spark-ignited engines. *Proceedings of the Institution of Mechanical Engineers, Part C: Journal of Mechanical Engineering Science* 2012; 227(3): 504–519.

[27] Song R, Gentz G, Zhu G et al. A two-stage combustion model for turbulence-jet ignition engines with RCM validation. *Proceedings of the Institution of Mechanical Engineers, Part D, Journal of Automobile Engineering* 2017; 231(13): 1315–1325.

[28] Hall C, Shaver G, Chauvin J et al. Combustion Phasing Model for Control of a Gasoline-Ethanol Fueled SI Engine with Variable Valve Timing. *IEEE American Control Conference (ACC)* 2012; : 1271–1277.

[29] Jia N, Wang J, Nuttall K et al. HCCI Engine Modeling for Real-Time Implementation and Control Development. *IEEE/ASME Transactions on Mechatronics* 2007; 12(6): 581–589.

[30] Men Y, Haskara I, Wang YY et al. Model-based calibration of reaction-based diesel combustion dynamics. *Proceedings of the Institution of Mechanical Engineers, Part D: Journal of Automobile Engineering* 2017; Accepted.

[31] Millo F and Ferraro C. Knock in si engines: a comparison between different techniques for detection and control. *SAE transactions* 1998; : 1091–1112.

[32] Schmillen KP and Rechs M. Different methods of knock detection and knock control. *SAE transactions* 1991; : 1404–1415.

[33] Lee JH, Hwang SH, Lim JS et al. A new knock-detection method using cylinder pressure, block vibration and sound pressure signals from a si engine. *SAE transactions* 1998; : 1808–1819.

[34] Ettefagh M, Sadeghi M, Pirouzpanah V et al. Knock detection in spark ignition engines by vibration analysis of cylinder block: A parametric modeling approach. *Mechanical Systems and Signal Processing* 2008; 22(6): 1495–1514.

[35] Zhu GG, Haskara I and Winkelman J. Closed-loop ignition timing control for si engines using ionization current feedback. *IEEE transactions on control systems technology* 2007; 15(3): 416–427.

[36] Livengood J and Wu P. Correlation of autoignition phenomena in internal combustion engines and rapid compression machines 1955; 5(1): 347–356.

[37] Nakano M, Nakahara S, Akihama K et al. Predictions of the knock onset and the effects of heat release pattern and unburned gas temperature on torque at knock limit in si engines. *SAE transactions* 1995; : 2183–2198.

[38] Elmqvist C AH Lindström F. Optimizing engine concepts by using a simple model for knock prediction. *SAE Technical Paper 2003-01-3123* 2003; .

[39] Pipitone E, Beccari S and Genchi G. A Refined Model for Knock Onset Prediction in Spark Ignition Engines Fueled With Mixtures of Gasoline and Propane. *Journal of Engineering for Gas Turbines and Power* 2015; 137(11): 111501–111509.

[40] Douaud EP A. Four-Octane-Number Method for Predicting the Anti-Knock Behavior of Fuels and Engines. *SAE Technical Paper 780080* 1978; .

[41] Hoepke B, Jannsen S, Kasseris E et al. Egr effects on boosted si engine operation and knock integral correlation, 2012.

[42] Shu G, Pan J and Wei H. Analysis of onset and severity of knock in SI engine based on in-cylinder pressure oscillations. *Applied Thermal Engineering* 2013; 51(1-2): 1297–1306.

[43] Zervas E. Correlations between cycle-to-cycle variations and combustion parameters of a spark ignition engine. *Applied Thermal Engineering* 2004; 24(14-15): 2073–2081.

[44] Bozza F, Siano D and Torella E. Cycle-by-cycle analysis, knock modeling and spark-advance setting of a "downsized" spark-ignition turbocharged engine. *SAE International Journal of Engines* 2010; 2(2): 381–389.

[45] Granet V, Vermorel O, Lacour C et al. Large-eddy simulation and experimental study of cycle-to-cycle variations of stable and unstable operating points in a spark ignition engine. *Combustion and Flame* 2012; 159(4): 1562–1575.

[46] Katsumata M, Morikawa K and Tanabe M. Behavior of shock wave and pressure wave of si knocking with super rapid compression machine. In *SAE International Powertrains, Fuels and Lubricants Meeting*. SAE International 2011-01-1875.

[47] Kawahara N and Tomita E. Visualization of auto-ignition and pressure wave during knocking in a hydrogen spark-ignition engine. *International Journal of Hydrogen Energy* 2009; 34(7): 3156 – 3163.

[48] Yao A, Xu H and Yao C. Analysis of pressure waves in the cone-type combustion chamber under SI engine knock. *Energy Conversion and Management* 2015; 96: 146–158.

[49] Terashima H and Koshi M. Mechanisms of strong pressure wave generation in end-gas autoignition during knocking combustion. *Combustion and Flame* 2015; 162(5): 1944 – 1956.

[50] Richard S, Dulbecco A, Angelberger C et al. Invited Review: Development of a one-dimensional computational fluid dynamics modeling approach to predict cycle-to-cycle variability in spark-ignition engines based on physical understanding acquired from large-eddy simulation. *International Journal of Engine Research* 2014; 16(3): 379–402.

[51] Draper CS. The physical effects of detonation in a closed cylindrical chamber 1935; .

[52] Brecq G and Le Corre O. Modeling of in-cylinder pressure oscillations under knocking conditions: introduction to pressure envelope curve. *SAE International Technical Paper* 2005; 2005(724).

[53] Di Gaeta A, Giglio V, Police G et al. Modeling of in-cylinder pressure oscillations under knocking conditions: A general approach based on the damped wave equation. *Fuel* 2013; 104: 230–243.

[54] Shen X and Shen T. Real-time statistical learning-based stochastic knock limit control for spark-ignition engines. *Applied Thermal Engineering* 2017; 127: 1518–1529.

[55] Zhang Y, Shen X, Wu Y et al. On-board knock probability map learning–based spark advance control for combustion engines. *International Journal of Engine Research* 2019; 20(10): 1073–1088.

[56] Stotsky AA. Statistical engine knock modelling and adaptive control. *Proceedings of the Institution of Mechanical Engineers, Part D: Journal of Automobile Engineering* 2008; 222(3): 429–439.

[57] Kassa M, Hall C, Pamminger M et al. Knock intensity distribution and a stochastic control framework for knock control. *Journal of Dynamic Systems, Measurement, and Control* 2019; 141(11).

[58] Cavina N, Po G and Poggio L. Ion current based spark advance management for maximum torque production and knock control. In *ASME 8th Biennial Conference on Engineering Systems Design and Analysis*. American Society of Mechanical Engineers Digital Collection, pp. 537–545.

[59] Jones JCP, Frey J and Muske KR. A statistical likelihood based knock controller. *IFAC Proceedings Volumes* 2010; 43(7): 809–814.

[60] Luo W, Chen B, Naber J et al. Stochastic knock detection, control, software integration, and evaluation on a v6 spark-ignition engine under steady-state operation. Technical report, SAE Technical Paper, 2014.

[61] Zhou L, Shao A, Hua J et al. Effect of retarded injection timing on knock resistance and cycle to cycle variation in gasoline direct injection engine. *Journal of Energy Resources Technology* 2018; 140(7).

[62] Heywood JB. *Internal combustion engine fundamentals*. New York : McGraw-Hill, 1988.

[63] Woschni G. A Universally Applicable Equation for the Instantaneous Heat Transfer Coefficient in the Internal Combustion Engine. *SAE Technical Paper 670931,* 1967; .

[64] Law CK. *Combustion physics*. Cambridge university press, 2010.

[65] Turns SR. *An Introduction to Combustion: Concepts and Applications*. New York: McGraw-Hill, 2012.

[66] Kikusato A, Terahata K, Jin K et al. A numerical simulation study on improving the thermal efficiency of a spark ignited engine — part 2: Predicting instantaneous combustion chamber wall temperatures, heat losses and knock. *SAE International Journal of Engines* 2014; 7(1): 87–95.

[67] Decan G, Broekaert S, Lucchini T et al. Evaluation of Wall Heat Flux Models for Full Cycle CFD Simulation of Internal Combustion Engines under Motoring Operation. *SAE Technical Paper 2017-24-0032,* 2017; .

[68] Olmeda P, Martín J, Novella R et al. An adapted heat transfer model for engines with tumble motion. *Applied Energy* 2015; .

[69] Le Méhauté B. *Linear Small Amplitude Wave Theories BT - An Introduction to Hydrodynamics and Water Waves*. Berlin, Heidelberg: Springer Berlin Heidelberg, 1976.

[70] Kreyszig E. Advanced engineering mathematics. *Integration* 2008; 9: 4.